Microstructural Optimization of Solid-State Sintered Silicon Carbide

A Thesis
Presented to
The Academic Faculty

by

Lionel R. Vargas-Gonzalez

In Partial Fulfillment
of the Requirements for the Degree
Doctor of Philosophy

School of Materials Science and Engineering
Georgia Institute of Technology
August 1, 2009

Microstructural Optimization of Solid-State Sintered Silicon Carbide

Approved by:

Professor Robert F. Speyer, Advisor	Professor Thomas H. Sanders, Jr.
Professor Robert L. Snyder	Professor Sheldon M. Jeter
Professor Joe K. Cochran	

Date Approved: _____

ACKNOWLEDGEMENTS

First and foremost, I would like to express my appreciation and respect to Professor Robert F. Speyer, for his guidance and advisement through my Ph.D. studies here at Georgia Tech. I have grown and gained much knowledge from him during my term here. I would also like to thank my committee members, Professor Robert L. Snyder, Professor Joe K. Cochran, Professor Thomas H. Sanders, Jr., and Professor Sheldon M. Jeter for their expertise and support given to me. I'd like to express sincere thanks to John T. Corcia, and the Goizueta Foundation for their selfless and generous financial support.

Special thanks goes to my wonderful, loving parents, Ruben and Priscilla, through whom I have been truly blessed. Without their love, support, and faith in me, I would have never made it this far. I'd like to thank the Buckhead Church family, my close friends from small group, my friends on the Parking Team, and my colleagues in the MSE department for being there, sharing in my frustrations and my joys, and supporting me fully throughout the last 4 years.

Last, but certainly not least, all the praise of my accomplishments go to God, through only whom all of this could have ever been possible.

TABLE OF CONTENTS

LIST OF TABLES

LIST OF FIGURES

SUMMARY

Silicon carbide armor, manufactured through solid-state sintering, liquid-phase sintering, and hot-pressing, is being used by the United States Armed Forces for personal and vehicle protection. There is a lack of consensus, however, on which process results in the best-performing ballistic armor. Previous studies have shown that hot-pressed ceramics processed with secondary oxide and/or rare earth oxides, which exhibit high fracture toughness, perform well in handling and under ballistic impact. This high toughness is due to the intergranular nature of the fracture, creating a tortuous path for cracks and facilitating crack deflection and bridging. However, it has also been shown that higher-hardness sintered SiC materials might perform similarly or better to hot-pressed armor, in spite of the large fracture toughness deficit, if the microstructure (density, grain size, purity) of these materials are improved.

In this work, the development of theoretically-dense, clean grain boundary, high hardness solid-state sintered silicon carbide (SiC) armor was pursued. Boron carbide and graphite (added as phenolic resin to ensure the carbon is finely dispersed throughout the microstructure) were used as the sintering aids. SiC batches between 0.25–4.00 wt.% carbon were mixed and spray dried. Cylindrical pellets were pressed at 13.7 MPa, cold-isostatically pressed (CIP) at 344 MPa, sintered under varying sintering soaking temperatures and heating rates, and varying post hot-isostatic pressing (HIP) parameters. Carbon additive amounts between 2.0–2.5 wt.% (based on the resin source), a 0.36 wt.% B_4C addition, and a 2050°C sintering soak yielded parts with high sintering densities (∼95.5–96.5%) and a fine, equiaxed microstructure (d_{50} = 2.525 μm). A slow ramp rate (10°C/min) prevented any occurrence of abnormal grain growth. Post-HIPing at 1900°C removed the remaining closed porosity to yield

a theoretically-dense part (3.175 g/cm^3, according to rule of mixtures). These parts exhibited higher density and finer microstructure than a commercially-available sintered SiC from Saint-Gobain (Hexoloy Enhanced, 3.153 g/cm^3 and $d_{50} = 4.837$ μm). Due to the optimized microstructure, Verco SiC parts exhibited the highest Vickers (2628.30 ± 44.13 kg/mm^2) and Knoop (2098.50 ± 24.8 kg/mm^2) hardness values of any SiC ceramic, and values equal to those of the "gold standard" hot-pressed boron carbide (PAD-B_4C). While the fracture toughness of hot-pressed SiC materials (~ 4.5 MPa$\sqrt{m}$) are almost double that of Verco SiC (2.4 MPa$\sqrt{m}$), Verco SiC is a better performing ballistic product, implying that the higher hardness of the theoretically-dense, clean-grain boundary, fine-grained SiC is the defining mechanical property for optimization of ballistic behavior.

CHAPTER I

INTRODUCTION

Ceramic armor (e. g. Al_2O_3, AlN, B_4C, SiC, and TiB_2) has been deployed by the United States Armed Forces since the 1960's and has undergone continuous evolution since then [1]. The dominant materials for this market are boron and silicon carbides, and aluminum oxide.

Until recently, boron carbide (B_4C) has been considered the best ceramic armor for personal protection because of its low theoretical density and high hardness. Commercially-available B_4C armor is manufactured via uniaxial hot pressing; sintering pure boron carbide to acceptable density has historically been difficult. Hot pressing has the additional advantage of densifying less-costly coarser-grained powder into acceptably-dense compacts ($\sim$98% relative density). However, complex-shaped parts cannot be fabricated through hot-pressing, and hot-pressing can introduce a fine-scale non-spherical porosity [2]. Boron carbide has been successfully pressureless-sintered to acceptable relative densities through use of second phase additives (e.g. Al_2O_3, SiC, TiB_2, AlF_3, and W_2B_5), which may promote activated sintering, liquid phase sintering, and/or inhibit grain growth [3, 4, 5, 6]. Carbon additives are effective sintering aids, and can react-away B_2O_3 coatings invariably formed on B_4C particle surfaces, yielding sintered bodies with $\sim$98% relative density [7]. However, all of these additives are detrimental to the hardness of the ceramic [8, 9]. Lee et al. used hydrogen gas to eliminate B_2O_3 particle coatings at a temperature below the onset of sintering, and rapid heating to a soak temperature to mitigate evaporation/condensation-based particle coarsening which was rapid relative to sintering in the lower portions of the sintering temperature range [10, 11]. In follow-up work, Cho et al. optimized soak

Table 1: Merit Factor for B_4C Armor Samples As Tested By Foster-Miller

Sample	Merit Factor
Supplier 1 "Gold Standard"	1.000
Supplier 2	0.993
Supplier 3 (Type 1)	0.818
Supplier 3 (Type 2)	0.871
Supplier 4	0.776
Verco B_4C	1.013

temperatures and times and used of a post hot-isostatic pressing (HIP) step on the closed-porosity sintered samples, bringing them to a fully pore-free state [2]. These optimizations led to the creation of a sintered boron carbide that has been shown to be superior to hot-pressed boron carbide armor currently on the market in a recent ballistic performance test by Foster-Miller (Table 1). B_4C, developed by Verco, was backed by composite coupons and shot with a 7.62mm $\times$ 51 NATO armor piercing (AP) round. The merit factor is an aggregate number based on the V_{50} value and the areal density of the part.

However, boron carbide armor has fallen out of favor in some circles for several reasons. Boron carbide has the highest Hugoniot elastic limit (HEL) of all ceramic materials. However, a large decrease in the ballistic performance of boron carbide under lower than expected impact rates and pressures is observed. Chen et al. found evidence of localized bands of amorphous boron carbide in the shards of material impacted at velocities above 850 m/s [12]. These localized bands were shown by TEM studies to be aligned in specific crystallographic directions, dissimilar from the direction of twins and stacking faults. Fanchini et al. followed with the discovery that the B_{12} (CCC) boron carbide polytype amorphized into B_{12} and amorphous carbon bands 2-3 nm wide, leading to the breakdown of the boron carbide structure and ultimately to failure at high impact velocities [13]. Also, boron carbide is produced in small quantities, and difficult to mill to sub-micron particle sizes, making sinter-grade powder cost-inhibitive.

In this work, the development of theoretically-dense, clean grain boundary, high hardness solid-state sintered silicon carbide (SiC) armor was pursued. There are various methods to create dense armor using solid-state sintering, liquid-phase sintering, and hot-pressing techniques; however, there is a lack of consensus into what processing, or what microstructural features, creates the best performing ballistic armor. Hazell et al. performed a test on the effectiveness of mosaic armor made from sintered SiC and hot-pressed (using liquid-phase sintering additives) SiC [14]. In his findings he found that not only did the sintered SiC exhibit a significantly lower depth of penetration (DOP) than the hot pressed SiC samples, but the DOP decreased the further the target was hit from its border and into the center. In the hot pressed sample, the DOP was comparable over all areas of the sample tile. Flinders et al. performed a study on the ballistic behavior of solid-state sintered SiC versus hot-pressed SiC to determine whether there was any advantage between any of the materials and to determine whether the mechanical behavior of the material would correlate with the ballistic behavior [15]. While the hot pressed SiC samples had almost a threefold increase in fracture toughness versus the sintered SiC samples, the DOP was greater, proving that increasing hardness resulted in a lower DOP and higher mass efficiency. The V_{50} testing also showed little variability between sintered versus hot-pressed samples. SiC-B performed slightly better over all other samples, and the argument for this was its high density (3.21 g/cm^3) and intergranular fracture, causing it to have a higher fracture toughness and therefore creating a more tortuous path for cracks during fracture. Adding to the argument between hardness and fracture toughness, ballistic properties were found to vary greatly depending on the type of backing/encapsulation used [16]. The right type of encapsulation could provide improved handling strength to the system as a whole, reducing the need for higher toughness armor.

It was then concluded that the best course of action for this work was to optimize

the solid-state sintering of SiC to create theoretically dense, clean grain boundary silicon carbide for ceramic armor use. It was hoped that the optimization of microstructure and hardness, as was done with the previous sintering optimizations of boron carbide, would yield a sintered SiC armor with superior ballistic properties to that of any other silicon carbide material currently on the market.

CHAPTER II

LITERATURE REVIEW

2.1 Silicon Carbide

Silicon carbide is used in a variety of high-wear, high-strength applications such as sandpaper grit, friction material in high-end brake applications, and for cutting tools. Applications also exist for SiC in electronic materials, where doped SiC materials are used in blue LED's, substrates, and diodes.

SiC is also used for ballistic armor. The SiC crystal structure is strong due to its high degree of covalent bonding. SiC is moderately light due to the low theoretical density of SiC, which is 3.211 g/cm^3 for α-SiC (6H) and 3.214 g/cm^3 for β-SiC [17]. The combined properties of high strength and low weight make SiC a desirable material for ground personnel and vehicle armor.

SiC is produced by the carbothermal reduction of silica (SiO_2), which is more formally called the Acheson process:

$$SiO_{2(s)} + 3C_{(s)} \rightarrow SiC_{(s)} + 2CO_{(g)}$$

SiC exists as a line compound along 50 mol % line in the silicon-carbon binary phase diagram, and exhibits a peritectic reaction at 2545°C. Under certain cases (depending on processing conditions) decomposition of SiC can occur far under the peritectic point, as low as 1700°C [17]. The silicon-carbon binary phase diagram is shown in Figure 1.

SiC can exist as two different crystal symmetries: α-SiC, formed at reaction temperatures above 2000°C, and β-SiC, formed at lower synthesis temperatures (1500-1600°C). α-SiC exists as a hexagonal (or rhombohedral) cell and can form various

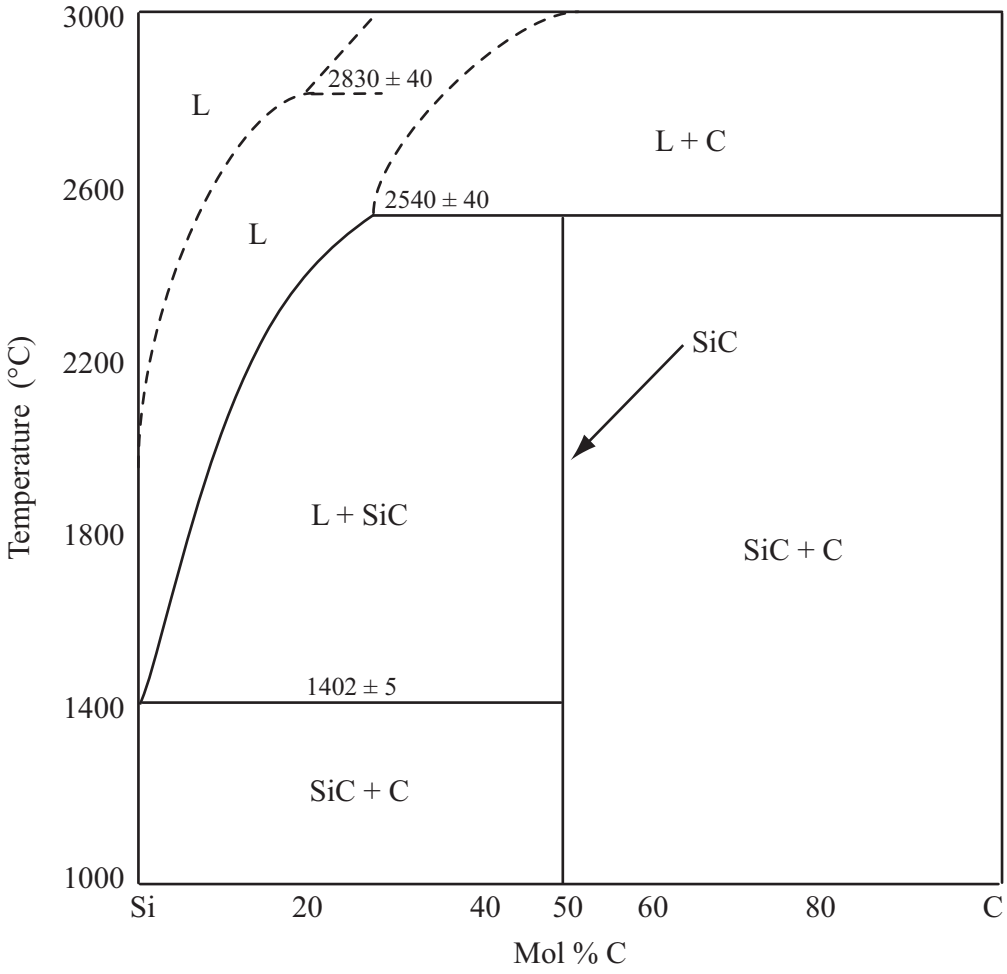

Figure 1: The silicon-carbon binary phase diagram [17].

Table 2: Listed Material Properties for Silicon Carbide

Density (g/cm^3)	Sintering Temperature (°C)	Young's Modulus (GPa)	Flexural Strength (MPa)	Hardness (GPa)	Fracture Toughness ($MPa\sqrt{m}$)
3.211-3.214	2100 [20]	475 [17]	350-600 [17]	24.5-28.2 [17]	4.6 [20]

structural polytypes (as many as 250 [18, 19]) based on the stacking of silicon and carbon layers in the close-packed (<0001>) direction. The most commonly available polytypes of α-SiC are 4H (ABACABAC stacking sequence) and 6H (ABCACBABC stacking sequence). β-SiC exists as a zinc blende structure (similar to the diamond structure). The close-packed (<111>) direction stacking sequence is always ABCABC.

Commonly listed material properties of SiC are listed in Table 2.1.

2.2 Sintering

Silicon carbide can be densified through sintering. Sintering is the process of heat treating a powder to produce atomic mass transport that densifies a powder compact through the creation of solid bonding between particles and through pore removal. Sintering processes can be classified into two sintering mechanisms: solid-state and liquid-phase sintering. For both cases, densification and grain growth occur during sintering, which can be modeled by

$$\Delta(\gamma A) = \gamma \Delta A + \Delta \gamma A \tag{1}$$

where γ is the interfacial energy (solid-vapor and solid-solid interfaces for solid-state sintering or solid-liquid and liquid-vapor for liquid-phase sintering) and A is the surface area of the particles [21]. $\Delta(\gamma A)$ describes the total change in the surface energy in a system with the combined effects of densification and grain growth. A change in surface area without a change in interfacial energy $\gamma \Delta A$ is coarsening which does not

Table 3: Mass Transport Mechanisms During Solid-State Sintering [22].

Mechanism	Path of Atoms	Result
Evaporation-Condensation	Surface to vapor to neck	Coarsening
Surface diffusion	Surface to neck	Coarsening
Adhesion	Surface to lattice to neck	Coarsening
Volume diffusion	Boundary or lattice to neck	Densification
Dislocation climb	Dislocation to neck	Densification
Grain boundary diffusion	Boundary to neck	Densification

lead to densification. Densification $\Delta\gamma A$ occurs when solid bonds are formed which removes pores from the interstices between grains, bringing grain centers closer to each other and changing the shape of the grain to accommodate into an arrangement that reduces the surface energy. The surface energy is a consequence of atoms on a free surface (such as a solid-vapor interface) having more free energy than atoms within the interior bulk of a material, due to the surface atoms having broken interatomic bonds. The equilibrium state of any natural process is the one with the minimum free energy, therefore it is the reduction of the surface energy which provides the driving force for particle sintering.

2.2.1 Solid-State Sintering

In solid-state sintering, densification occurs through lattice and grain boundary diffusion. A complete list of mass transport processes that can occur in solid-state sintering are listed in Table 2.2.1.

Solid-state sintering occurs in the absence of a wetting liquid. Many systems are sintered through this method to reduce any adverse material properties, such as loss of refractoriness, that could arise due to wetting liquids. The process by which a material changes through solid-state sintering can be classified into three stages. These are:

- First stage: Neck formation between adjacent particles through surface diffusion or evaporation/condensation processes. The atoms at the surface need less

driving force than interior atoms to undergo diffusion due to the excess free energy at the surface arising from the lower number of interatomic bonds that have to be broken, therefore surface diffusion is prevalent at the lower temperatures of sintering. Pore volume is decreased ∼10–12%. Particle surfaces are smoothed and surface area is reduced, however densification does not occur.

- Second stage: The necks between the particles grow. Grain boundary and lattice diffusion works to move atoms from grain interiors to fill vacancies and pores, reducing porosity and bringing the centers of grains closer together. Solid-vapor interfaces are replaced with solid-solid interfaces, which have less surface energy. Remaining porosity is pushed to the grain edges and forms an interconnected channel throughout the microstructure. Most of the shrinkage during sintering occurs in this step, as much as ∼20%.

- Third stage: Grain growth occurs during the last stage of sintering. Grains grow through bulk and grain boundary diffusion, thereby reducing the grain boundary area. Densification in this step is around 3–5%. Pores coalesce into the junction between three grain corners (triple point). Exaggerated grain growth during this step could lead to pore entrapment in grain interiors where removal becomes impossible, leading to lower densification.

At the beginning stage of sintering, necks between particles are formed. A sintering stress σ arises as a consequence of curvature at an interface, given by the Laplace equation

$$\sigma = \gamma \left(\frac{1}{R_1} + \frac{1}{R_2} \right) \tag{2}$$

where R_1 and R_2 are the radii of curvature [23]. A two-sphere model for neck formation is shown in Figure 2.

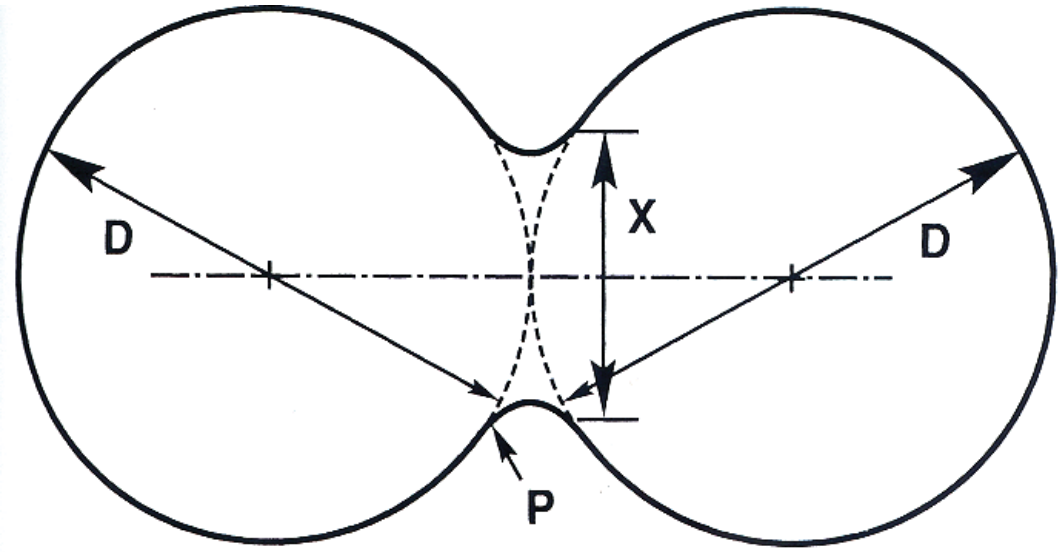

Figure 2: Two-sphere solid state sintering model for neck formation between two particles in contact [23].

The sign convention for the sintering stress is positive (tensile) for a radius beneath a convex surface, and negative (compressive) for a concave surface. The necks formed between particles are concave and therefore compressive in stress. The atoms in the neck region have more satisfied bonds than the atoms on the particle surfaces, which decreases the surface energy in the neck region and lowers the chemical potential. Also, the vapor pressure of the area around the neck is lower than the equilibrium vapor pressure. The neck region has a high stress gradient, where the sign of the stress changes from negative to positive in a small distance. The gradient, the reduced chemical potential, and the lower vapor pressure of the atoms in the neck provide a driving force for mass transport from the surface to the neck region. Surface diffusion and evaporation/condensation are the dominant mass transport mechanisms during the initial stages of sintering due to the free energy of the surface atoms. At the lower range of sintering temperatures, the temperature is not high enough to promote diffusion of atoms in the bulk interior.

The shrinkage rate $\frac{\Delta L}{L_0}$ with respect to grain size and temperature during the initial stages of sintering has been modeled as

$$\frac{\Delta L}{L_0} = \left[\frac{K D_V \gamma_S V_V t}{k_B T d^n}\right]^m \tag{3}$$

where d is the grain size, K is a geometric constant, D_V is the diffusivity of the vacancies in the volume V_V, and m and n are constants relating to the mass transport mechanisms being used. Later stages of sintering have many variables to consider because several mass transport mechanisms occur simultaneously, therefore this model is adequately rigorous to describe the sintering behavior beyond the first stage of sintering [24].

In the intermediate stage of sintering, after solid bridges between particles have formed through surface diffusion processes, densification of the part occurs through lattice (volume) diffusion of atoms from the particle interior to the neck and from diffusion of atoms through the grain boundaries. The driving force is the elimination of solid-vapor interfacial energy. The rate of lattice diffusion is dependent on the concentration of vacancies in the material, as vacancies are required to facilitate the diffusion of interior atoms to the neck regions. The vacancy concentration can be increased by raising the sintering temperature, since the vacancy concentration is exponentially proportional to temperature. The vacancy concentration can also be increased through adding sintering aids.

Vacancy concentration in the material is also a function of the curvature of particles during sintering. The effect of curvature on vacancy concentration C can be modeled using the following function

$$C = C_0 \left[1 - \frac{\gamma \Omega}{kT}\left(\frac{1}{R_1} - \frac{1}{R_2}\right)\right] \tag{4}$$

where C_0 is the equilibrium concentration (a function of temperature), γ is the surface energy, Ω is the atomic volume, T is the absolute temperature, and k is Boltzmann's constant [23]. For a concave surface, such as the neck between particles, the vacancy concentration is higher than the equilibrium concentration. Conversely, the vacancy

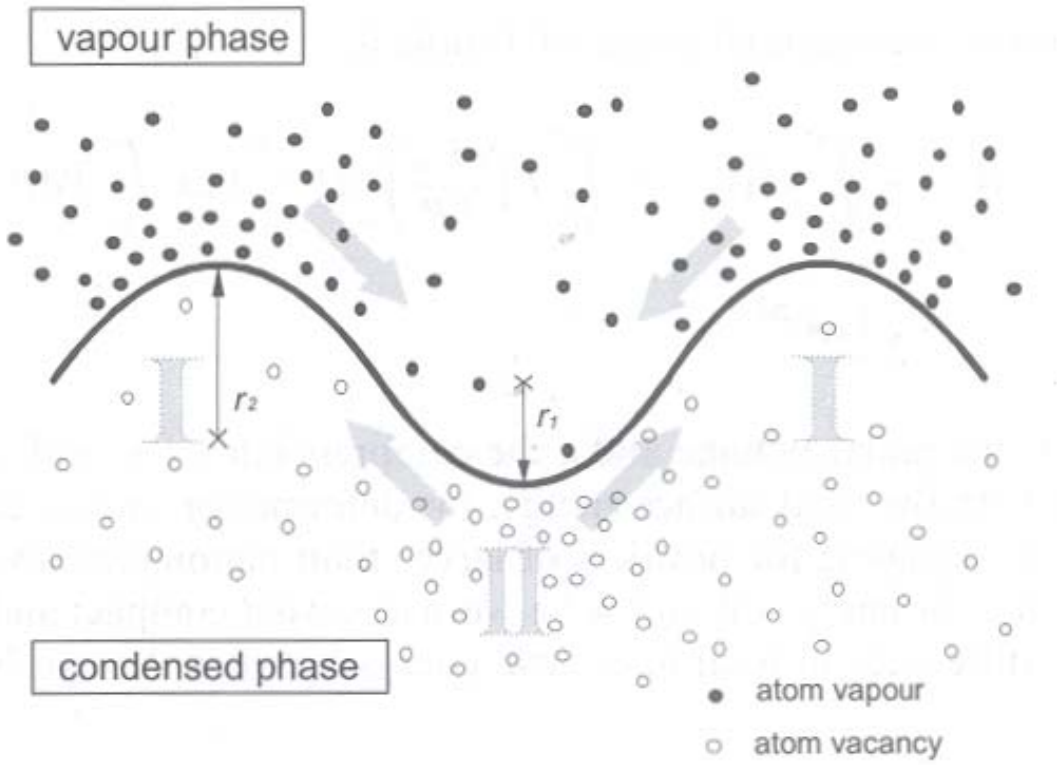

Figure 3: The effect of interfacial curvature on the vacancy concentration and vapor pressure of a solid-vapor interface. A concave surface exhibits a higher concentration of vacancies in the solid and a lower vapor pressure of the solid in the vapor [21].

concentration is lower than the equilibrium concentration for a convex surface, which describes the curvature of a particle surface. This provides a vacancy gradient for mass flow from the areas of low vacancy concentration to the areas of high vacancy concentration. The effect of curvature on vacancy concentration is illustrated in Figure 3.

Particles that have sintered together form grain boundaries between each other due to the mismatch in the lattice orientation between the particles. This mismatch lowers the activation energy needed for mass flow to occur, thus the rate of grain boundary diffusion is higher than lattice diffusion at lower sintering temperatures. The rate will depend on the type of boundary formed, which is a function of the angle of misorientation between the crystal lattices. Lattice diffusion will become

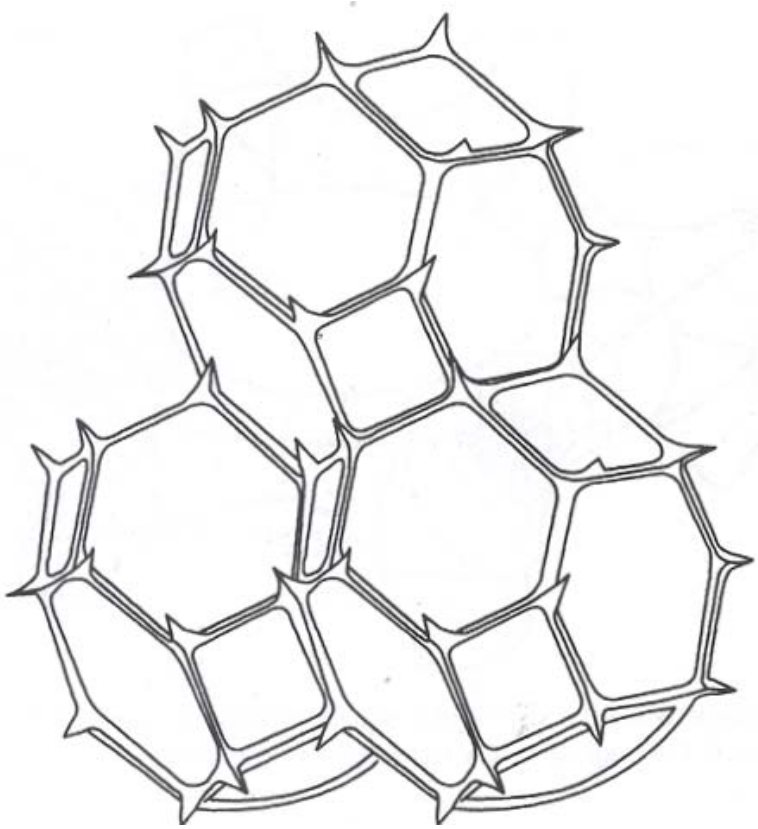

Figure 4: Pore and grain structure in the intermediate stage of sintering [23].

more dominant as the sintering temperature is increased.

Figure 4 shows the ideal case of the microstructure in the intermediate stage of sintering. The particle shape has changed from spherical to that of a tetrakaidecahedron, a shape with 14 sides. Vacancies are moved onto the tetrakaidecahedron edges and create an interconnected pore structure throughout the microstructure.

The final stage of solid-state sintering involves grain growth through movement of grain boundaries. As the interconnected pore structure begins to collapse, the pinning effect of pores on grain boundary migration diminishes and grain growth increases rapidly. The pore structure changes from the cylindrical interconnected pore shape to isolated pores on the grain edges and corners. The idealized model of the microstructure is shown in Figure 5. The ability of a pore to shrink depends on pore size, coordination number, and the dihedral angle (the internal angle formed

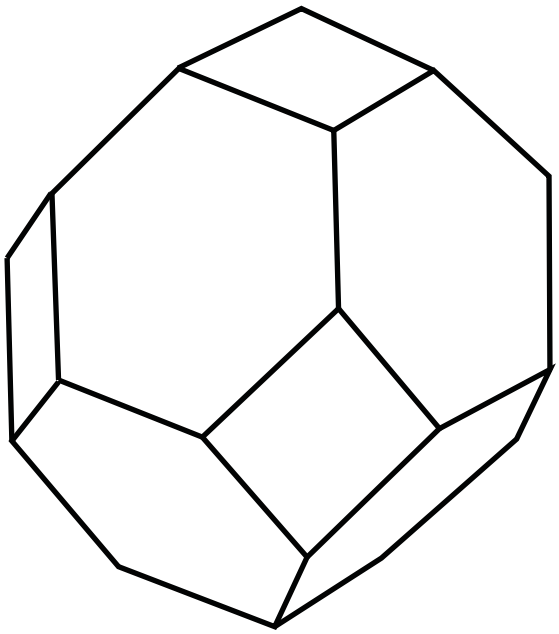

Figure 5: Pore and grain structure in the final stages of sintering [23].

from the intersection of two adjacent faces of two polyhedrons) between pores and grains. A pore size larger than half the average grain size will be stable and can grow. A large dihedral angle and a small coordination number (the number of grains surrounding a pore) will result in the shrinkage of a pore. Therefore, it is beneficial to obtain a high degree of packing and density in the powder consolidation process.

The rate of grain growth can be modeled according to the following relation

$$d_t^n - d_0^n = 2AM_b\gamma_b t \tag{5}$$

where d_t is the mean grain size after time t, d_0 is the original mean grain size, A is a geometric constant, M_b is the mobility of the grain boundary, and γ_b is the interfacial energy of the grain boundary. The exponent n is observed to have a value of 2–3 (for normal grain growth). The driving force for grain growth comes from the difference in chemical potential across the curvature of the boundary between grains. Grain boundary curvature is a result of equalizing grain boundary tensions between three grains coming into contact at a triple point. To balance the grain

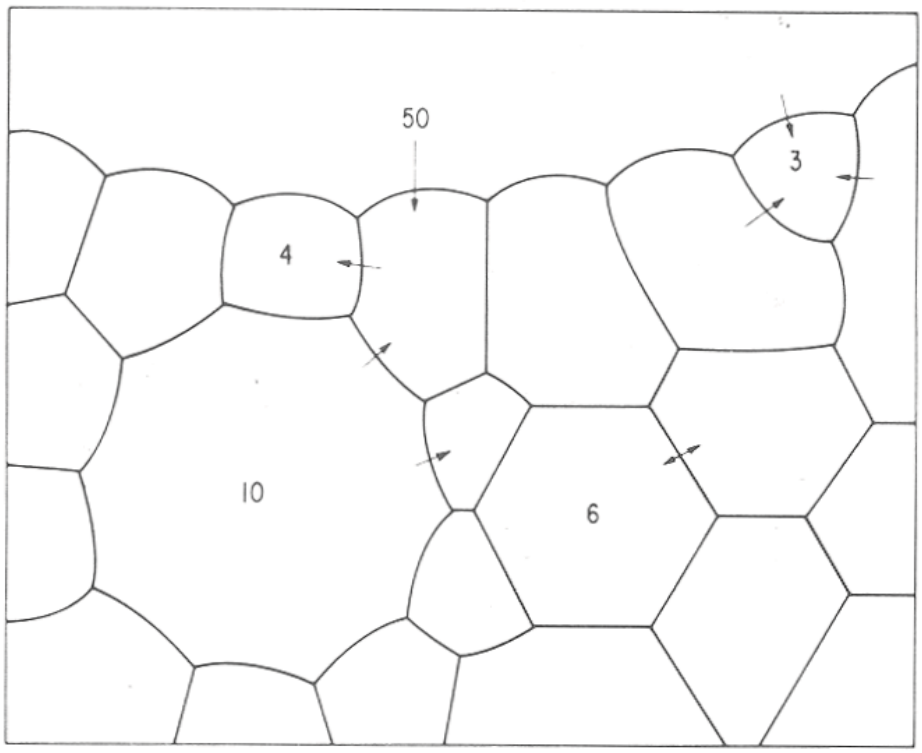

Figure 6: The effect of boundary curvature on grain growth. Grains with concave boundaries grow and those with convex surfaces shrink. Unusually large grains in a matrix of fine grains grow quickly, causing pore entrapment and a reduction in densification [24].

boundary tension, all grain boundaries must be separated by 120° (looking at the plane perpendicular to the intersection of the boundaries). A hexagon naturally has 120° angles between sides, thus a grain with six sides would have flat boundaries with chemical potential being equal on both sides. Grains with lower than six sides will develop convex boundaries (relative to the radius) and grains with more than six sides will develop concave boundaries. The curvature will flatten by the diffusion of atoms in the opposite direction. Since the driving force exists to remove grain boundary area, grains with convex surfaces will shrink while grains with concave surfaces will grow. A representation of the effects of boundary curvature on grain shrinkage and growth is shown in Figure 6.

Abnormal grain growth and pore coarsening can occur during the final stage of

sintering, which leads to a decrease in densification and could lead to degradation in material properties. Abnormal grain growth (or exaggerated grain growth) occurs when grains in a local area grow rapidly due to high grain boundary mobility as compared to the bulk of the microstructure. Causes of abnormal grain growth include the presence of large particles or agglomerates in as-pressed consolidated powder, non-uniform distribution of second-phase particles, and high concentrations of impurities. The distinction between normal and abnormal grain growth can usually be seen from the size distribution of grains after sintering. If the size distribution of grains does not change over annealing time at the sintering temperature, then the grain growth is normal. An abnormal grain growth result would show a broadening of the size distribution over time, and in some cases the creation of a bimodal grain size distribution. Pore coarsening is the process of trapped pores in the grains growing through an Ostwalt ripening process, where the smaller pores shrink and the larger pores grow due to curvature effects. Both processes can cause a loss in densification and degradation of material properties.

2.2.2 Liquid Phase Sintering

Sintering in the presence of a wetting liquid is the process known as liquid phase sintering. As with solid-state sintering, the driving force for the sintering process comes from the reduction of surface energy. However, liquid phase sintering can promote high densification rates and low sintered porosity in materials through lower temperatures than required for solid-state sintering. Because of this, the tendency for exaggerated grain growth to occur during sintering is reduced [25]. The requirements for achieving maximum densification during liquid phase sintering [26] are

1. An appreciable amount of wetting liquid.

2. Complete wetting of the solid particles.

3. A sensible amount of solubility of the solid into the liquid phase, and conversely a low liquid solubility into the solid.

The amount of wetting liquid varies depending on the characteristics in the system being sintered. In theory, a mono-sized packing of spheres (with a packing efficiency of 74 vol.%) would need 26 vol.% liquid to achieve full theoretical density, however a lower percentage of liquid has been used to achieve complete densification in SiC systems ($<$ 10 vol.%) [27].

The wetting of the second phase liquid onto the solid is one of the most important factors during liquid phase sintering. A wetting liquid spreads over a solid to reduce the free surface energy of a system. The surface tensions between a solid, liquid, and gas can be modeled using the following relationship

$$\gamma_{SV} = \gamma_{SL} + \gamma_{LV} cos\theta \tag{6}$$

where γ is the surface tension between solid-vapor, solid-liquid, and liquid-vapor surfaces. At the equilibrium contact angle, the interfacial energies are balanced. A liquid will wet a surface of a solid to reduce a high γ_{SV}. Wetting also occurs if γ_{LV} is lowered, or if a reaction between the liquid and the solid results in a lower γ_{SL}. A completely wetting solid ($\theta = 0^{\circ}$) is needed to fill the channels between particles to provide the capillary force needed for particle rearrangement, and the path for mass transport through a solution/precipitation process. An incomplete wetting liquid (liquid with a high wetting angle) will tend to form isolated islands of liquid between solid particles and also push to separate particles, causing swelling of the compact. If the particles come into contact they will undergo densification analogous to a solid-state sintering process, where mass transport is by volume diffusion instead of a solution/precipitation process. An illustration of the effect of wetting angle on the behavior of the solid-liquid surface is shown in Figure 7. Wetting behavior can vary due to presence of surface defects (which would increase the contact angle and reduce

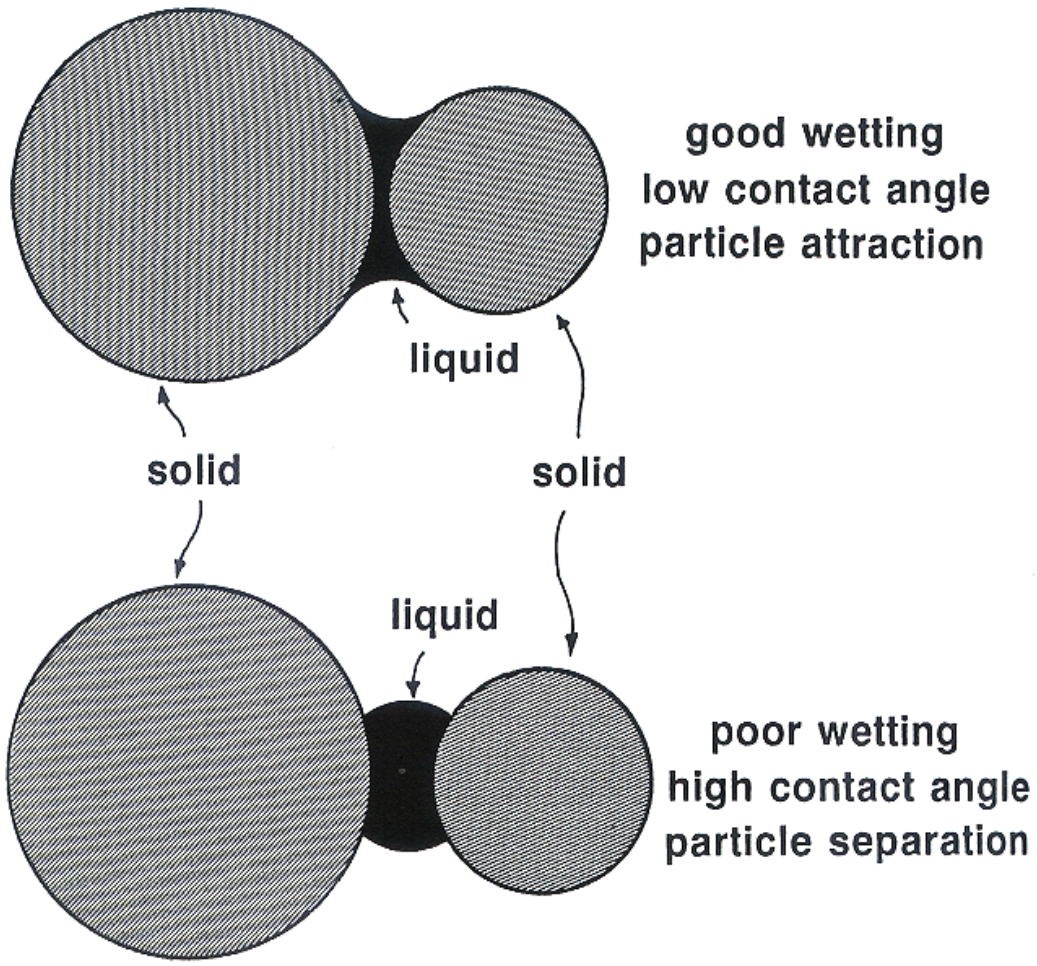

Figure 7: Effect of the liquid-solid contact angle on the wetting of the solid. The top diagram illustrates an attractive force between particles due to a low contact angle and high wetting. The lower diagram illustrates particle separation due to a high contact angle and low wetting [23].

wetting), or due to changes in temperature. A higher sintering temperature will increase the solubility of the solid and decrease the contact angle of the liquid [23].

A fully wetting liquid exerts a capillary pressure that pulls the particles in the compact into a tighter and denser arrangement. Upon melting, the liquid flows into the small capillaries between particles, as fast as 2 μm per second, and leaves a pore behind. Using smaller sized particles in the melting phase will benefit as it leaves smaller pores behind and melts at a lower temperature due to the increase in solubility of the higher surface area particles. The amount of capillary (or contact) force is a

function of the pressure difference ΔP across the curvature of the liquid. This pressure difference is also dependent on the amount of liquid present, the contact angle between the liquid and solid, and particle size of the solid. The pressure difference across a curve surface is analogous to the sintering stress described earlier in which

$$\Delta P = \gamma_{LV} \left(\frac{1}{R_1} + \frac{1}{R_2} \right) \tag{7}$$

where γ_{LV} is the interfacial energy of the liquid-vapor surface. Using a two sphere model for liquid phase sintering, which is illustrated in Figure 8, a relationship for the capillary force F exerted on the solid particles can be derived:

$$F = \frac{\pi}{4} X^2 \Delta P + \pi X \gamma_{LV} \cos \psi \tag{8}$$

where ΔP is the pressure difference, X is the meniscus diameter, γ_{LV} is the interfacial energy of the liquid-vapor surface, and ψ is an angle representing the curvature of the liquid meniscus [23]. As the contact angle θ decreases toward zero, the capillary force in the liquid becomes increasingly larger and attractive. The transition between attractive and repulsive forces of the liquid on the solid particles will occur around a contact angle value of 60°.

For densification of the solid through a solution/precipitation process, the solid must be soluble in the liquid. The amount of solid solubility into the liquid preferred for liquid phase sintering is typically between 1–20 vol.%. Sintering temperatures are generally chosen slightly above the eutectic temperature where the liquid solubility into the solid is low. A high liquid solubility into the solid will result in formation of a transient liquid and swelling of the compact.

The viscosity of the liquid is an important variable during the sintering process. The viscosity is dependent on the sintering temperature and the composition of the liquid phase. The sintering rate is inversely proportional to the viscosity of the liquid, therefore, the viscosity must be low enough for particle wetting, rearrangement, and

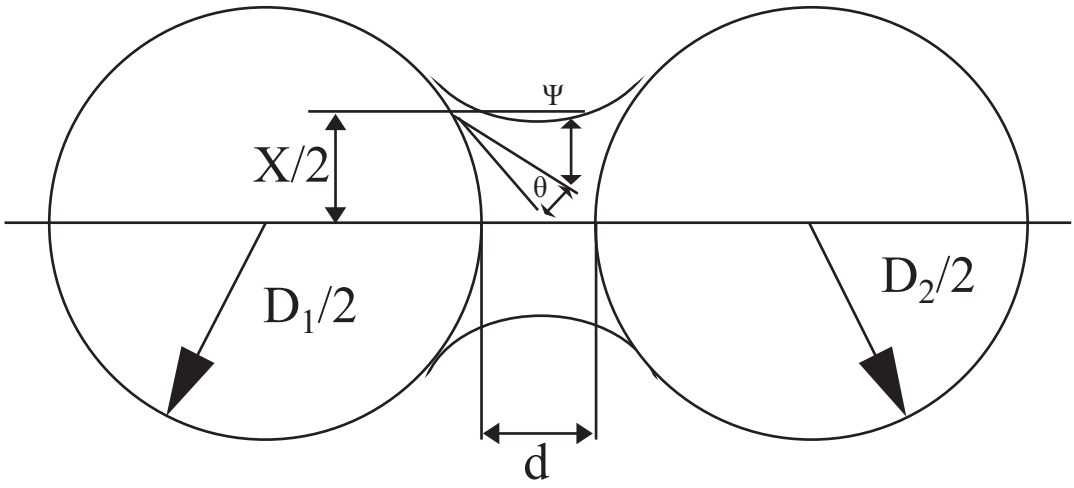

Figure 8: Two-sphere LPS model used for the calculation of the capillary force exerted by the liquid. [28].

solution/precipitation to occur efficiently. However, too low of a viscosity can lead to slumping of the consolidated part during sintering [26].

Liquid phase sintering has been described by Cannon and Lenel [29] as a three step process:

1. Formation of a fully wetting liquid phase that provides substantial capillary pressure, bringing particles together into a tighter fitting and more dense rearrangement while still keeping a thin film (< 1 μm) of liquid between the solid particles.

2. Densification of the part occurs through a solution/precipitation process in where atoms are preferentially dissolved from smaller particles into the liquid and precipitate on larger particles in the matrix. The rate and extent of the solution/precipitation process is a function of the amount of solubility of the solid into the liquid. The solubility of a solid into a liquid phase is modeled by

the function

$$\ln \frac{C}{C_0} = \frac{4\gamma_S L\Omega}{DkT} \tag{9}$$

where C is the solubility, C_0 is the equilibrium solubility, $\gamma_S L$ is the interfacial energy of the solid-liquid interface, Ω is the atomic volume, D is the particle diameter, k is Boltzmann's constant, and T is temperature. The solubility of the solid is a function of the temperature and of the particle diameter. Small particles with larger curvature have higher solubility than larger, more stable particles and dissolve into the liquid. This establishes a concentration gradient of atoms from the small to large particles. The atoms in the liquid diffuse and then precipitate onto the larger particles, which causes pore elimination through grain shape adjustment.

3. Final sintering stage, in which the densification process was assumed by Cannon and Lenel to be similar to a solid-state sintering mechanism.

However, Kingery [26] stated that there were issues with this generally accepted explanation. He pointed to solubility data with respect to particle size in the $Fe_{(s)}$-$Cu_{(l)}$ system, which undergoes densification through LPS, and showed that the extent of disparity in solubility between small and large particles is not sufficient enough to provide the driving force for the solution/precipitation process described above. Evidence is also shown that particles in certain systems will change shape to accommodate packing and provide maximum densification. Even particles with relatively large radii of curvature were shown to change shape and create smaller radii of curvature, which is again in contradiction to the model described above.

Kingery's proposed model and theory for microstructural evolution through LPS attributes the driving force for densification to the increased pressure at the points of contact between solid particles separated by thin liquid capillaries. When the liquid

first forms and flows between particles, the capillary pressure exerted by the liquid will first densify the part by rearrangement of the particles to a tighter packing fit. After this is accomplished, the driving force for densification then comes from the increased pressure at the solid contact points. At these points of contact, the compressive force on the particle caused by the capillary pressure of the liquid is substantially larger. This increase in pressure at the contact point leads to an increase in the chemical potential of the solid atoms at those points. The amount of chemical potential increase can be calculated through the free energy relation

$$dG = -SdT + VdP \tag{10}$$

where G is the Gibbs free energy of the system [26]. For a single component in the system i, the chemical potential μ_i is related to the molar Gibbs free energy of the component $\overline{G_i}$

$$\mu_i = \overline{G_i} = \left(\frac{\partial G}{\partial n_i}\right)_{T,P,n_i \neq n_j} \tag{11}$$

Through the relationship between chemical potential and Gibbs free energy it is possible to obtain the effect of pressure on chemical potential of a component.

$$\begin{aligned} d\mu_i|_T &= d\overline{G_i}|_T \\ d\mu_i|_T &= \overline{V}dP|_T \\ \int_{\mu=\mu_0}^{\mu} d\mu &= \int_{P=P_0}^{P} \overline{V}dP \\ \Delta\mu &= \overline{V}\Delta P \end{aligned} \tag{12}$$

The activity a can be found through the chemical potential and thus can be found as a function of pressure, surface tension and pore radius.

$$\begin{aligned} \Delta\mu &= RTln\frac{a}{a_0} \\ ln\frac{a}{a_0} &= \frac{\overline{V}\Delta P}{RT} \\ ln\frac{a}{a_0} &= \frac{2\gamma_{LV}\overline{V}}{rRT} \end{aligned} \tag{13}$$

In these relationships, P_0 and a_0 are the equilibrium pressure and activity at the given temperature.

The increase in activity and chemical potential of the atoms due to the increased pressure at the contact points is what drives the further densification of the part. Atoms at the contact points melt into the liquid and diffuse to precipitate on areas of lower pressure (with lower chemical potential and activity), causing densification contradictory to the Price-Smithells-Williams model where solubility is the primary factor. Instead, the grains undergo contact flattening and change shape to fill available space, even under conditions where the curvature of the growing interface is increasing. As the grain shape changes, the pore space continuously shrinks. The Kingery model is suitable for describing the densification behavior observed through liquid-phase sintering and is traditionally referred to as the classical model.

Kingery's classical model and theory have been used to explain most liquid phase sintering processes, however, Kwon and Yoon [30] argued that there were inherent problems with Kingery's model and theory. In the intermediate stage where grain shape changes due to contact flattening, the pores are assumed to continuously decrease in size with time. However in real systems, the frequency of small pores decreases and the frequency of large pores remains constant until the final sintering stage [21]. Also, the microstructure formed through liquid phase sintering does not exhibit much, if any, change in grain shape [31]. The theory also assumes that the liquid film exists throughout all the grains, however, most systems do not exhibit a fully wetting liquid (0°) and therefore particles will come into contact and densify

through volume diffusion processes. This has been proved by the fact that the densification kinetics observed are faster than predicted for contact flattening, which is an indication that the contact flattening mechanism is not the dominant densification mechanism.

A pore-filling model was proposed by Kwon and Yoon which described the microstructural change in liquid phase sintering through the behavior of the liquid phase rather than the solid particles [30]. A three-stage model was suggested for the pore filling densification mechanism:

1. liquid coagulation
2. liquid redistribution
3. liquid filling of pores

The total liquid-vapor interfacial energy is reduced through liquid flow in the coagulation stage, and a homogeneous microstructure with a uniform distribution of pores is obtained in the redistribution stage. Both stages are quick and occur at the initial stage of liquid phase sintering. Kwon and Yoon argue that the overall densification kinetics are governed in the pore filling stage.

The driving force for the pore filling mechanism is provided by the instability of the pressure in the wetting liquid. When the liquid initially melts, it is pulled by capillary action around the solid particles and leaves a pore where the liquid initially resided as a solid. Initially, the pressure of the gas atmosphere surrounding the compact and the pressure of the gas inside the pore are equal, creating an equal hydrostatic liquid pressure throughout the part. After the initial liquid formation and solid rearrangement, further densification of the solid occurs through grain growth of the solid, as opposed to the contact flattening mechanism in the Kingery model. During grain growth, the radius of curvature of the liquid meniscus surrounding the solid particles on the surface and the solid particles surrounding the pore increases. After

a certain point the liquid radius of curvature becomes large enough to completely wet the surface of the pore wall. At this critical point, the liquid meniscus is constricted on the pore wall, however, the menisci on the surface are free to continue to increase. This produces pressure instability in the liquid causing the wetting liquid to fill the pore. The filling of the pore with the liquid reduces the pressure of the liquid and increases the capillary pressure due to the decrease of the fraction of liquid separating the grains. A graphical illustration of this model is shown in Figure 9. Microstructural coarsening due to grain growth then begins in the liquid filled pore region to homogenize the microstructure. As grain growth occurs in the liquid-filled pore volume, liquid is pushed out from the filled pore an back into the liquid filled capillaries surrounding the grains.

Based on the pore-filling model proposed by Kwon and Yoon, Lee and Kang proposed the pore-filling theory [32]. The theory was developed to evaluate the critical condition needed for pore filling, which is a function of the effective volume fraction of the liquid and liquid meniscus radius. The liquid meniscus radius is a function of the size and packing of grains, the wetting and dihedral angles, the ratio of the liquid-vapor to solid-liquid interfacial energies, and the effective liquid volume fraction. The effective liquid volume fraction f_l^{eff} is calculated by taking into account the initial volume fraction of the liquid f_l^i, the volume of the liquid-filled pores, and the volume of the homogenized pores. The homogenized pore volume refers to the volume of the pore during the homogenization process of the liquid-filled pore through grain growth. It is inferred that when the microstructure is completely densified, the effective volume fraction will reach the initial volume fraction (since the part will be completely homogeneous and void of liquid-filled pore volume). The homogenized volume V_{homo}^j of a liquid pocket j can be modeled as

$$V_{homo}^j = -\int_0^t 4\pi r^2 \left(\frac{dr_\tau}{d\tau}\right) d\tau \tag{14}$$

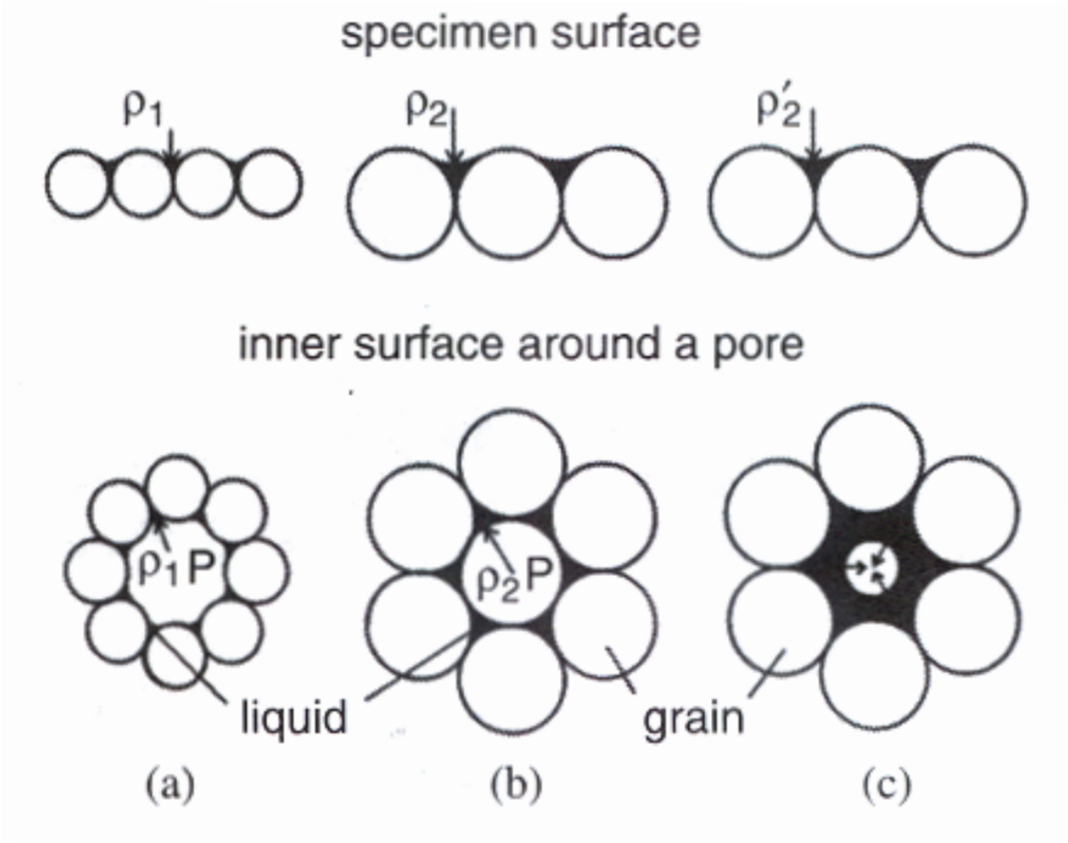

Figure 9: Pictoral representation of the pore-filling model: (a) grains and liquid before pore filling, (b) the critical criteria for instability, where the liquid meniscus fully wets the pore surface, and (c) liquid filling of the pore after the critical instability. ρ is the radius of curvature for the liquid meniscus, where $\rho_1 < \rho_2 < \rho_2'$ [21].

where r_τ is the radius of the liquid pocket j at time $t = \tau$. The effective liquid volume fraction f_l^{eff} can be calculated through

$$f_l^{eff} = \frac{V_l^i - \Sigma_{j=k+1}^{n}(V_p^j - V_{homo}^j)}{V_s^i + V_l^i - \Sigma_{j=k+1}^{n}(V_p^j - V_{homo}^j)} \tag{15}$$

V_l^i is the initial volume fraction of liquid present in the compact, V_s^i is the initial solid volume, V_p^j is the volume of the pore filled with liquid.

According to Kwon and Yoon, liquid filling of pores will result in densification (an increase in Archimedes density), but will not result in volume shrinkage. Conversely, homogenization of liquid-filled pores will result in shrinkage. Both processes are independent of each other, unlike solid-state sintering, and occur simultaneously through the sintering process. Therefore, Lee and Kang developed different models to predict the density ρ and compact shrinkage $1 - \frac{l}{l_0}$, given by

$$\rho = 1 - \frac{\Sigma_{j=n+1} V_p^j}{V_s^i + V_l^i - \Sigma_{j=n+1} V_p^j} \tag{16}$$

$$1 - \frac{l}{l_0} = 1 - \left(1 - \frac{\Sigma_{j=k+1}^{n} V_{homo}^j}{l_0^3} - \frac{\Sigma_{j=1}^{k} V_p^j}{l_0^3}\right)^{\frac{1}{3}} \tag{17}$$

where l is the dimension of the compact at time t, and l_0 is the initial compact dimension.

The critical radius for the pressure instability to occur is linearly related to the pore size and grain size, therefore during grain growth small pores will fill with liquid before large pores. A small particle size for the liquid forming additive would be beneficial, since smaller pores would be left behind after the initial liquid formation and capillary flow, and would fill with liquid sooner than larger pores. Also, since the sintering is a grain growth-limited process, Kang argues that densification of the part is enhanced through use of a coarser powder as opposed to a finer one [33].

2.2.3 Hot Pressing

Another method to exploit solid-state or liquid-phase sintering is through use of either method along with the application of an external pressure. This is referred to as hot pressing. The application of an external pressure P_e increases the driving force for sintering densification P_T by acting against the internal pore pressure P_i [47].

$$P_T = P_e + \frac{2\gamma}{r_p} - P_i \tag{18}$$

The added energy of the applied pressure decreases the need for severely high sintering temperatures to supply the driving force for densification, thereby reducing the tendency for exaggerated grain growth. Using lower sintering temperatures keeps the microstructure finer, more equiaxed, and enables the densification of powders without use of second-phase additives, when purity is important. Coarser, and therefore cheaper, powders can be processed to high density as well. However, the graphite dies used are expensive to make and maintain. Also, parts are gang-pressed, which prohibits the development of geometrically complex shapes. Therefore, the use of hot pressing in industry is limited to certain processes.

Hot-isostatic pressing (HIPing) is similar to hot pressing. However, instead of a mechanically acting force applying the external pressure, the pressure is exerted on the part by use of a gas (usually argon or nitrogen). HIPing can be done in temperatures up to 2200°C and 200 MPa of gas pressure. An advantage to the process is the elimination of expensive die materials, and the ability to process parts of high geometric complexity. Commercially, most HIPing is performed to remove or reduce the extent of closed porosity in metal castings. Parts can be encapsulated in a powder bed and surrounded be a metal can, or in a fused silica casing if open porosity exists on the part. In recent years, HIPing has been used to remove the closed porosity in un-encapsulated ceramic bodies, providing the part had no open porosity [2].

2.3 Silicon Carbide Sintering

Silicon carbide densification has been thoroughly studied over the past few decades. Prochazka et al. [34] was the first to effectively create dense SiC structures through solid-state sintering. Fine β-SiC powders (130 nm) were oxidized in air to remove excess carbon and to simultaneously form an SiO_2 coating over all the particles. The oxide was then removed from the powder by leaching the powder in a 20% HF solution and washing it with alcohol and water. 0.5 wt.% Phenolic resin and 0.36 wt.% B_4C were added as sintering aids. Sintering the compacts in a flowing He atmosphere at 2100°C yielded parts that were 96.4% dense. These parts had great wear, corrosion, and creep resistance. However, using HF to leech the silica off the particles is not effective for a large manufacturing process, and is a hazard to work with. Also, the problem of low fracture toughness ($\sim$2.5 MPa$\sqrt{m}$) and exaggerated grain growth led to the search for other methods of densification that would lead to higher density, finer-grained compacts with enhanced strength.

Various explanations have been proposed for the effect of boron and carbon on the sinterability of SiC. Oxygen, existing in a silica layer on the silicon carbide particle surfaces reacts unfavorably with the silicon carbide particles to create SiO and Si vapor at 1870°C and 1950°C, respectively. Datta et al. suggests that carbon deters these reactions by reducing the silica layer,

$$SiO_{2(s)} + 3C_{(s)} \rightarrow SiC_{(s)} + CO_{(g)}$$

at 1520°C [36], well before the vapor producing reactions are thermodynamically favorable. However, it has been argued recently [35] that additions of carbon are not necessarily needed for de-oxidation of the silica layer, and that SiC works to perform that task as well as any addition of carbon. It is argued that the carbon works to chemically bond the gaseous products of that SiC-SiO_2 reaction

$$SiO_{2(s)} + nSiC_{(s)} \rightarrow Si_{(g)} + SiO_{(g)} + CO_{(g)} + (n-1)SiC_{(s)}$$

leaving only the evolution and vaporization of CO, reducing the amount of weight loss in the sample. Stobierski et al. also propose that carbon works to eliminate solid-vapor mass transport mechanisms and pin grain boundaries to reduce grain growth. It is proposed that boron exhibits limited solubility into the crystal structure of silicon carbide, substituting into both silicon and carbon lattice positions and creating vacancy paths for bulk diffusion [36]. Another argument for the sintering enhancement is that the boron creates an Si-B-C liquid phase [37]. Stobierski argued that the high degree of densification (90% densification in the first 60 seconds) and the grain morphology suggest a liquid-phase sintering mechanism provide high capillary pressure, and grain rearrangement through contact flattening.

Lange et al. first demonstrated the merits of liquid-phase sintering (LPS) of SiC using Al_2O_3 [38]. The added Al_2O_3 forms a eutectic liquid with the SiO_2 coating that exists on the surface of SiC particles at temperatures as low as 1597°C [39]. This second phase liquid assists in particle rearrangement and densification through solution/precipitation of SiC, which eliminates the need for high sintering temperatures and thus eliminates the problem of exaggerated grain growth. The drawback to using Al_2O_3 as an additive is the resulting reaction between Al_2O_3 and SiC:

$$SiC_{(s)} + Al_2O_{3(s)} \rightarrow SiO_{(g)} + Al_2O_{(g)} + CO_{(g)}$$

The gases formed from this reaction trap themselves as pores in the microstructure, which limits the extent of densification during sintering.

To eliminate pore formation due to gas reactions, Mulla et al. sintered using similar conditions while also applying an overpressure of CO (0.105 MPa) to suppress the reaction from moving forward to gaseous formation. This technique produced sintered compacts with a relative density ∼98%. From XRD and SEM analysis,

Mulla discovered that around 50% of the β-SiC phase transformed into α-SiC during sintering [40].

Sintering methods using mixtures of alumina and rare earth oxides were researched. Parthasarathy et al. sintered SiC using LPS and with an addition of Y_2O_3 into the liquid phase former material. Al_2O_3 and Y_2O_3 form a eutectic liquid at 1826°C [41]. During cooling, this liquid formed two secondary phases in the grain boundaries: yttria-alumina garnet and alumina [42]. She et al. [27] explored LPS through use of Al_2O_3-Y_2O_3 liquid formers powders. It was discovered that a 10 wt.% mixture of additives with a 25–50% Y_2O_3 content exhibited the least amount of evaporation of Al_2O_3 from the part at the higher sintering temperatures and produced the highest densification (98%). Vaporization of liquid and solid phases during sintering was reduced by embedding compacts in a powder bed of the powder material. She also observed that there needed to be at least 5–10 wt.% liquid forming additive addition in the powder mixture. With a 5 wt.% or lower addition of liquid forming additives not enough liquid is created to enable the solution/precipitation process [40], and the resulting microstructure exhibits a skeletal sintering structure.

Realizing the phase change of SiC during LPS, discovered by Mulla, could be exploited to tailor the mechanical behavior of the sintered body, Rixecker et al. [43] explored the β to α transformation. Rixecker used a mixture of AlN-Y_2O_3 as a substitution for the Al_2O_3-Y_2O_3 additive mixture. An overpressure of nitrogen (0.1 MPa) was used to deter formation of gaseous species, therefore a powder bed to embed parts was not needed. The highlight of their work was the study of the improvement in the mechanical behavior of the SiC microstructure due to the change in phase of the SiC powder during sintering. A mixture of 10 vol.% α-SiC and 90 vol.% β-SiC was sintered at 1950°C for 30 minutes, which brought the parts to theoretical density. Following the sintering soak, a second sintering soak was performed at 1925°C for 16 hours. During the heat treatment, the β-SiC to α-SiC reaction occurs. The β-SiC

particles, which are not stable at the high sintering temperature, dissolve into the second phase liquid. This solute from the dissolved β-SiC particles precipitate onto the thermodynamically stable α-SiC grains. The α-SiC grains, hexagonal in structure, grow anisotropically into elongated platelets due to the relatively low volume percent of nucleation sites. The prism planes have a much faster kinetic growth rate than the basal planes, which is the reason for the high aspect character of the grain growth. Also, the kinetics of the β to α transformation are very slow, which necessitates the need for the 16 hour soak time. The microstructure formed from this sintering and growth process is shown in Figure 10.

The elongated α-SiC microstructure exhibits interesting mechanical properties. The fracture toughness of the material increased dramatically from 4.6 up to as much as 6.5 MPa$\sqrt{m}$ during the heat treatment. This data is shown in Figure 11. Interestingly enough, the same study, it was shown that a pure 100% α-SiC powder compact exhibited no appreciable change in fracture toughness through the exact heat treatment process as the mixed-mode powder. It is inferred that the cause was the inability of the α-SiC grains to grow into elongated platelets because of the impingement of its neighboring α-SiC grains in the microstructure.

The increase in fracture toughness of the elongated platelet microstructure can be attributed to several phenomena. First, it was shown by She et al. [27] through analyzing SEM images of fracture surfaces in LPS-SiC materials that the fracture mode for these LPS materials is intergranular, as opposed to the transgranular fracture exhibited in pure-phase solid-sintered materials. Therefore, the fracture path of the elongated microstructure is more tortuous than that of an equiaxed, fine-grained microstructure such as the pure α-SiC seeded microstructure shown in Figure 12. Also, crack bridging is exhibited due to mismatch in the thermal expansion coefficients of SiC and of the secondary phases. The difference in CTE between the SiC phase and the second-phase material causes stresses to develop between the interface,

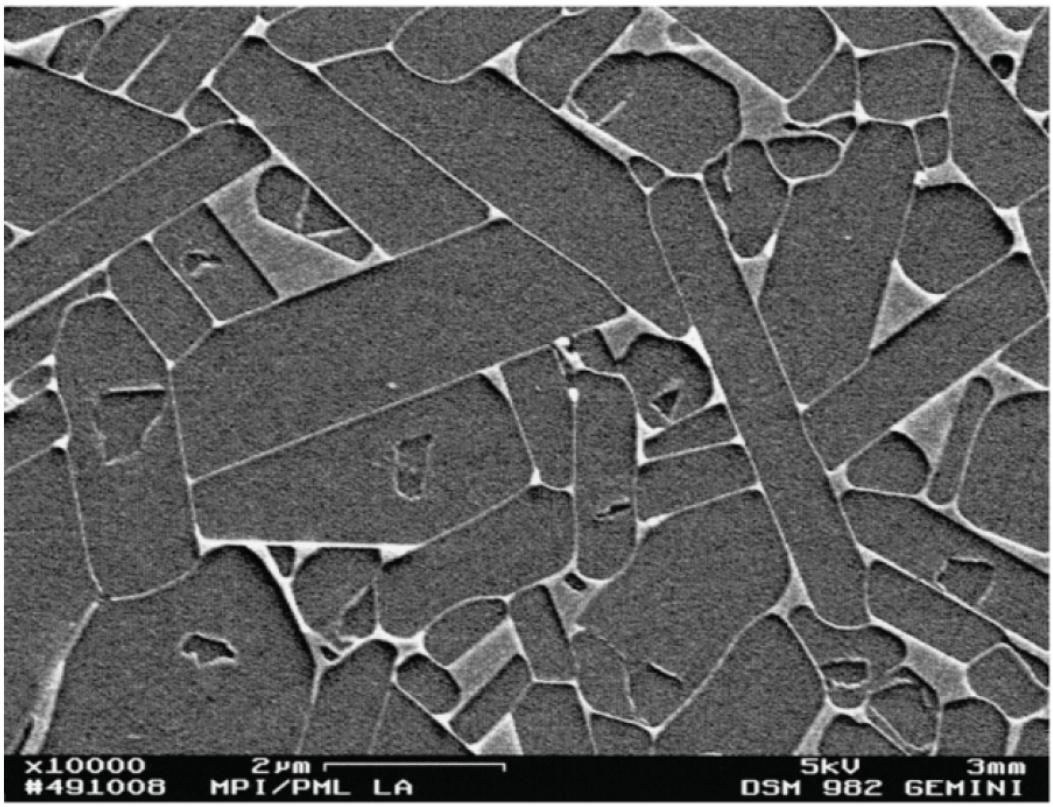

Figure 10: The elongated α-SiC platelet microstructure formed from the sintering of a mixture of α and β SiC powders [43].

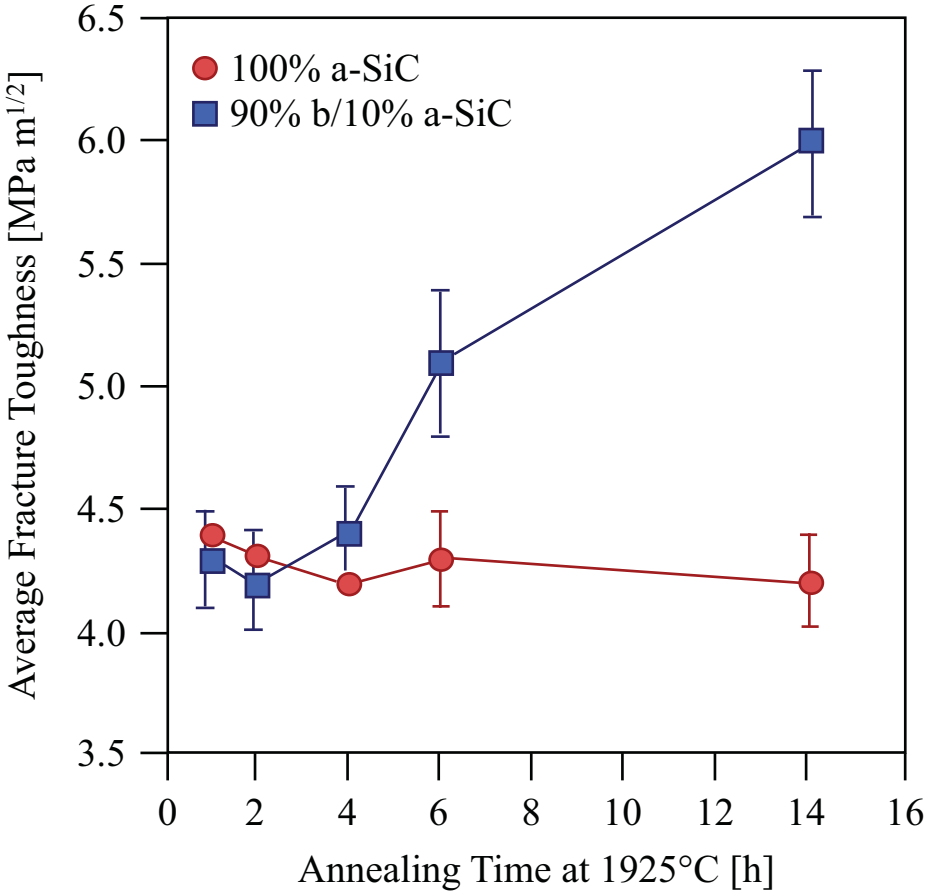

Figure 11: The effect of annealing time on fracture toughness of 100% α-SiC and 90% β/10% α-SiC powders [44]. The solution and precipitation of β-SiC into α-SiC increased the fracture toughness with increasing α-SiC grain growth.

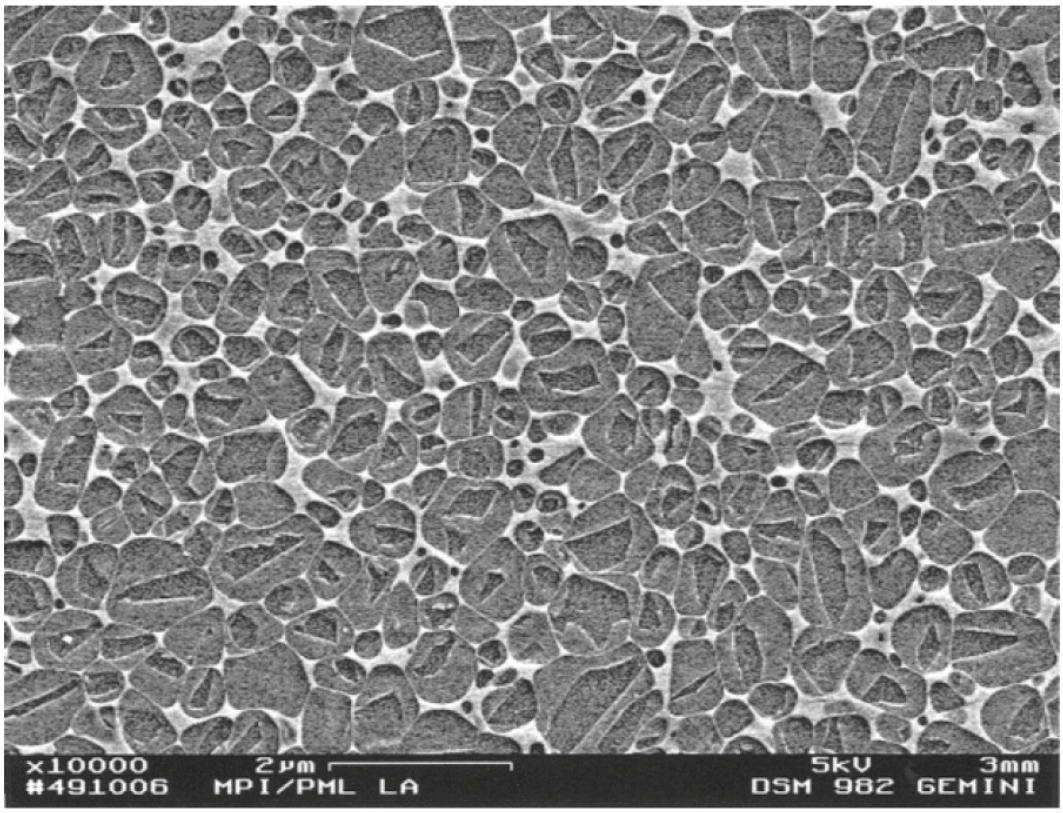

Figure 12: Fine equiaxed microstructure formed from sintering α-SiC powder at 1950°C and heat treating for 16 hours [43].

which leads to micro cracking at the SiC/second phase interface [27].

Flexural strengths between 500–600 MPa were observed in these materials. However, strengths in excess of 1 GPa were achieved through oxidation-induced strengthening, where in which the part was oxidized in air at 1200°C, forming a thin, amorphous SiO_2 layer on the surface of the part, which healed surface flaws and put the part into compression [43], increasing the bending strength of the material. Another reportedly possible way to achieve a flexural bend strength of 1 GPa is through post-HIPing of the compact after sintering [45].

Nader et al. [46] continued Rixecker's work by studying the transformation kinetics of the reaction between β- and α-SiC. It was discovered that the sintering atmosphere had a large effect on the rate of transformation. High pressures of argon increased the reaction rate, while increasing nitrogen pressures retarded the transformation

rate. Their results are also in stark contrast with Mulla's work [40] in that they did not observe any transformation occurring in a pure β-SiC powder mixture during sintering. Therefore it was concluded then that the initial seeding amount of α-SiC was the determining factor in the number of SiC nucleation sites during LPS. The highest fracture toughness values were observed for samples sintered in a 1.5 MPa argon atmosphere and 90% and higher intial β-SiC content. However, pores were still apparent in the sintered material, which were possible nucleation sites for cracking during loading.

2.4 Silicon Carbide Armor Developments

Several armor manufacturers today take advantage of solid-state and liquid phase sintering methods to produce various forms of SiC ballistic armor.

Saint Gobain Ceramics (Niagara Falls, NY) manufactures a line of solid-state sintered silicon carbide under the trade name Hexoloy. The highest product in the line, Hexoloy Enhanced, is claimed to be above 98% theoretical density, exhibits a fracture toughness value (through SENB and double torsion methods) of 4.6 MPa$\sqrt{m}$ and a flexural bend strenth of 428 MPa.

Ceramatec, Inc. (Salt Lake City, UT) has developed methods to exploit LPS phenomena in hot pressing techniques. Cutler et al. describe a method [48] where a mixture of rare earth oxides (Y, La, Ce, Pm, Sm, Eu, Gd, Tb, Dy, Ho, Er, Tm, Yb, Lu, In) (0–19.5%) or a rare earth oxide and alumina mixture (0–19.5%) is used to enhance densification and enable the tailoring of the resulting microstructure to obtain a high toughness part (through exploiting the intergranular fracture mode due to the weak interface). Parts were hot pressed at temperatures between 1700–2200°C (liquid phases formed at temperatures as low as 1600°C). Ultimately, an SiC and Al_2O_3-Y_2O_3 mixture hot pressed at 2000°C was shown to exhibit high hardess (26.4 GPa, the testing method and loading are not specified), high fracture toughness (4.7

MPa$\sqrt{m}$, test method not prescribed), and high bending strengths (535 MPa, 4 point flexural bend test, 20 mm inner and 40 mm outer span, 0.5 mm/min).

Ezis, developed a manufacturing process for hot pressing SiC with a small amount of AlN [49]. Processing in this manner enabled the use of coarser ($d_{50} \sim 3$ μm) sized "dirty" powder (at \$1.50 per pound) as it was inferred that the impurities would collect in the triple points of the microstructure and not harm the structural integrity of the finished part. AlN was added at a rate of 0.25 wt.% per m^2/g of surface area of SiC powder to ensure full coverage and densification enhancement. The resulting material was highly dense (3.04–3.22 g/cm^3) and exhibited an intergranular fracture mode, which led to higher fracture toughness values (4.5 MPa$\sqrt{m}$). Knoop hardness using a 0.5 kgf loading was 2800 kg/mm^2. This material is known as SiC-B, and it and the successor, SiC-N, are manufactured by Cercom, Inc.

CHAPTER III

EXPERIMENTAL PROCEDURE

3.1 Additive Optimization Study

The initial component of this work was to determine the optimized additive amounts needed to effectively sinter silicon carbide to acceptable densities. Prochazka [34] was able to use a minimum of 0.25 wt.% carbon additive, however, the silicon carbide powders were washed with HF to remove the silica before sintering. Therefore, it was necessary to determine an amount of carbon additive that would effectively remove the silica coatings without using HF, while keeping the amount of excess carbon to a minimum.

α-SiC powder with a mean particle size of 0.748 μm was used for this work. The SiC powder was mixed with incremental additions of carbon derived from phenolic resin and with a 0.36 wt.% addition of B_4C. An analysis of the phenolic resin showed that the resin leaves a 44.46% char when pyrolyzed, which was then used to calculate the initial dry resin content that needed to be added to the powder mixture. Poly(methyl methacrylate) (PMMA) was added (2 wt.%) for use as a binder. The compositions were mixed together in acetone and ball milled for 24 hours to ensure even mixing and dispersion. Table 4 shows the compositions of SiC mixed and spray dried for this study.

Spray drying was selected as the granulation method of choice, since it was impossible to dry the slurry quickly enough to eliminate demixing of the phenolic resin. Spray drying eliminates the problem of deflocculation during the drying process. A laboratory spray dryer (BÜCHI Laboratory Equipment, Postfach, Switzerland) was used to spray dry the powders. The dryer was equipped with a two fluid type spray

Table 4: SiC Compositions for Sintering Study

Composition	B_4C Content (wt%)	Carbon Content (wt%)
SS1	0.360	0.250
SS15	0.360	0.375
SS18	0.360	0.500
SS19	0.360	0.625
SS20	0.360	0.750
SS21	0.360	0.875
SS22	0.360	1.000
SS23	0.360	2.000
SS24	0.360	3.000
SS25	0.360	4.000

nozzle. A beaker with a magnetic stirrer was used to keep the particles in suspension during the spraying process. The inlet and outlet temperatures were set to 80°C and 40°C, respectively. Both coarse and fine spray granules were collected from the spray dryer and mixed together. All compositions were sprayed using the same method.

6.41 mm cylindrical pellets were pressed at 13.7 MPa using a laboratory uniaxial press (Model C, Carver, Inc., Wabash, IN). Pellets were then CIPed in a laboratory CIP at 344 MPa. After CIPing, the pellets were placed in an alumina tube furnace and heated at 3°C/min to a 1000°C soak for 2 hr to pyrolyze the phenolic resin.

Sintering was performed in the high temperature dilatometer to obtain dilatometry traces for each composition to determine the sintering behavior. Each sample was run in the dilatometer at a rate of 10°C/min to the sintering temperature. The initial soak temperature for the experiments was set to be 2150°C. The furnace was programmed to hold each sample at the sintering soak temperature until the sample reached its sintering extent (criteria reached where the sintering rate is less than 0.005%/min) or the soak hold reached a total of 90 minutes. Sintered samples were then checked for density through use of the Archimedes method. Rule of mixtures was used to determine the theoretical density of each sample composition. Hexoloy

Table 5: Steps in Grinding/Polishing for the Preparation of Specimens for Hardness Evaluation

Step	Finish	Surface	RPM	Rotation Direction	Time (min)
Grind	120 Grit	Struers MD Piano 120	300	Opposite	30
Grind	220 Grit	Struers MD Piano 220	300	Opposite	30
Grind	45 μm	Buehler Apex B	300	Opposite	30
Grind	15 μm	Buehler Apex B	300	Opposite	60
Polish	9 μm	Buehler Texmet-P	150	Concurrent	60
Polish	3 μm	Struers MD Pan	150	Concurrent	120
Polish	1 μm	Struers MD Dur	150	Concurrent	120

Enhanced, a solid-state sintered silicon carbide product from Saint Gobain (Saint-Gobain Ceramics, Niagara Falls, NY), was used throughout the study as a reference material to compare the samples against.

Samples were mounted in SpeciFix resin (Struers, Inc., Westlake, OH) and polished to a 1 μm finish using plane grinding and polishing equipment and polycrystalline diamond consumables. The complete procedure for grinding and polishing of the samples is listed in Table 5. Polished samples were then subjected to Vickers indentation testing on a Struers Duramin indenter. Ten acceptable indentations were measured and recorded according to the guidelines specified in the ASTM C1327–03 test standard [52]. The indenter calibration was confirmed against a WC-based NIST 2831 standard reference material for Vickers hardness of ceramics and hard metals.

Polished specimens were thermally etched at 1800°C for 1 hr under flowing He in the dilatometer to reveal the microstructural topography of the polished surface. An optical microscope (Olympus BX440, Olympus America Inc., Center Valley, PA) was used to image sample microstructures. A microscope calibration ruler (Carl Zeiss, Oberkochen, Germany) was used to determine length scales for each magnification level.

3.2 Sintering Optimization Studies

Tests were performed to determine the effect of the heating rate on the resulting microstructure. 6.41 mm cylindrical disks of SS23 (2 wt.% carbon) were manufactured as prescribed previously. The specimens were heated in the dilatometer at five heating rates varying from 10 to 50°C/min in flowing He to 2150°C and held until the sintering contraction rate was less than 0.005%/min (completion of sintering). Samples were polished, etched, and analyzed under the optical microscope.

The next step was to determine the sintering soak temperature required to obtain an optimized microstructure that lies within the minimum density threshold needed to facilitate post hot-isostatic pressing (HIPing) to theoretical density. For the study, cylindrical powder compacts of 44.45 mm in diameter were uniaxially pressed, CIPed, and pyrolyzed as described above. The disks were sintered in the dilatometer, heating at 10°C/min to soak temperatures between 2000°C and 2200°C (50°C increments), for 60 min. All samples were post-HIPed using the Verco laboratory-scale HIP (AIP6-30H, American Isostatic Presses, Inc., Columbus, OH) at 1900°C and under 206.8 MPa Ar for 2 h. Sample densities were checked using Archimedes method after sintering and post-HIPing. The disks were mounted, polished, and tested for Vickers hardness. After hardness testing, the samples were etched in thde dilatometer and imaged using the optical microscope.

3.2.1 Mechanical Testing

A total of six ceramic armor compositions, four provided to us by the Army Research Lab, were evaluated in this experiment (Table 6). Verco B_4C, Verco SiC[1], and Hexoloy Enhanced (Saint-Gobain Ceramics, Niagara Falls, NY) were all processed through pressureless sintering (the two Verco materials were subsequently post-hot

[1]Verco SiC refers to the SiC material optimized in the previous additive and sintering optimization work.

Table 6: Armor Compositions Chosen for Mechanical Testing

Sample	Composition
Verco	B_4C
Verco	SiC
Cercom PAD-B_4C	B_4C
Cercom SiC-N FH	SiC
Cercom SiC-N LA3	SiC
Saint Gobain Hexoloy Enhanced	SiC

Table 7: Listing of Mechanical Properties Evaluated

Mechanical Test	ASTM Standard
Flexural Strength	C1161–02c [50]
Fracture Toughness	C1421–01b [51]
Vickers Hardness	C1327–99 [52]
Knoop Hardness	C1326–03 [53]
Elastic Modulus	C1198–01 [54]

isostatically pressed). PAD-B_4C (pressure-assisted densification) and SiC-N (both from BAE Systems, Vista, CA) were densified through hot-pressing. All but the Verco specimens were provided by the Army Research Laboratory (ARL, Aberdeen, MD). Bulk tiles of these materials were sent to be machined into mechanical testing bars (Ferro-Ceramic Grinding, Inc., Wakefield, MA). Bars were machined to match the specifications of the individual tests. For each composition, 12 bars were machined for flexural strength testing and 20 bars were machined and notched for fracture toughness testing. CoorsTek AD-998 Al_2O_3 was purchased to be used for sacrificial parts during machine setup. Because of it's prevalence in armor usage, some of the material properties were reported with the results of the six other compositions.

All mechanical testing measurements were performed in accordance with the ASTM standards. These test standards are listed in Table 7.

3.2.1.1 Flexural Strength

Four-point flexural strength measurements were performed on test bars (Phoenix load frame, Measurements Technology, Inc., Roswell, GA) equipped with a 450 kg load

cell. A fully articulating four-point test fixture (Wyoming Test Fixtures, Inc., Salt Lake City, UT) was used (2 cm inner span and 4 cm outer span, 5 mm diameter rollers) which followed the specifications of the the ASTM C1161–02c standard [50] (NOTE: The CoorsTek AD-998 bars were purchased off the shelf at 3.2 mm × 3.2 mm, which were taken into account when calculating the flexural strength of the material). Twelve rectangular test specimens of 3 mm × 4 mm × 45 mm were evaluated. Displacement of the specimen was measured at the cross head with a precision of 2.54 μm. The loading rate was 0.5 mm/min. The breaking force P was measured, from which the flexural strength S was determined via:

$$S = \frac{3PL}{4bd^2} \tag{19}$$

where L is the outer support span of the fixture, b is the specimen width, and d is the specimen thickness.

3.2.1.2 Fracture Toughness

Ceramic materials are notoriously difficult to pre-crack, therefore chevron-notched beams were machined into bars of dimensions 3 mm × 4 mm × 45 mm to the specifications of the Configuration B size in the ASTM C1421–01b standard. Twenty chevron-notched specimens were machined for each of the five compositions. For fracture toughness measurements, chevron-notched beams were machined into bars of dimensions 3 mm × 4 mm × 45 mm, as part of the Configuration B size specification in the ASTM C1421–01b standard [51]. Twenty chevron-notched specimens were machined (Ferro Ceramic Grinding, Inc., Wakefield, MA) for each of the six compositions. The test apparatus and fixture were the same as those used in the flexural strength tests. The loading rate was 0.3 mm/min. The fracture toughness K_{Ic} was calculated from

$$K_{Ic} = Y^*_{\min} \frac{P_{\max}(S_o - S_i)}{BW^{3/2}} \tag{20}$$

where $P_{\max}$ is the ultimate fracture load for stable crack growth failure, S_o and S_i are the outer and inner spans of the fixture, respectively, B is the sample height, and W is the sample width. $Y^*_{\min}$ is the minimum stress intensity factor and relates to the geometry of the chevron-notched cross section. For the Configuration B chevron-notch cross section profile, the calculated value for $Y^*_{\min}$ is 4.0984.

3.2.1.3 Vickers and Knoop Hardness

Sample pieces of each composition were mounted in epoxy resin and polished to a 1 μm finish using a Struers Rotopol and Pedemat automatic polishing system (Struers, Inc., Westlake, OH). Hardness measurements were obtained on a Struers Duramin hardness tester using a Vickers and Knoop indenter. Both indentation methods were used since either or both measurements are usually reported in literature, and because both scales are incomparable due to the fundamental difference of how each test calculates the stress imparted by the indentation [55]. The instrument calibration was confirmed using the WC-based NIST standard reference material (#2831), National Institute for Standards and Technology, Gaithersburg, MD) for Vickers hardness of ceramics and hard metals.

Vickers indentations were made as prescribed according to the ASTM C1327–03 standard [52]. The applied load of the indent was 9.81 N (1 kgf) for a period of 15 s. The indent locations were selected in a blind and unbiased manner. Ten acceptable indentations, as defined in the standard, were measured and recorded. Knoop indentations were taken according the the ASTM C1326–03 standard [53]. A 19.6 N (2 kgf) load was applied for 15 s. Again, ten acceptable indentations were recorded.

3.2.1.4 Elastic Modulus

The elastic modulus E of the materials were measured using a Sonic Resonance method, as specified in the ASTM C1198–01 standard. The specimens were analyzed in the Dynamic Elastic Properties Analyzer (Matrix Enterprises, Waterville, OH). In this test setup, mechanical excitation was applied to the sample through a transducer on one end, and a second transducer on the other end sensed the fundamental vibration frequency f_f^2 of the material, and used this value to determine E by:

$$E = 0.9465 \frac{m f_f^2 L^3 T_1}{b t^3} \tag{21}$$

where m, b, L, t are the mass, width, length, and thickness of the bar, respectively. T_1 is a correction factor to account for Poisson's ratio and other mechanical parameters. Poisson's ratio values for B_4C and SiC were taken from reported values in literature [8, 17].

3.2.2 Characterization

The density of each material was measured using the Archimedes method. Samples were boiled for 1 hour, and 3 measurements were taken for dry, suspended, and saturated weights and averaged. The samples were measured at room temperature.

Phases were identified through x-ray diffraction (X'Pert PRO Alpha-1 diffractometer, PANalytical, Almelo, The Netherlands). Each sample was scanned fifteen times over a 12 h period. The scans were merged into a single intensity graph to obtain high peak to noise ratio patterns. The B_4C specimens were placed in an etching solution consisting of 1 g of KOH in 100 mL of deionized water. A thin leaf of Pt was used as the cathode. Using 21 VDC and 0.3 A, the specimens were etched for a period of 30-60 s to make the grain boundaries evident. Polished SiC specimens were thermally etched at 1500°C for 30 min in a flowing Ar atmosphere.

The etched microstructures were characterized using an optical microscope (Olympus BX440, Olympus Corporation, Tokyo, Japan) and a scanning electron microscope (SEM, Model 1530, LEO Electron Microscopy, Inc., Oberkochen, Germany). Energy-dispersive X-ray spectroscopy (EDS, Oxford Pentafet detector with ultrathin window, Oxford Instruments, Oxfordshire, UK) was used to characterize the elements present in each specimen. Average grain sizes and grain size distributions were calculated using the line-intercept method (500-700 measurements per micrograph) on optical micrographs of etched polished surfaces.

3.3 Ballistic Evaluation of SiC Armor

Following the sintering optimization studies, production of large scale samples began in order to supply parts for ballistic evaluation. A spray dryer (Model PSD 180, Anhydro Holdings A/S, Copenhagen, Denmark) was rented for a month to be able to granulate enough powder to press the quantity of tiles needed. The spray dryer was outfitted with a two-fluid nozzle capable of drying 7 kg/hr of water at 350°C.

A 38–40 solids wt.% aqueous suspension was developed for the spray drying process. α-SiC (Grade HSC490N, Superior Graphite, Chicago, IL) powder was batched with a mixture of 1.5 wt.% polyvinyl alcohol (PVA), 1 wt.% polyethylene glycol (PEG), 0.6 wt.% Darvan 821A (R. T. Vanderbilt Company, Norwalk, Connecticut), 0.36 wt.% sinter-grade B_4C (Grade HS, H.C. Starck, Newton, MA), and 2.5 wt.% of a water-soluble Novalok-type phenolic resin (SP-6877, SI Group, Schenectady, NY) was used. The suspension was spray dried (inlet temperatures between 190–220°C, outlet under 100°C, two-fluid nozzle set to 51.7 kPa) and sieved through a 145 μm mesh to remove agglomerates.

4" $\times$ 4" tiles were pressed in a 200-ton double-action press (CeramTec NA, Laurens, SC) with a 4.690" square die size. After pressing, the tiles were CIPed in the Verco CIP at 344 MPa to eliminate any possible pressing gradients. The tiles were

then placed in a high temperature vacuum furnace (Model 822-SN, Thermal Technology, LLC, Santa Rosa, CA) for thermolysis of the organic binders and pyrolysis of the phenolic resin (0.5°C/min to 500°C and held for 20 hr, and 3°C/min to 1000°C and held for 8 hr). Samples were sintered in the System VII furnace (Centorr Vacuum Industries, Nashua, NH).

Sintered tiles were HIPed (Bodycote North America, Princeton, KY) at 1900°C for 1 hr under 206.8 MPa Ar. 15 acceptable tiles from each of the two sizes requested for ballistic evaluation (0.262", 0.680") were selected for shipment. Ballistic evaluation was performed by Foster-Miller, Inc. The tiles were bonded to composite backing coupons, and the ceramic/composite samples were shot with a 7.62mm x 54R LPS (mild steel core) Ball Round. Four other SiC compositions from competitive manufacturers were supplied to be tested in the same manner.

CHAPTER IV

RESULTS

4.1 Additive Optimization Study

To evaluate the sintering effectiveness of each sample composition, the theoretical density of each sample was calculated using the rule of mixtures according to the initial B_4C and phenolic resin loading amounts. These densities are listed in Table 8. Post-sintering densities of all compositions (SS1–SS25) run in the dilatometer are listed in Table 9.

The resulting dilatometry traces for SS1-SS21 compositions are shown in Figure 13. None of the samples in this testing group (0.250–0.875 wt.% carbon) reached the criteria for full sintering extent during the 90 minute soak at 2150°C. As expected, sample SS1 did not sinter well in this experiment. One thing to note, however, is that Prochazka leached the silica coatings off his starting powders, which could have led to the decreased need for high carbon addition. Nevertheless, the compositions generally sinter better as the carbon content is increased.

Table 8: Calculated Theoretical Density of SS1–SS25 Compositions

Composition	Theoretical Density (g/cm^3)
SS1	3.2045
SS15	3.2028
SS18	3.2012
SS19	3.1996
SS20	3.1979
SS21	3.1963
SS22	3.1947
SS23	3.1820
SS24	3.1696
SS25	3.1575

Table 9: Post Sintering Density of SS1–SS25 Compositions

Composition	Sintered Density (% Theoretical)
SS1	53.11
SS15	53.84
SS18	56.16
SS19	55.81
SS20	57.76
SS21	63.28
SS22	73.33
SS23	95.68
SS24	97.34
SS25	97.37

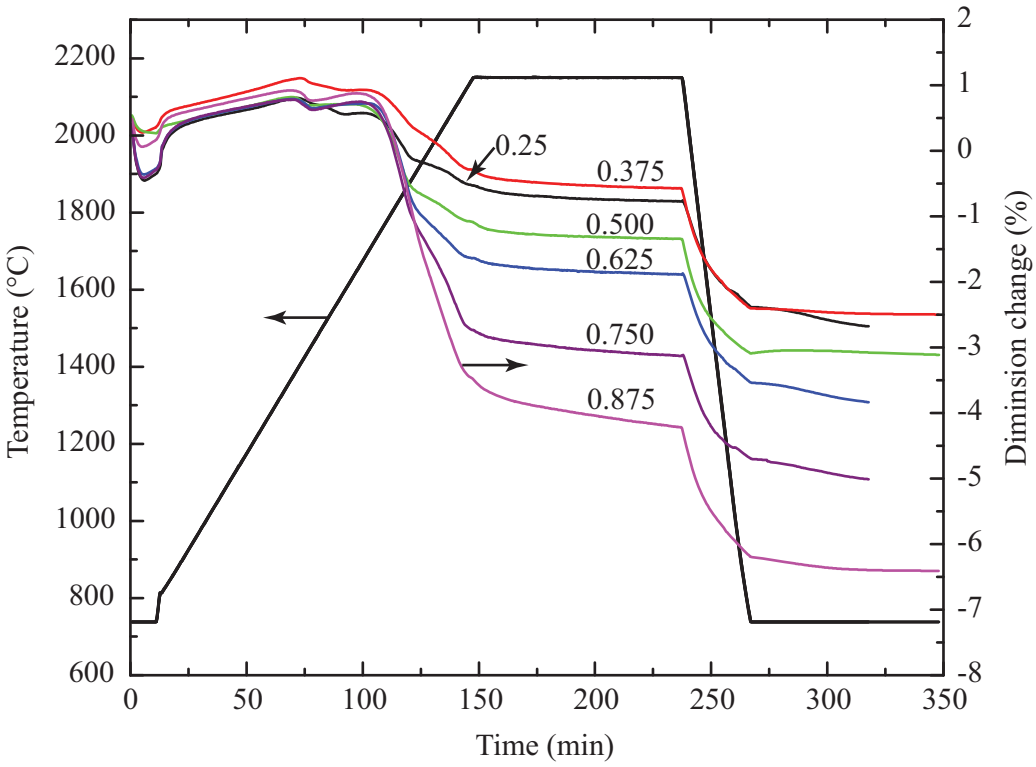

Figure 13: Dilatometry traces for samples SS1-SS21. Sinterability increases as carbon content is increased, however, the extent is far less than desired.

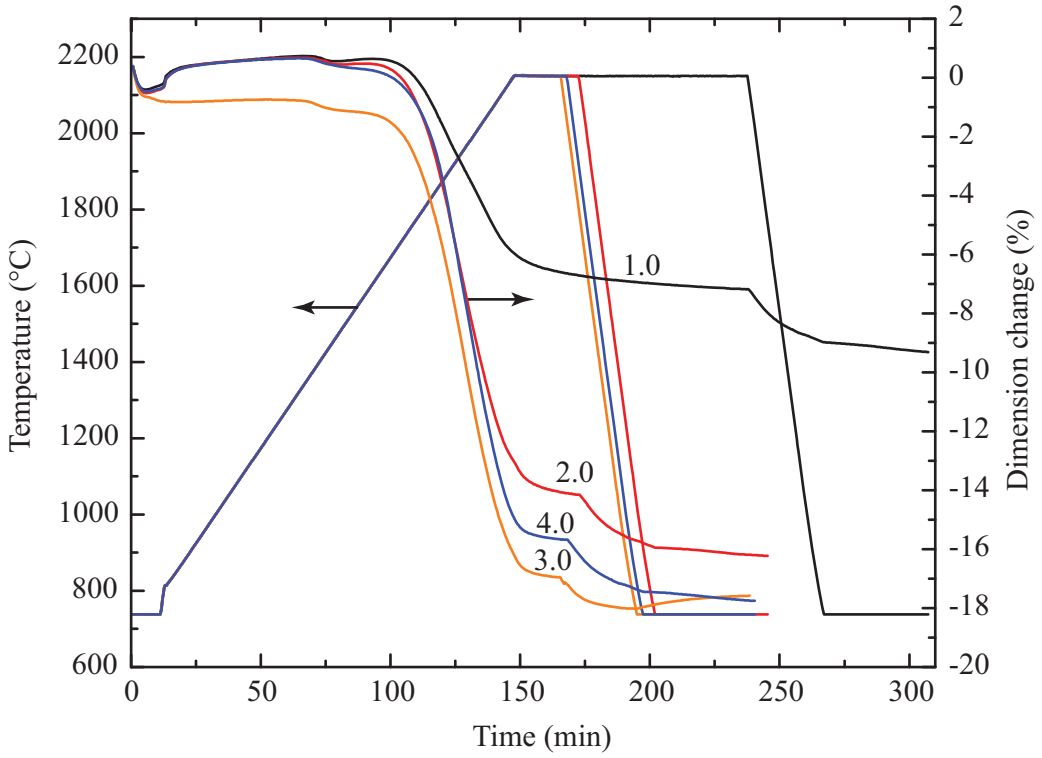

Figure 14: Dilatometry traces for samples SS22–SS25, of which SS23 and SS24 show the highest relative densities of the sintering group. The SS25 sintering extent is greater than that of SS23; however, the sintered density is lower.

Due to the low sinterability of these compositions, the carbon contents were increased to 1–4 wt.% additions. The dilatometry traces for the SS22–SS25 samples are shown in Figure 14. A large increase in sinterability of these compositions in respect to the first group is plainly evident. All samples above SS22 (1 wt.% carbon) sintered to densities higher than 93% theoretical. It is evident that at least 2 wt.% carbon is needed for reaching a greater than 90% theoretical density threshold. The SS23 sample sintered to a terminal density of 95.68% theoretical. Sinterability increased minimally with the SS24 and SS25 samples (97.34 and 97.37% theoretical, respectively). Therefore, it was determined that 2 wt.% carbon would be the optimal amount for further work.

Between 1450–1500°C, there is a sharp downward inflection point in the dilatometry traces for all the samples, irregardless of carbon content amount. This is believed

Table 10: Vickers Hardness Values For SS23–SS25 Samples and Hexoloy Enhanced

Composition	Vickers hardness (HV)
SS23	2329.10 ± 134.72
SS24	2423.30 ± 120.81
SS25	2393.10 ± 87.96
Hexoloy Enhanced	2308.10 ± 87.96

to be where the carbon begins to reacts with the silica coating. Between 1500°C and 1700°C, the sample exhibits no expansion or contraction. The onset for sintering occurs between 1650–1700°C. Samples lower than 1 wt.% carbon show irregular shrinkage behavior (as seen in the humps in the traces of the SS1–SS21 samples). Samples above 1 wt.% carbon (SS22–SS25) exhibit much smoother sintering contraction traces once sintering has past onset.

Vickers hardness and density values for the SS23–SS25 samples and Hexoloy Enhanced are shown in Figure 15 and listed in Table 10. The manufacturer's claimed value for the theoretical density of Hexoloy Enhanced is greater than 98%. In our own density measurements, the density of Hexoloy Enhanced is 3.154 g/cm^3, which is 98.21% relative to the theoretical value of SiC (3.211 g/cm^3). While not having as high a theoretical density as Hexoloy Enhanced, the Vickers hardness values are superior. An increase in hardness is seen between sample SS23 and SS24, which is due to the increase in theoretical density. However, with increasing carbon content, the Vickers hardness values begin to fall. It is clearly evident that excess carbon additive is deleterious to the mechanical properties of the material.

XRD patterns were taken for the SS23–SS25 samples and are shown in Figure 16. All three samples exhibit the same phase and intensity factor for all SiC peaks. A tighter and longer scan around the most intense graphite peak, 26.611°2θ was performed and the results are shown in Figure 17. The intensity of each sample was normalized by taking the intensity ratio between the highest graphite peak and the highest SiC peak (at 34.845°2θ, the (101) plane). The amount of residual graphite

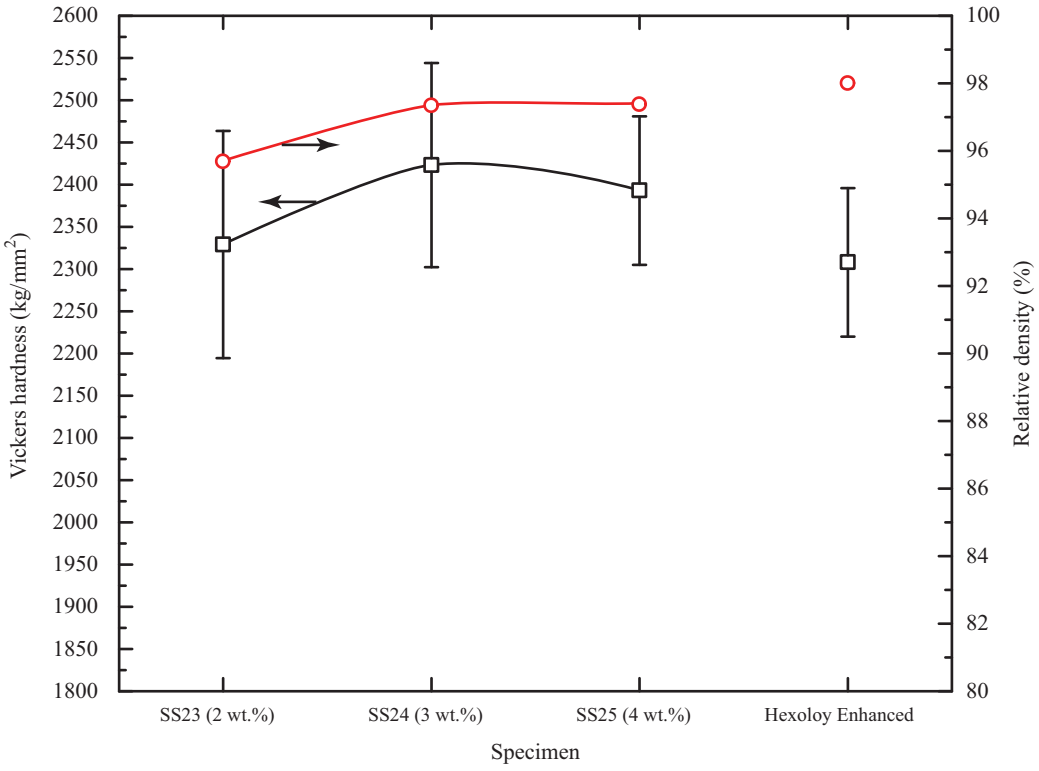

Figure 15: Vickers hardness values of SS23–SS25 and Hexoloy Enhanced. Unoptimized, as-sintered specimens demonstrated higher hardnesses than Hexoloy Enhanced. Note that Saint Gobain does not publish an exact relative density for Hexoloy Enhanced, but reports a value greater than 98% in their literature.

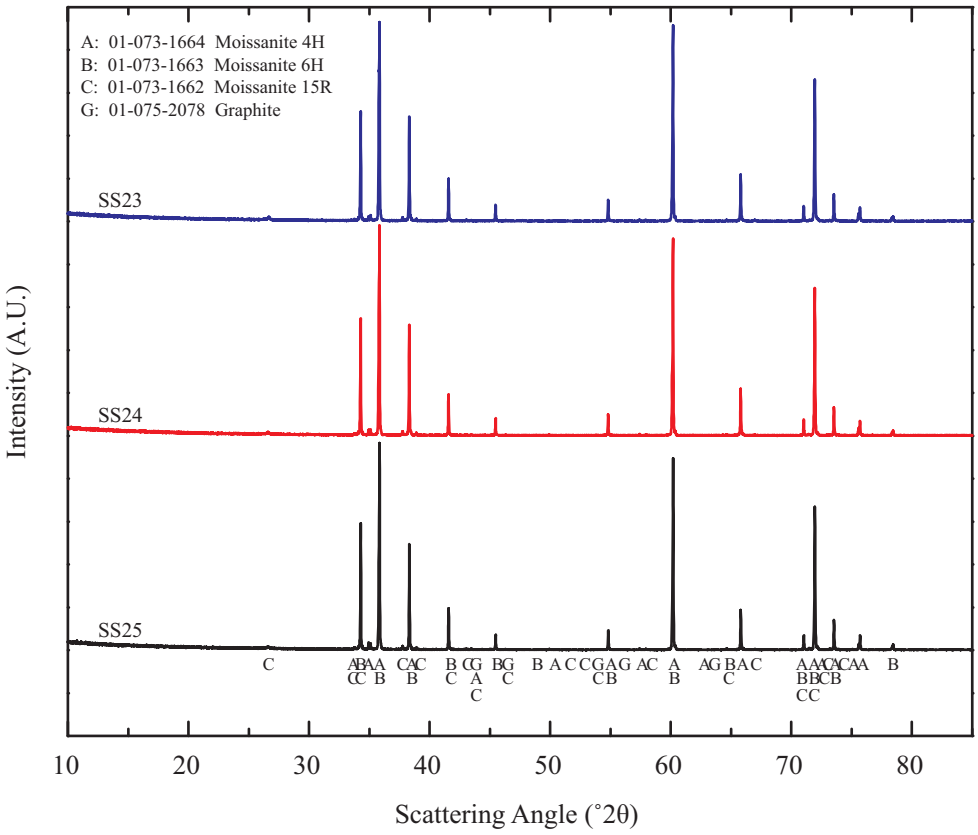

Figure 16: X-ray diffraction traces of specimens with 2, 3, and 4 wt.% carbon additions. ICDD data: A: 01-073-1664 Moissanite 4H; B: 01-073-1663 Moissanite 6H; C: 01-073-1662 Moissanite 15R; G: 01-075-2078 Graphite.

in each SS sample follows the trend of additive amount. Hexoloy has a much higher residual graphite peak than the other four samples, which seems to indicate that the carbon content of Hexoloy before sintering is at least or greater than 5 wt.%.

A collage of optical images of each sample microstructure, taken at 20× magnification, is shown in Figure 18. Hexoloy Enhanced is clearly much coarser than the SS samples, which implies that either the starting powder is much coarser than the Superior Graphite powder used for this study, or that the sintering was done at a higher temperature, which facilitated abnormal grain growth. The grain size distribution for the samples are shown in Figure 19. All the SS compositions show a nearly uniform grain size distribution. Hexoloy exhibits a much coarser and wider grain size distribution than all SS samples. Table 11 lists the average grain size for all samples.

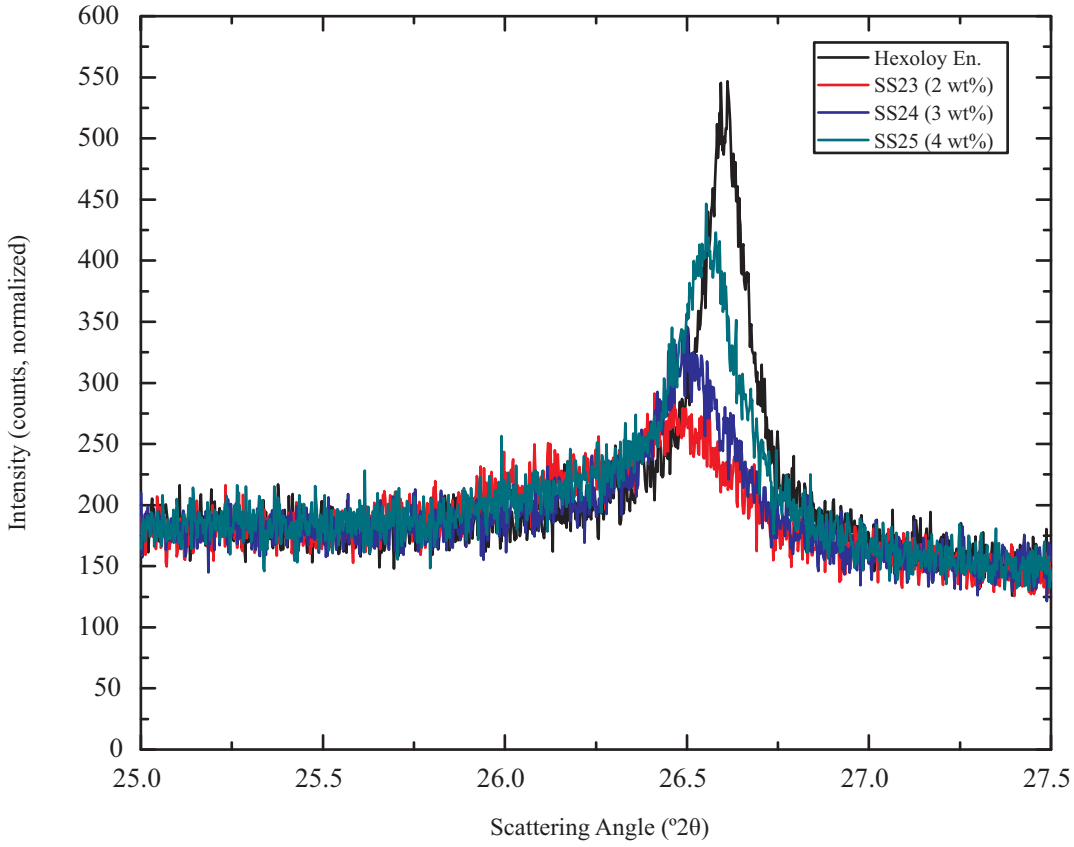

Figure 17: X-ray diffraction traces concentrated in the region of the most intense graphite peak.

Table 11: Average Grain Size for SS and Hexoloy Samples

Composition	d_{50} (μm)
SS23	2.5269
SS24	2.7328
SS25	2.4054
Hexoloy	4.8372

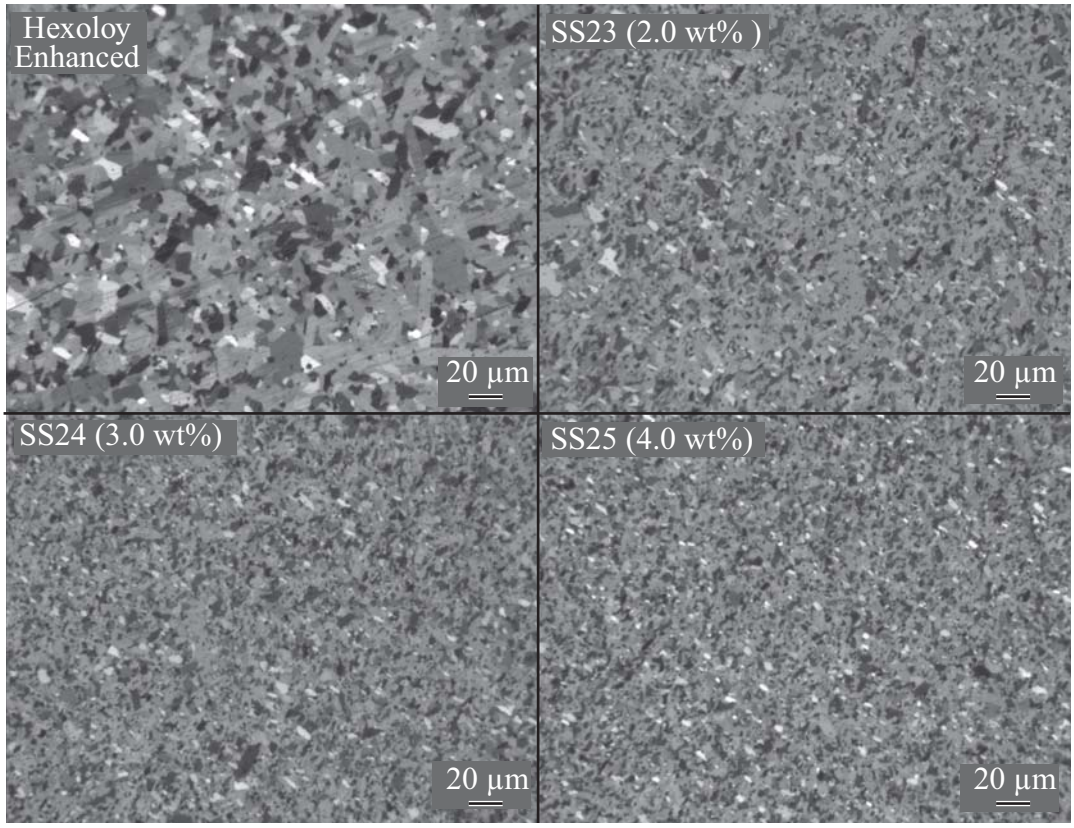

Figure 18: Optical micrographs (20×) of polished and thermally-etched specimens with the indicated carbon weight percentages and the Hexoloy specimen. Hexoloy exhibits a much coarser and high aspect grain microstructure, indicating abnormal grain growth.

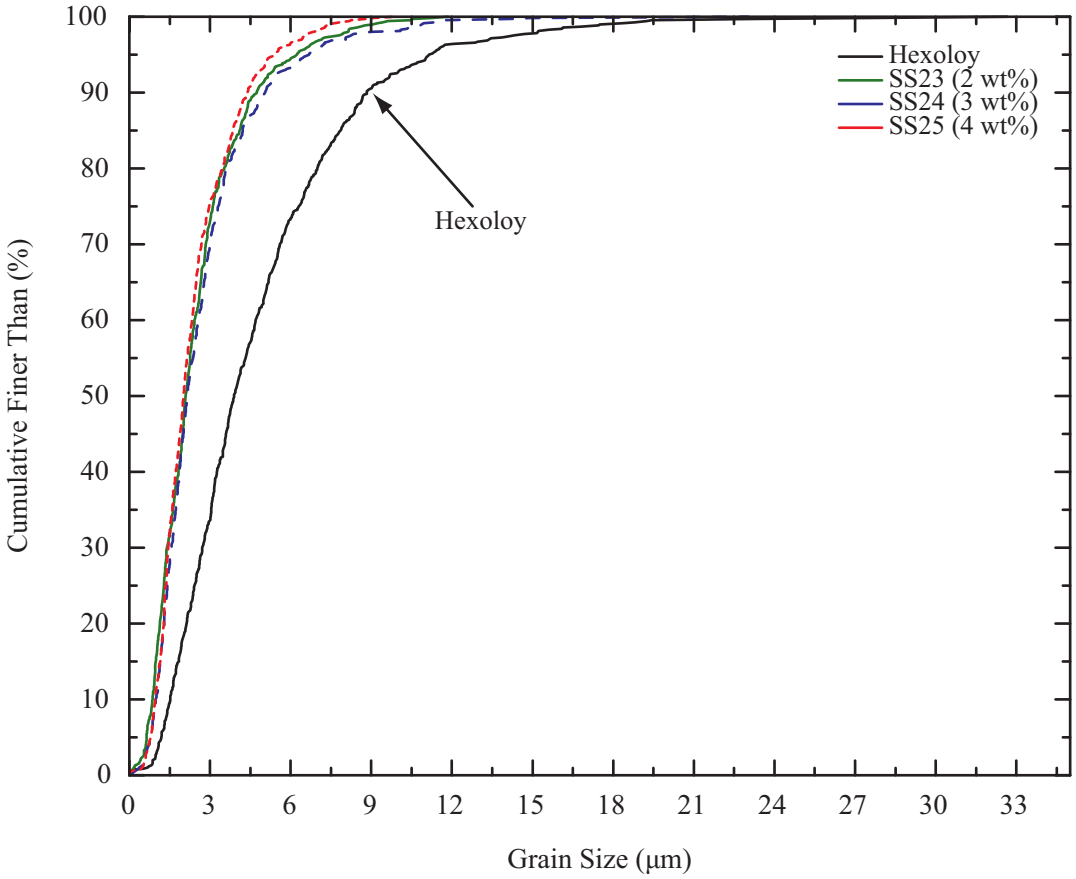

Figure 19: Grain size distributions of the specimens with varying carbon content along with the Hexoloy specimen, as determined by the linear intercept method. Samples SS23–SS25 exhibit similar distributions.

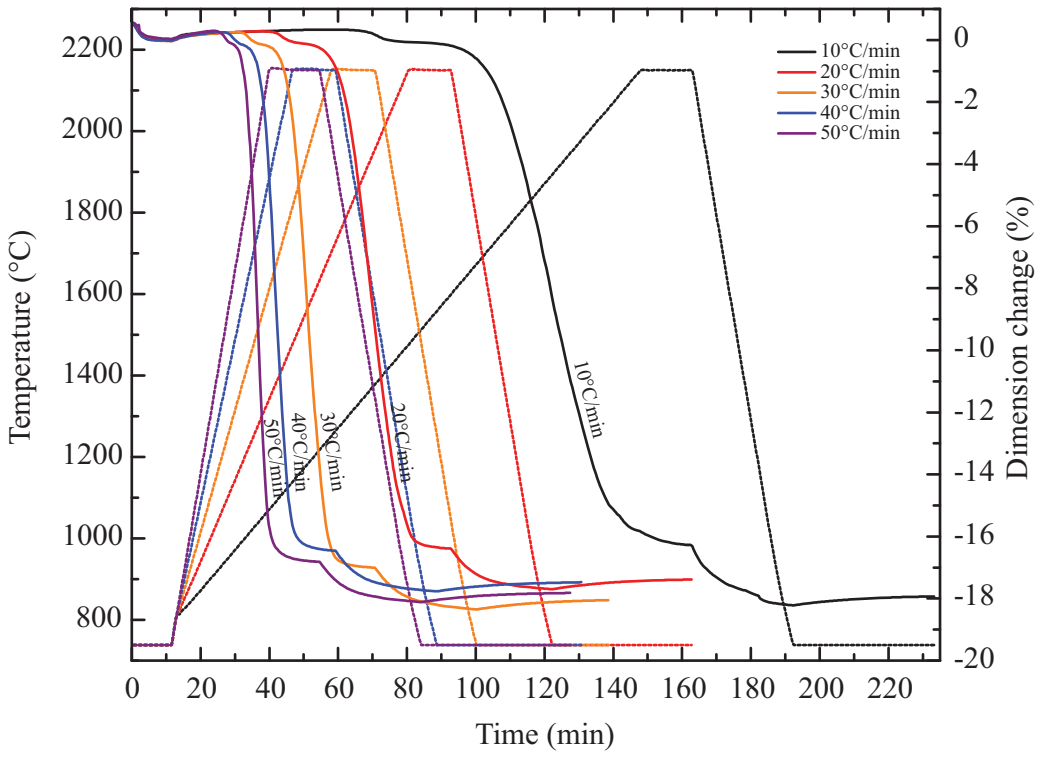

Figure 20: Dilatometry traces for powder compacts exposed to differing heating rates.

4.2 Sintering Optimization Study

The dilatometry traces for the SS23 samples sintered under different heating rates is shown in Figure 20. As seen, there is not a large difference in the time of sintering extent for most samples sintered faster than the 10°C/min heating rate, and the sintering shrinkage is relatively similar between all samples. However, upon inspection of the resulting microstructures (Figures 21 and 22), it can be clearly seen that a rapid heating rate results in large amounts of exaggerated grain growth. This result was not intuitive, as it was shown in previous boron carbide work [2] that slower heating rates resulted in excessive coarsening, and as a result, lower sintered density. However, the result is promising, since the slower heating rates make large-scale manufacturing more feasible.

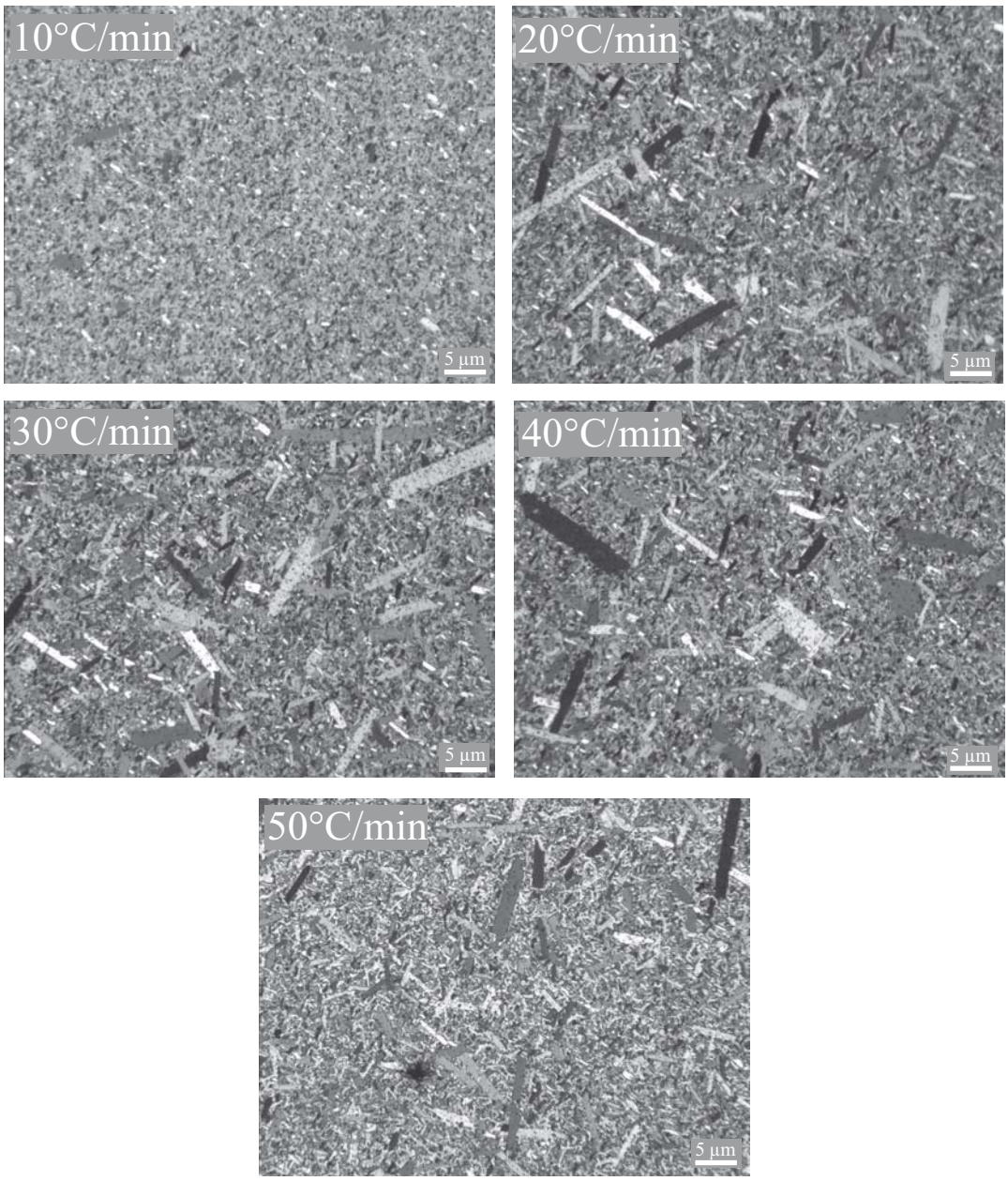

Figure 21: SS23 samples sintered at various heating rates. The sample sintered with the 10°C/min heating rate exhibits the finest grain structure.

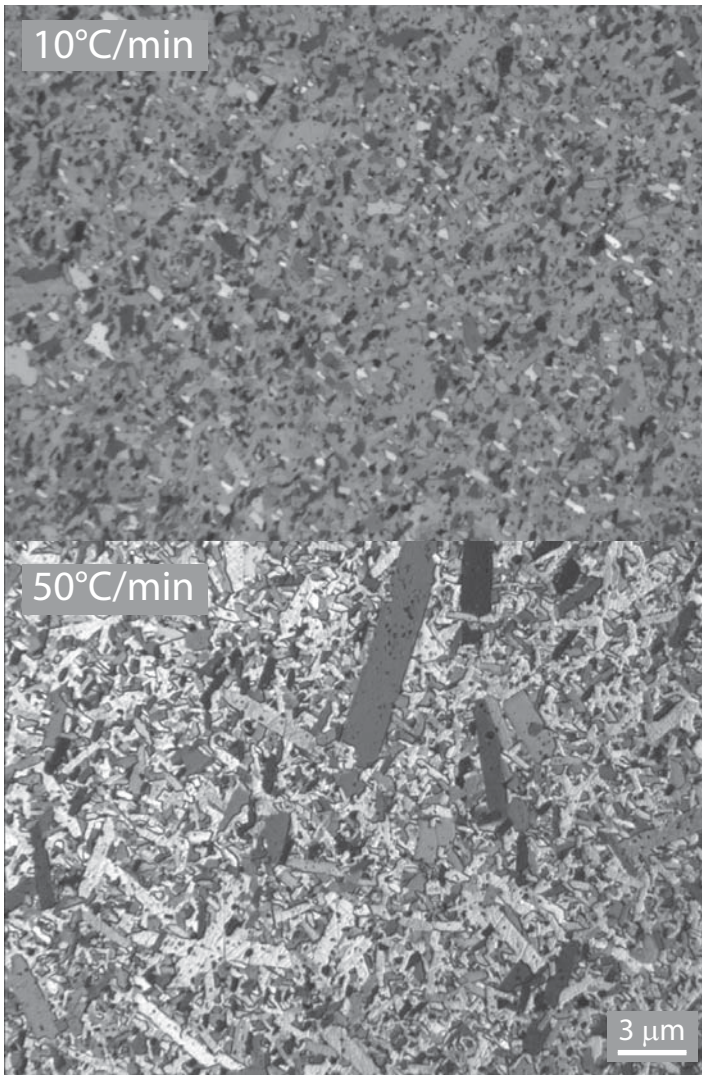

Figure 22: SS23 samples sintered at 10 and 50°C/min, imaged at 50×.

For the temperature and post-HIPing study, larger cylindrical disks 44.45 mm in diameter were used. However, during testing it was discovered that the parts did not sinter well. It was found that for these size parts, the PMMA binder did not working adequately and that powder granules were not being crushed under the action of the press, therefore a switch to a PVA-PEG binder/plasticizer system was necessary. However, the resin is not soluble in water, and the organics are not soluble in acetone. A Novalok-type phenolic resin was obtained that was water-soluble and left a high amount of carbon char, 48.01%, after pyrolysis. Also, for this powder, a different laboratory spray dryer was used, which was equipped with a new type ultrasonic nozzle (Sono-Tek Corporation, Milton, NY). The ultrasonic nozzle utilizes piezoelectric transducers to create a fine, low velocity atomized spray. The spray granules produced (Figure 23) are much more uniform and have a much tighter size distrubution that granules attained through using a two-fluid or rotary atomizing nozzle. Several batches of SiC suspensions were made with varying amounts of resin content, and sintered to 2150°C. The dilatometry traces, shown in Figure 24, show that the 2.5 wt.% carbon additive sintered the greatest and exhibited the lowest time for sintering extent. All further studies in this work are using this spray dried powder formulation.

The density results and Vickers hardness results of the sintered and post-HIPed disks are listed in Table 12 and shown in Figure 25. As shown, all samples above 2050°C, which were sintered to over 96% theoretical density, are essentially theoretically dense after post-HIPing at 1900°C. The 2000°C sample, which was thought to have a high enough threshold density (from previous boron carbide work [2]), did not HIP well. Therefore, for SiC, it can be inferred that open porosity exists under 96%, therefore parts need to be sintered above this value to obtain a fully "encapsulated" part.

Vickers hardness values are the highest for the sample sintered at 2050°C. The

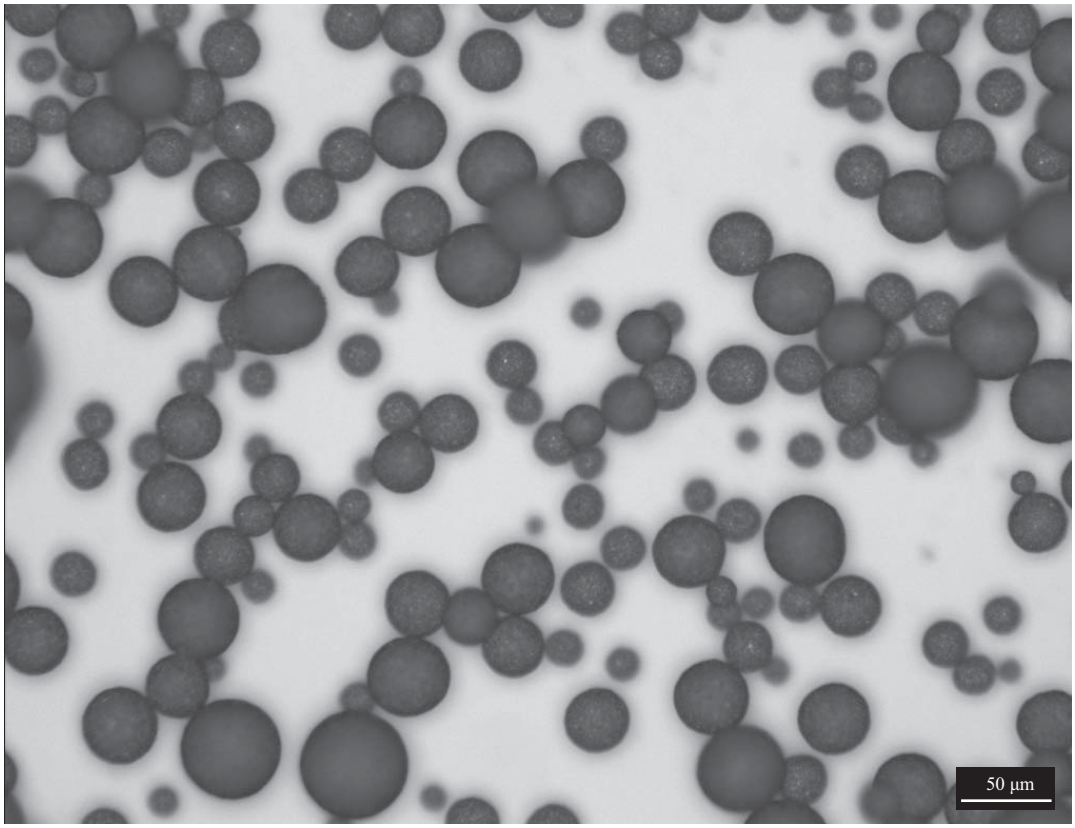

Figure 23: Spray-dried granules attained through use of a ultrasonic atomizing nozzle from Sono-Tek Corporation.

Table 12: Sintering and Post-HIPing Data for 44.45 mm Samples

Sintering Temperature °C	Sintered Density % Rel.	HIP Density % Rel.	Vickers Hardness (post-HIP) kg/mm^2
2000	93.29	95.76	2036.30 ± 174.65
2050	96.85	99.87	2600.70 ± 31.90
2100	98.01	99.93	2595.20 ± 46.33
2150	98.40	99.75	2550.70 ± 68.37
2200	97.67	99.60	2537.50 ± 55.45

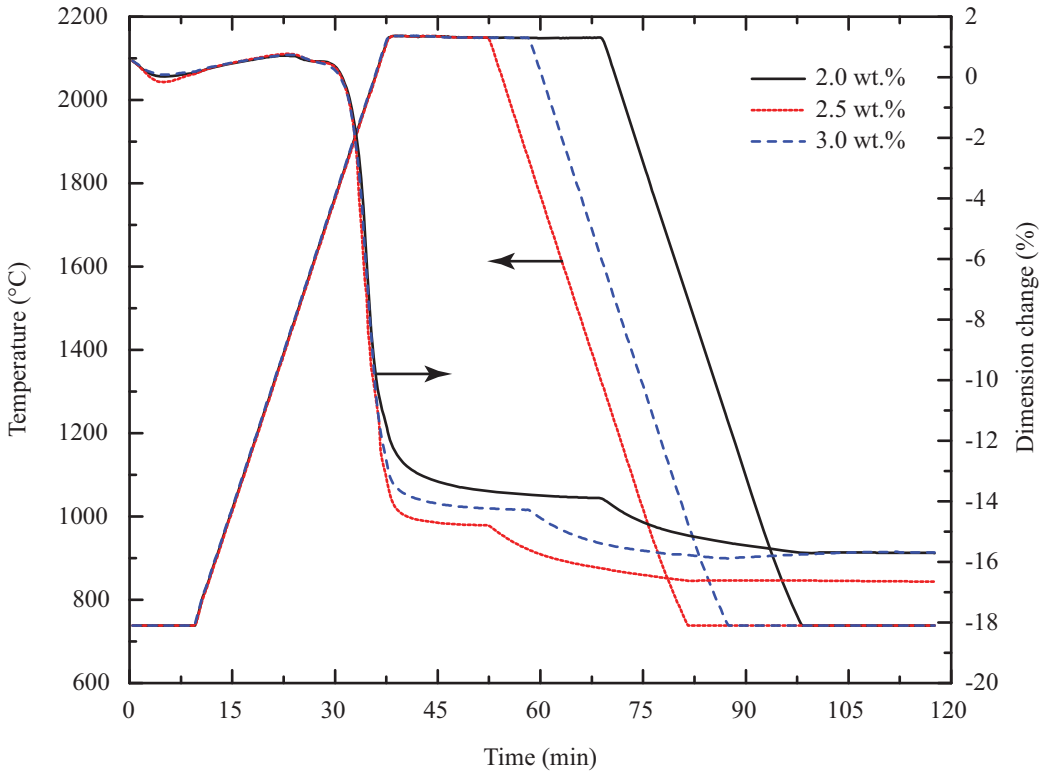

Figure 24: Dilatometry traces for the initial Anhydro spray-drying trials. Numbers in the figure correspond to weight percentages of added phenolic resin. The sample with the 2.5 wt.% carbon content sintered the best.

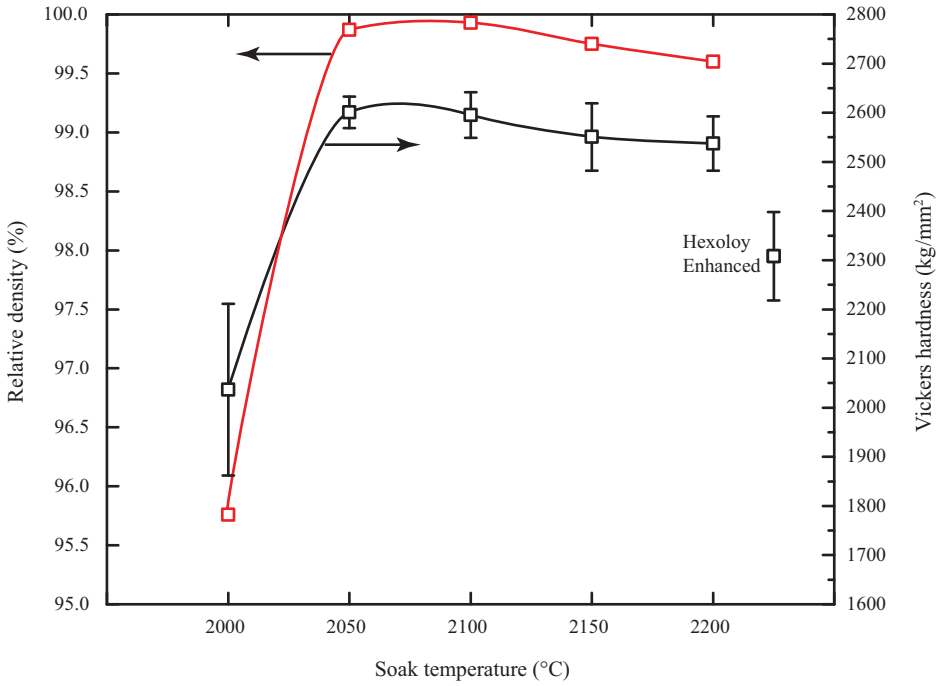

Figure 25: Hardness and relative density values for specimens which were sintered and post-HIPed as a function of sintering soak temperature. Hexoloy Enhanced hardness value is added as a reference.

reason is readily evident in the images of each sample microstructure, shown in Figure 26. 2050°C exhibits the finest grain structure of all the samples post-HIPed to theoretical density. Above 2100°C, the samples undergo abnormal grain growth. Porosity is evident in the interior of the large platelets, which might account for the decrease in post-HIPed density values in the 2150–2200°C samples. A Vickers indentation in the post-HIPed specimen which was sintered at 2100°C is shown in Figure 27. Transgranular fracture is clearly evident, indicating strong cross-grain boundary bonding and lack of a weak interfacial grain boundary phase. EDS scanning using the LEO 1550 SEM reveal that the dark blemishes in the microstructure of the 2050°C sample are pockets of graphite, and not pores, as initially thought. These results are shown in Figure 28. The transgranular nature of the ceramic and the EDS data suggest that the grain boundaries are clean of any secondary phases.

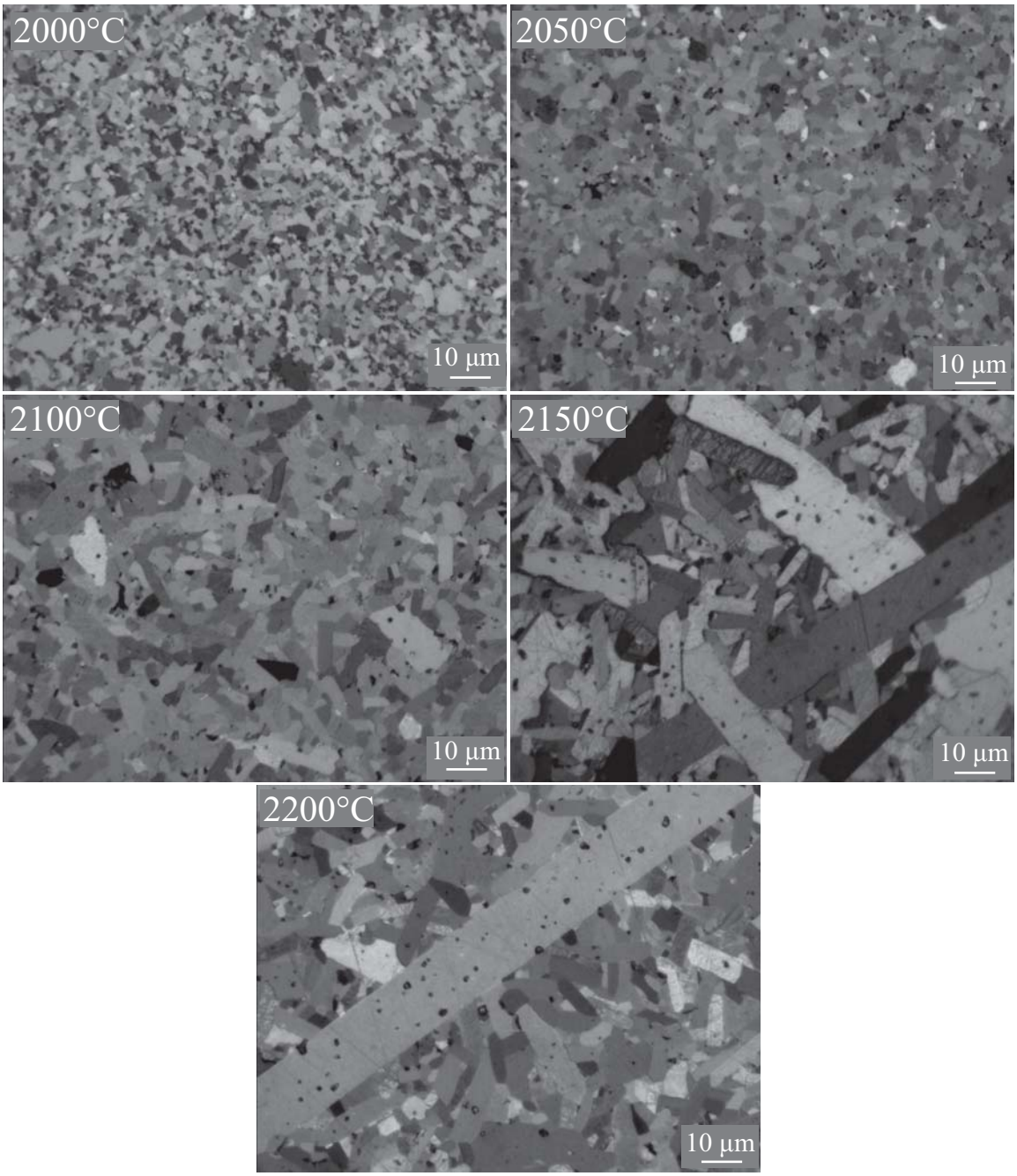

Figure 26: Etched microstructures of sintered and post-HIPed specimens which were sintered at the indicated soak temperatures. Abnormal grain growth is evident in samples soaked above 2100°C, which leads to the decrease in Vickers hardness for those samples.

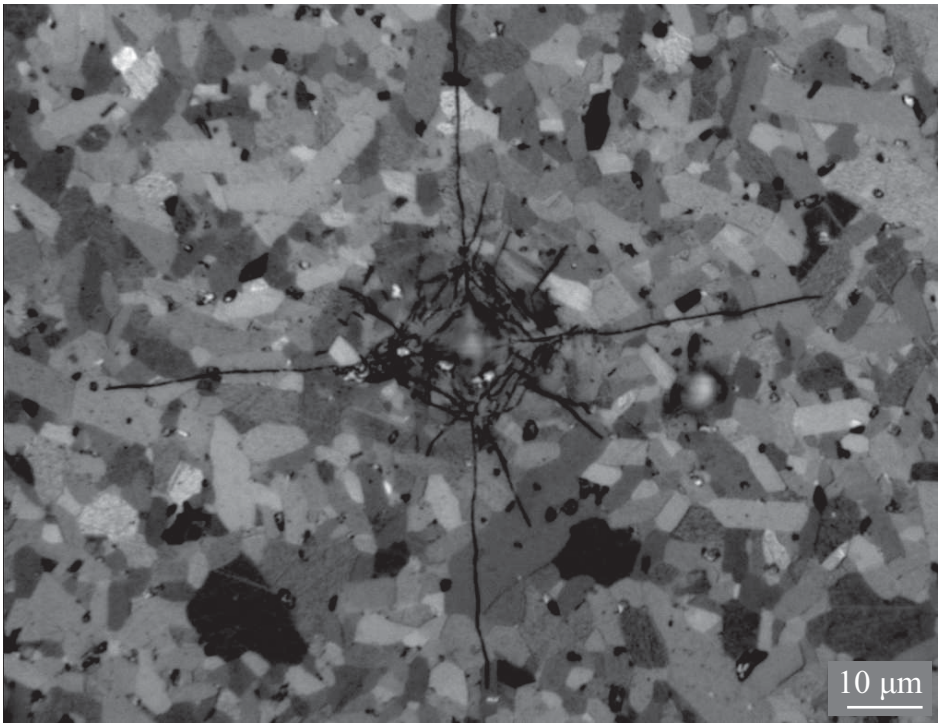

Figure 27: A Vickers indentation in the post-HIPed specimen which was sintered at 2100°C. Transgranular fracture behavior is exhibited.

4.3 Mechanical Characterization

X-ray diffraction (XRD) patterns for the B_4C samples are shown in Figure 29. Verco B_4C exhibits B_4C phases with a residual amount of free graphite. PAD-B_4C scans revealed trace free graphite, as well as trace amounts of alumina, a common densification aid for hot-pressed B_4C [8, 59].

XRD patterns for SiC-N materials are shown in Figure 30. Both SiC-N materials were composed of α-SiC grains, only differing minutely in the polytypes exhibited. The presence of densification aids as second phases was not detected, most likely due to the relatively minute amount of additive and the high probability that the additive peaks could be hidden underneath the SiC peaks.

Hexoloy Enhanced and Verco SiC XRD patterns are shown in Figure 31. Both were composed of minutely different α-SiC polytypes. Traces of graphite were evident, which was expected, since most sintered SiC materials include carbon [15, 34, 60],

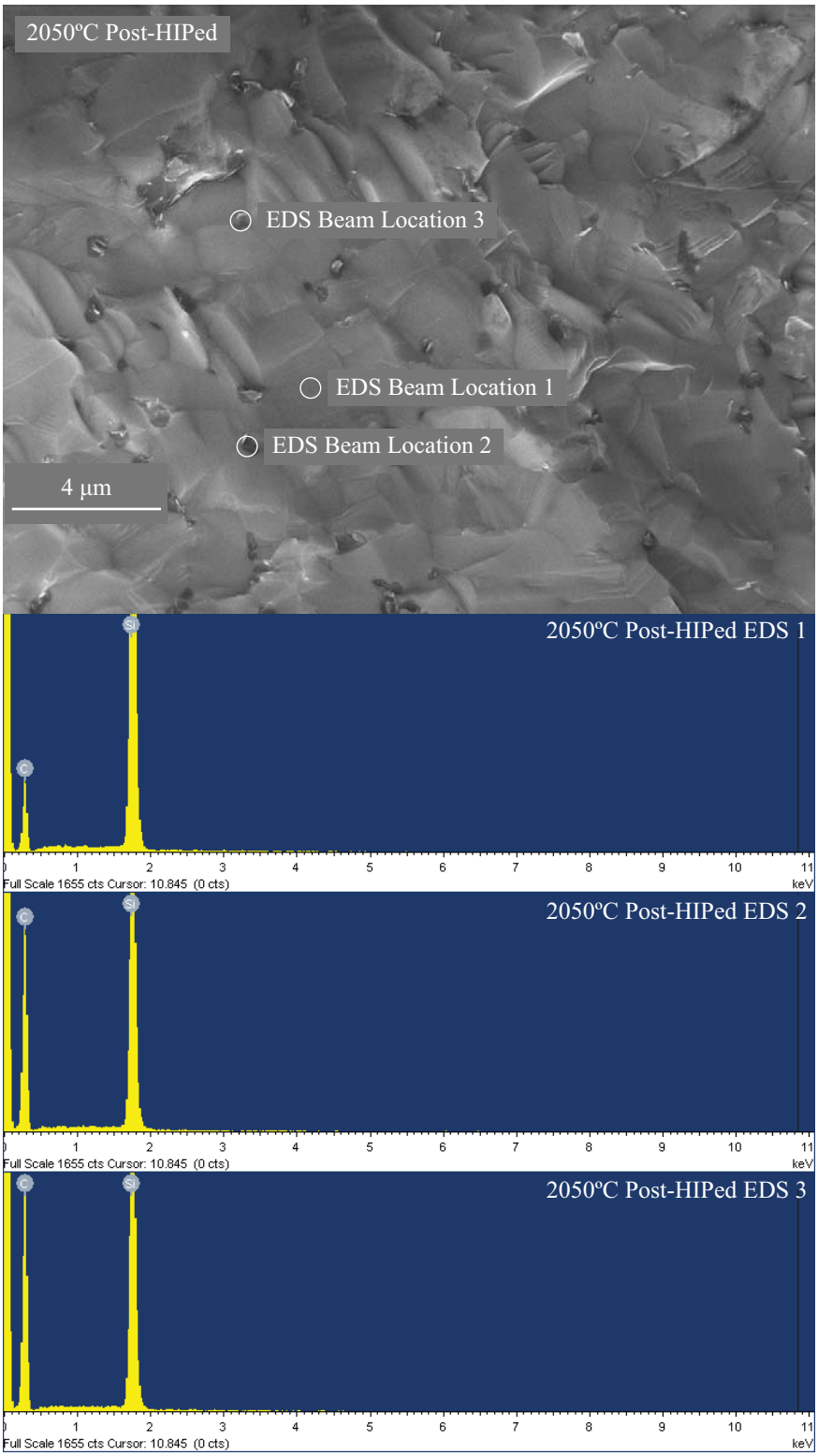

Figure 28: EDS scans of the 2050°C sample after post-HIPing. Blemishes in the triple points are revealed to be pockets of carbon. No excess carbon could be found along the grain boundaries.

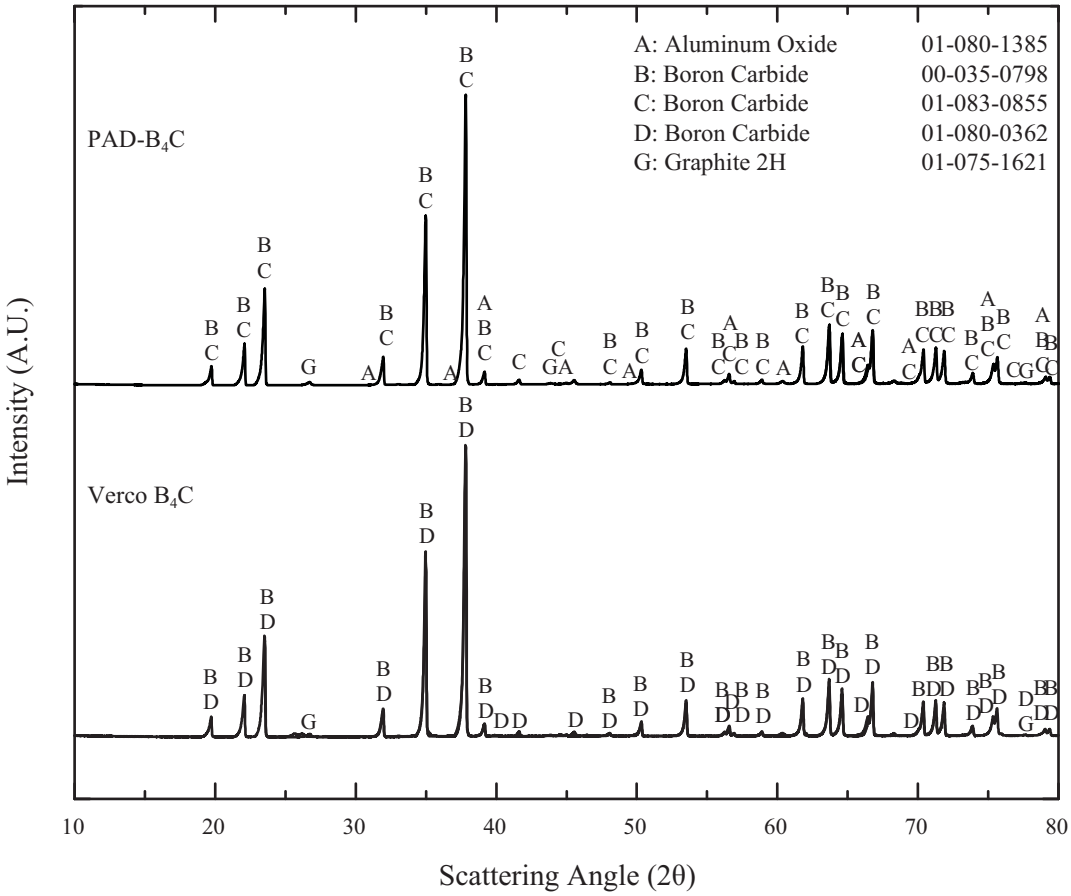

Figure 29: XRD patterns for Verco B_4C and PAD-B_4C. Trace amounts of alumina are present in the PAD-B_4C.

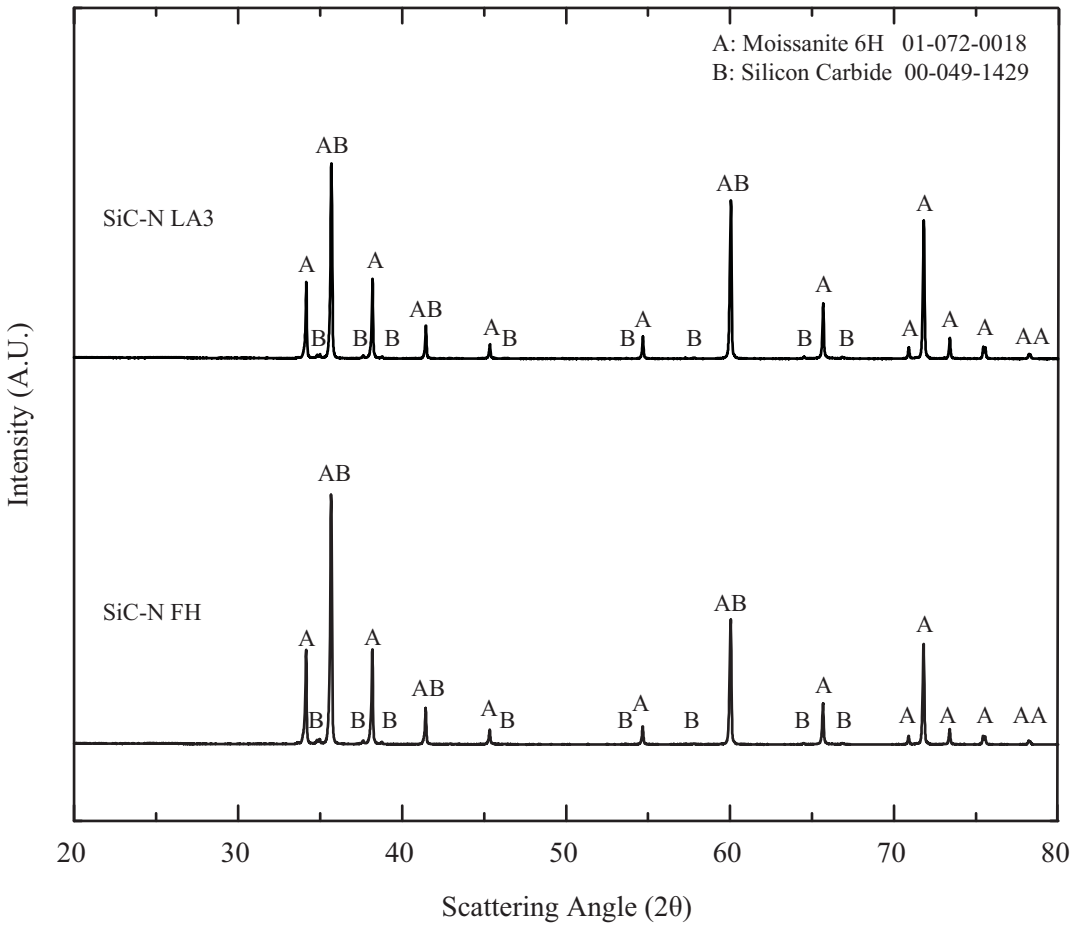

Figure 30: XRD patters for SiC-N FH and LA3

however, no boron or boron carbide was observable in the scan.

Elemental scans using EDS confirm the XRD scans for Verco and PAD-B_4C samples. Verco B_4C exhibited no other elements besides boron and carbon. The scans in PAD-B_4C reveal that aluminum exists in inclusions situated randomly throughout the microstructure, as shown in Figure 32. The EDS scans of SiC-N samples detected aluminum and oxygen situated at the grain boundaries, inferring that an aluminosilicate glass exists throughout the microstructure. This result is shown in Figure 33. Scans of Hexoloy Enhanced detected inclusions at the triple points rich in boron. No phases were detected at the boundaries in the Verco SiC and Hexoloy Enhanced samples, as reported similarly in TEM work performed on solid-state SiC [61]. This

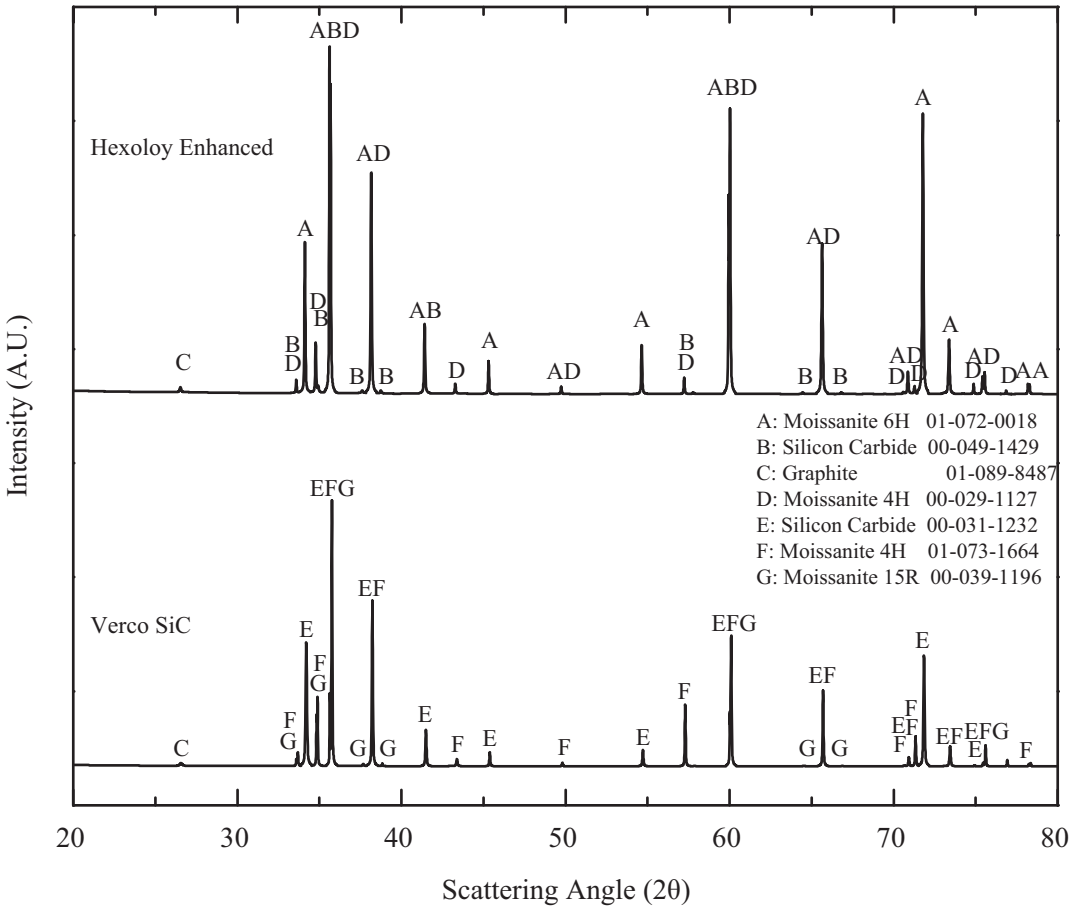

Figure 31: XRD patterns for Hexoloy Enhanced and Verco SiC

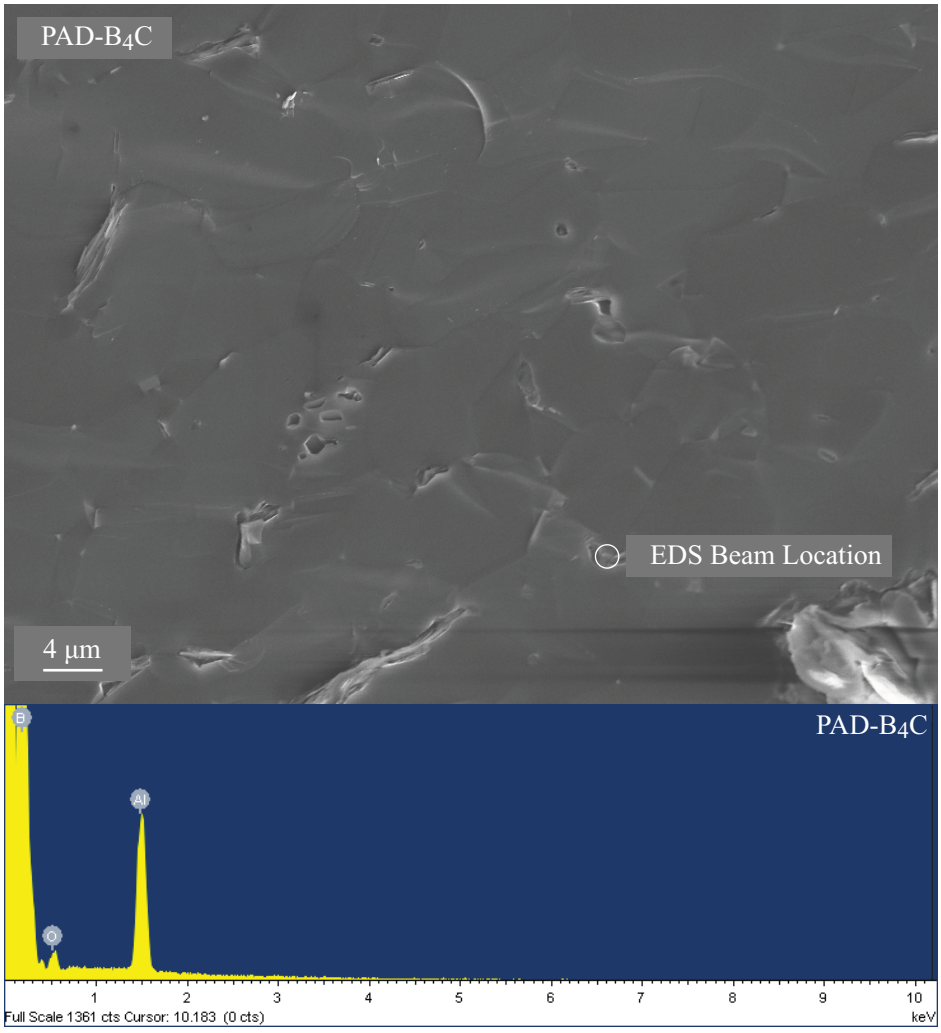

Figure 32: EDS scan of PAD-B_4C showing aluminum existing in inclusions at the grain corners.

explains the disparity in fracture toughness values between hot-pressed and and sintered SiC materials. The intergranular phases in SiC-N lead to enhanced fracture toughness through crack deflection and bridging. Hexoloy Enhanced, and Verco SiC, have higher hardness values due to their clean boundaries exhibiting high strength interfacial bonding.

Fracture surfaces of all samples were imaged in the LEO SEM and are shown in Figure 34. The only material to exhibit intergranular fracture is SiC-N, as the fracture surface is clearly showing a faceted, grain-like appearance. Intergranularity

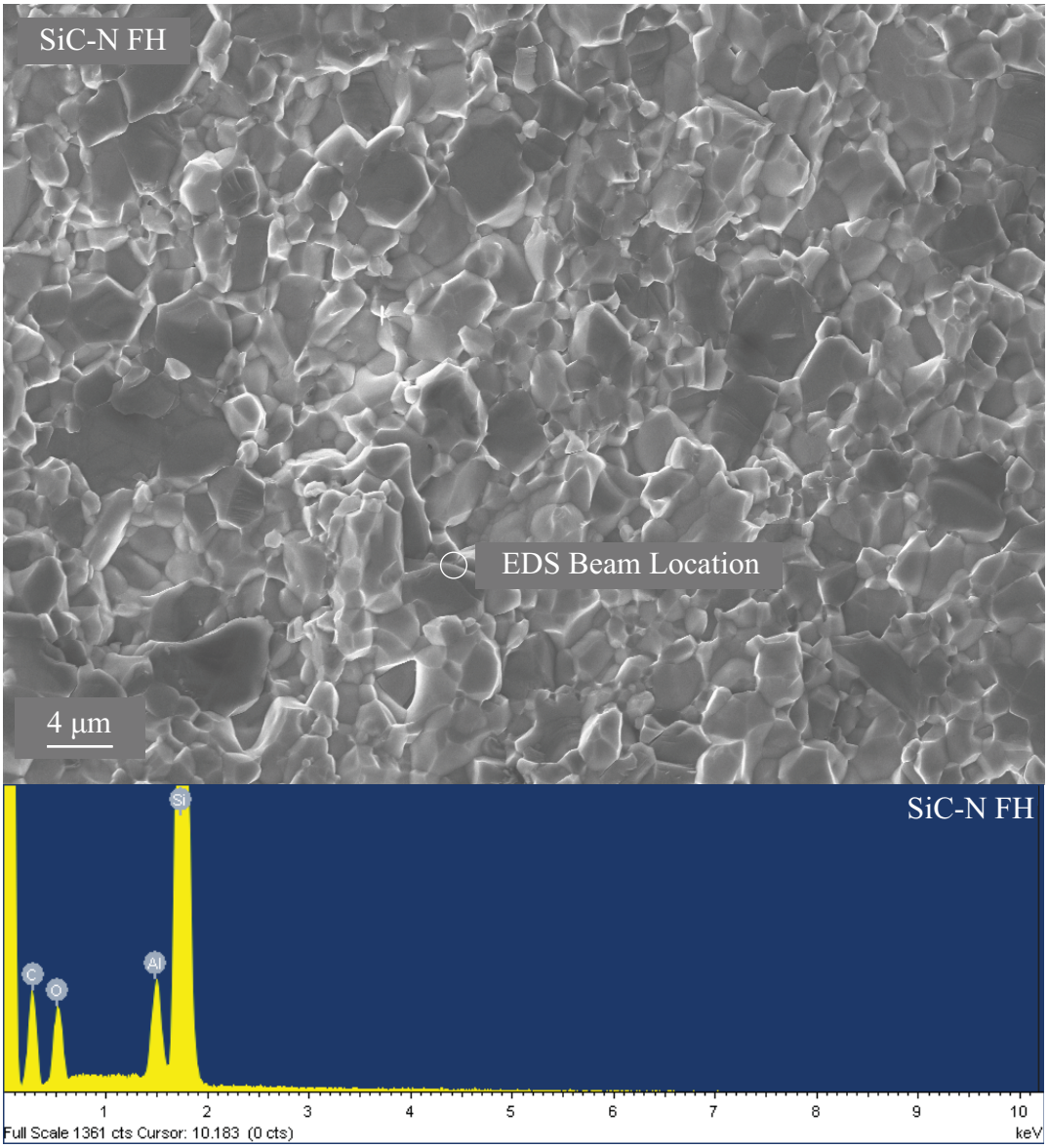

Figure 33: EDS scan of SiC-N fracture surface. The grain facets on the fracture surface are coated with the interfacial phase containing aluminum and oxygen.

Table 13: Mean Values for Carbon Inclusions in Sintered SiC Materials

Sample	Mean (μm)	Median (μm)
Verco SiC	0.219	0.192
SiC Hexoloy Enhanced	1.699	1.691

is also seen in the cracking pattern on the fracture surface, as shown in Figure 35. This reinforces the assumption that the the higher fracture toughness values are a direct result of the intergranular phase. All other materials shown a transgranular fracture pattern, which was inferred from the fracture toughness measurements of B_4C and sintered SiC samples, and through Vickers indentation cracking patterns. Both Verco materials clearly show a smoother fracture surface than that of the respective PAD-B_4C and Hexoloy samples, believed to be a result of the difference in grain size. The carbon inclusions for both Verco SiC and Hexoloy Enhanced were measured using the line-incercept method and the mean and median values are listed in Table 13. Verco SiC exhibits a highly fine distribution of carbon, much more so than Hexoloy Enhanced.

All polished samples were imaged using the optical microscope, and are shown in Figure 36. The grain size distributions for all samples are shown in Figure 37. Mean and median values are listed in Table 14. Verco B_4C has a finer grain size distribution compared to PAD-B_4C, which is a contributing factor to the disparity between their hardness values. No porosity is evident in the Verco B_4C sample. Both SiC-N and Verco SiC microstructures are fine and equiaxed. The SiC-N specimens show grains mutually separated by a continuous grain boundary phase (much more pronounced in the LA3 sample). Hexoloy Enhanced has a broader and coarser distribution compared to Verco SiC. A correlation between fine grain size distributions leading to higher indentation hardness values is evident for most samples. However, the hardness to grain size does not correlate between Hexoloy Enhanced and SiC-N, likely due to the weak intergranular phase present in SiC-N. The Hexoloy sample exhibits grains

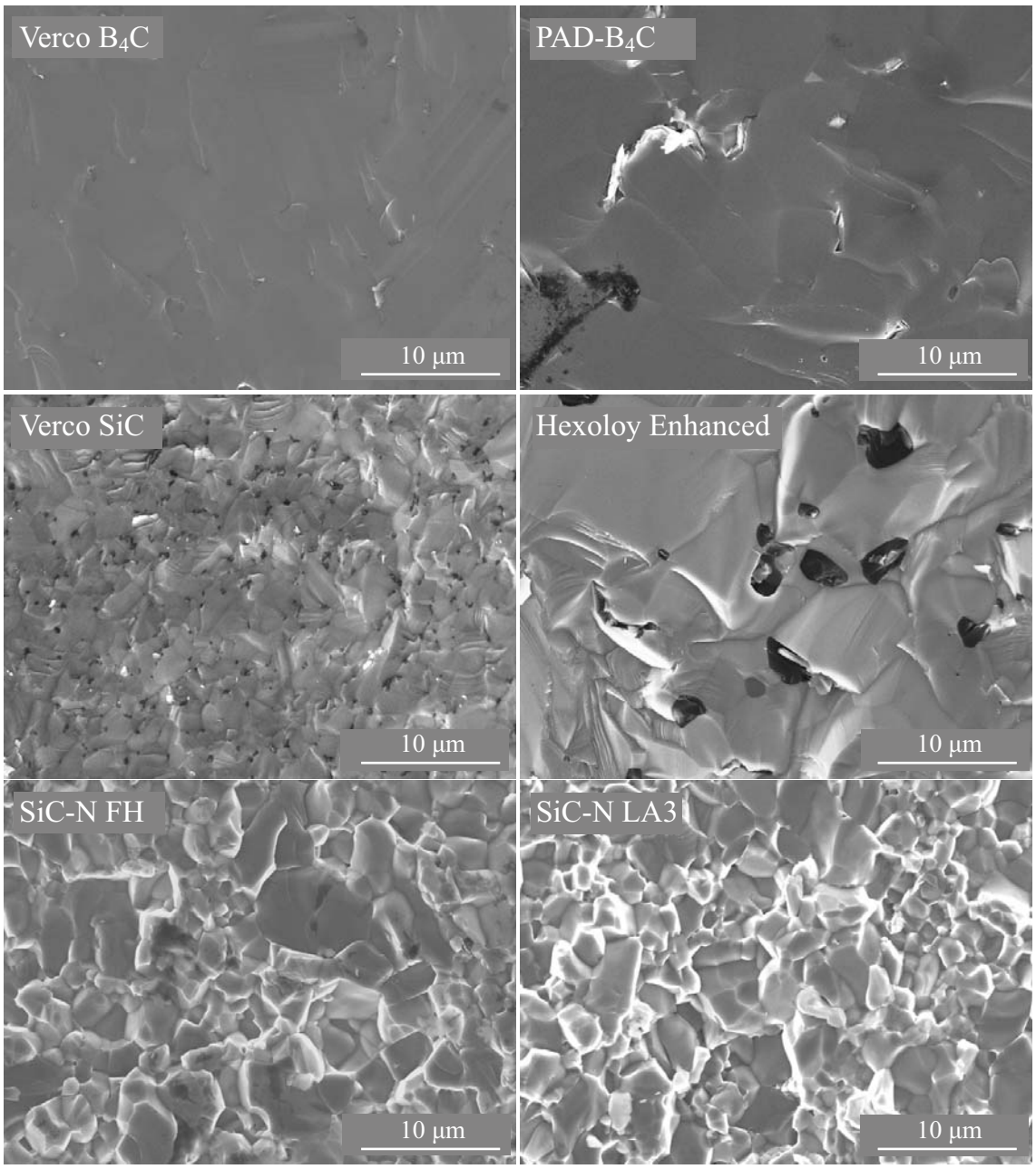

Figure 34: Fracture surfaces of all ceramics as imaged by the LEO SEM. The scale bar is 10 μm. SiC-N is the only material to show an intergranular fracture mode.

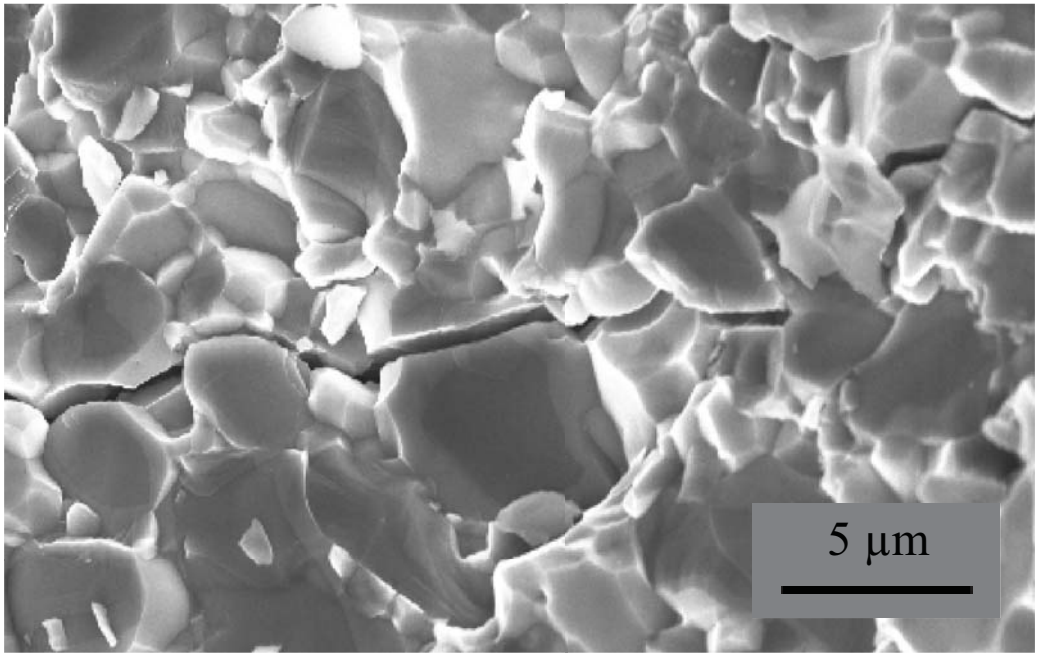

Figure 35: Crack propagating intergranularly on the fracture surface of SiC-N.

Table 14: Mean Values for Grain Size of All Armor Ceramics

Sample	Mean (μm)	Median (μm)
Verco B_4C	2.6623	2.2935
Verco SiC	2.5259	2.1033
PAD-B_4C	5.2012	4.5200
Cercom SiC-N FH	2.5793	2.2522
Cercom SiC-N LA3	2.3765	1.9656
SiC Hexoloy Enhanced	4.8372	3.8994

with high aspect ratio and porosity trapped within grains, which suggest abnormal grain growth due to high sintering temperatures [46, 56]. No high aspect grains are exhibited in Verco SiC.

Table 15 summarizes all mechanical testing results for the 6 compositions tested in this work.

The results of the flexural strength bend test for all materials is shown in Figure 38. All SiC ceramics perform better in this test over the B_4C samples. The two SiC-N varieties exhibit extraordinarily high flexural bend strengths, similar to those

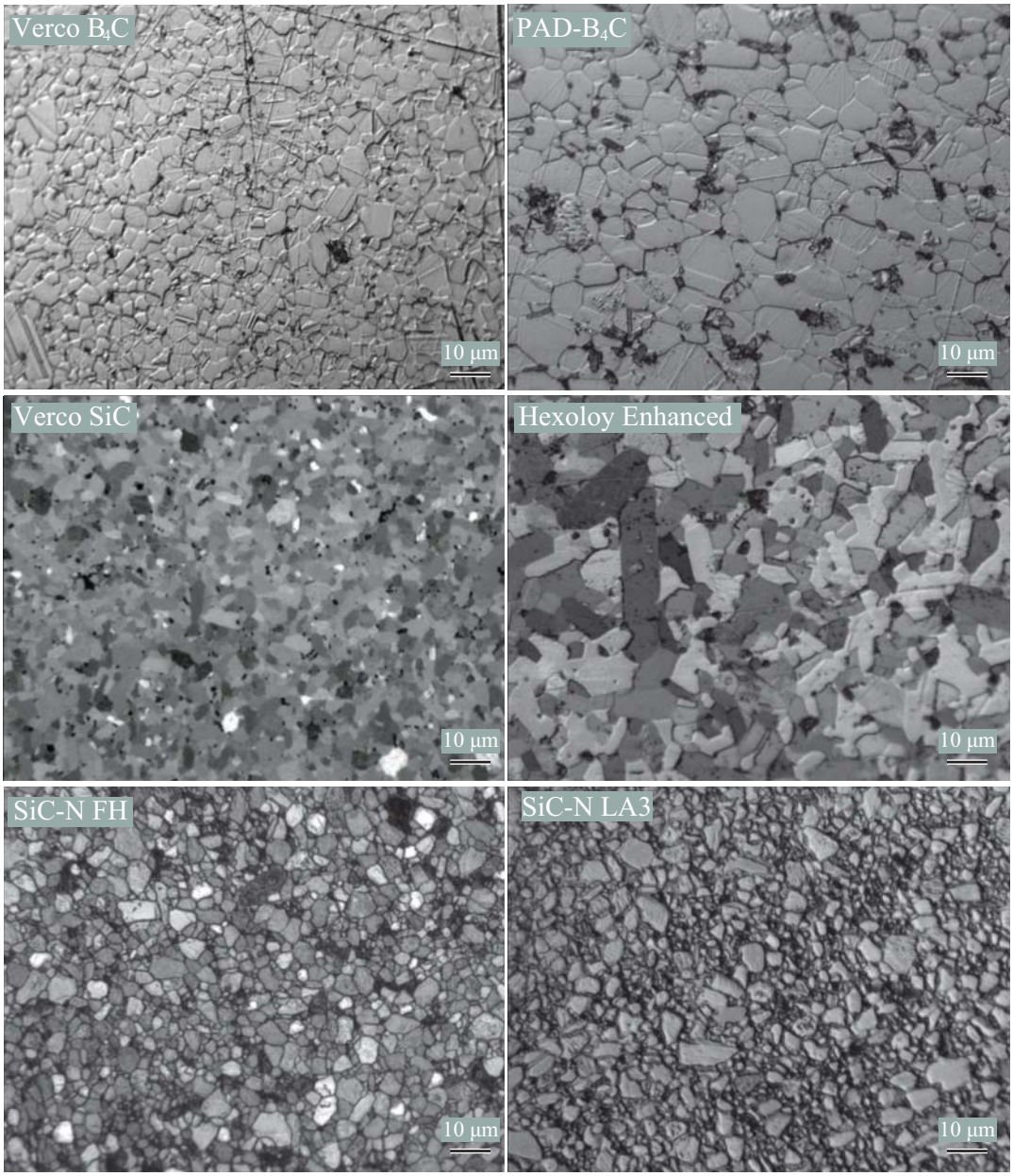

Figure 36: Optical micrographs of the B_4C and SiC samples. The scale bar on all images is 10 μm.

Table 15: Mechanical Characterization of Armor Ceramics

Specimen	Density g/cm^3	Flexural Strength MPa	Fracture Toughness MPa m$^{1/2}$	Vickers Hardness (HV1) kg/mm^2	Knoop Hardness (HK2) kg/mm^2	Elastic Modulus GPa
Verco B_4C	2.520	392.36 ± 58.36	2.73 ± 0.16	2946.30 ± 62.57	2215.20 ± 89.55	454.226
PAD-B_4C	2.505	397.96 ± 33.51	2.90 ± 0.39	2632.40 ± 111.68	2019.90 ± 60.24	445.514
Verco SiC	3.196	486.93 ± 103.97	2.48 ± 0.38	2628.30 ± 44.13	2098.50 ± 24.87	434.372
SiC-N FH	3.202	599.06 ± 25.26	4.51 ± 0.09	–	1956.40 ± 24.80	448.818
SiC-N LA3	3.201	578.30 ± 26.69	4.49 ± 0.24	–	1959.30 ± 30.43	443.597
Hexoloy Enh.	3.153	458.97 ± 43.40	2.73 ± 0.43	2308.10 ± 87.96	1975.90 ± 57.53	431.702

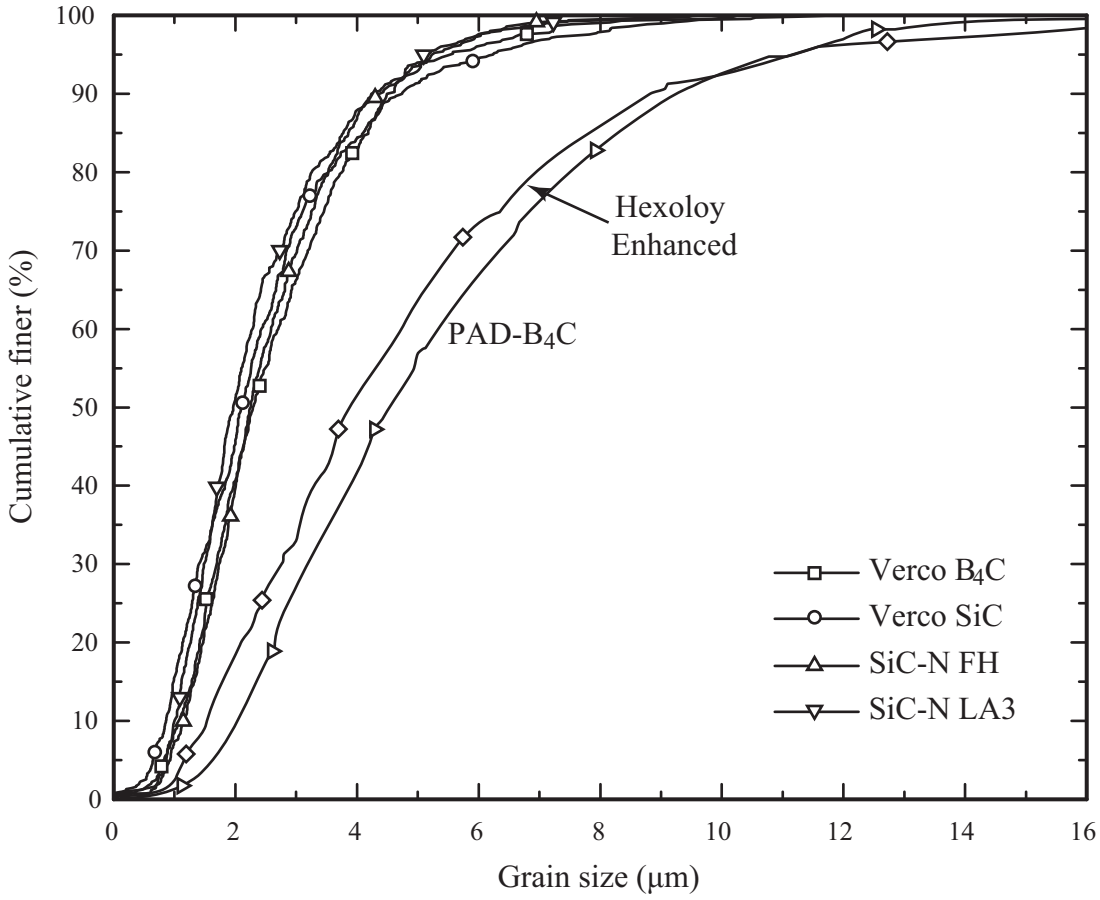

Figure 37: Grain size distributions for all samples. Verco B_4C, Verco SiC and SiC-N varieties share similar size distributions. Hexoloy Enhanced and PAD-B_4C have a coarser and broader distribution.

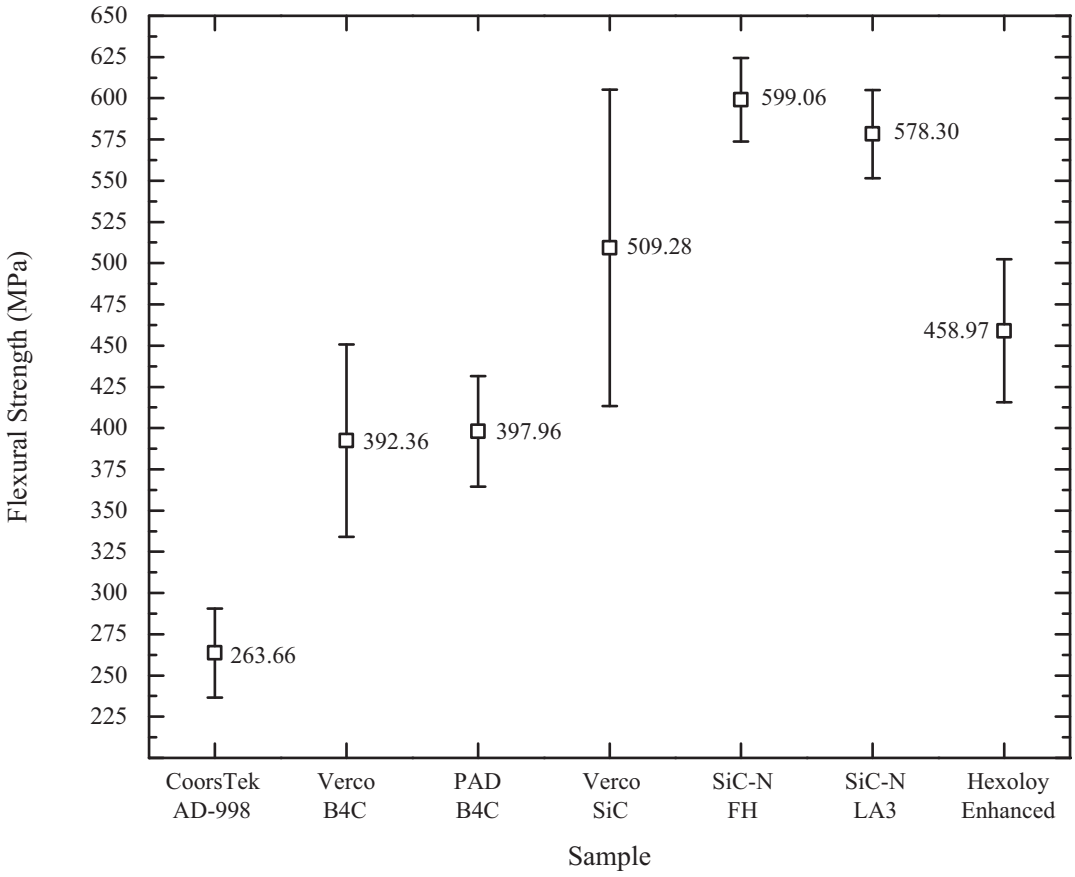

Figure 38: Flexural strength for all ceramic materials tested using the ASTM C1161-02c standard. SiC-N bars exhibit the highest flexural strength values for all compositions. The Verco SiC specimen showed a comparatively wide distribution in strengths.

hot-pressed and sintered SiC ceramics using Al_2O_3, Al_2O_3-Y_2O_3, and AlN-Y_2O_3 densification aids [43, 44, 56, 57]. Hexoloy Enhanced differs from the other SiC materials, however, this strength value closely matches the 428 MPa listed in the Saint-Gobain literature. The Verco SiC specimen showed a comparatively wide distribution in strengths, however still exhibited a higher bending strength overall than Hexoloy. Thevenot lists flexural bend strength values ranging from 480 MPa for hot-pressed B_4C (99.5% relative density) to 351 MPa for sintered B_4C (∼98% relative density) with 1 wt.% carbon [8]. It has been shown [58] that the mechanical properties of B_4C decrease precipitously with porosity, which therefore explains the high strength obtained from Verco B_4C (no porosity or added graphite).

The chevron-notch beam test results for the ceramic samples are shown in Figure 39. Previously reported values for B_4C fracture toughness using single-edge notched beam test (SENB) and indentation methods are in the 2.9–3.7 MPa $\sqrt{m}$ [8] range. Fracture toughness values have been shown to decrease as porosity decreases in B_4C samples [63]. Therefore, the lower value for fracture toughness of Verco B_4C was expected over PAD-B_4C. This trend was also true for Verco SiC and Hexoloy Enhanced. The measured values for FH and LA3 are similar to other reported values for SiC-N [62]. Hexoloy Enhanced fracture toughness was a radical departure from the listed number in Saint Gobain's literature (4.60 MPa $\sqrt{m}$), although the same methods of testing are claimed. However, fracture toughness values similar to those obtained in this work for solid-state sintered SiC have been reported in literature [15, 57, 60]. The disparity in the reported value could be attributed to a difference of testing parameters or testing type.

Vickers indentation in ceramic materials is difficult due to the excessive cracking that occurs in the material, which makes hardness measurement difficult due to the occlusion of diamond indentation edges. Vickers indentation results can also vary depending on the user and the equipment. However, they provide a good insight into the fracture mode of the ceramic body [15] and are less prone to effects of surface flatness and finish [52]. Vickers indentation values were collected for all measurable samples using a 9.8 N (1 kgf) load and are shown in Figure 40. Verco B_4C displayed the highest indentation hardness while PAD-B_4C has a significantly lower value and a much larger deviation in values. Verco SiC exhibits the highest Vickers hardness value seen in all SiC samples tested, with mean values approximately equal to those of PAD-B_4C. The low spread in the standard deviation values for Verco SiC are a clear indication of a homogeneous microstructure. Hexoloy Enhanced hardness values, while being significantly lower than Verco SiC, are within the reported range of other pressureless-sintered SiC ceramics referenced in literature [15, 60, 61, 62].

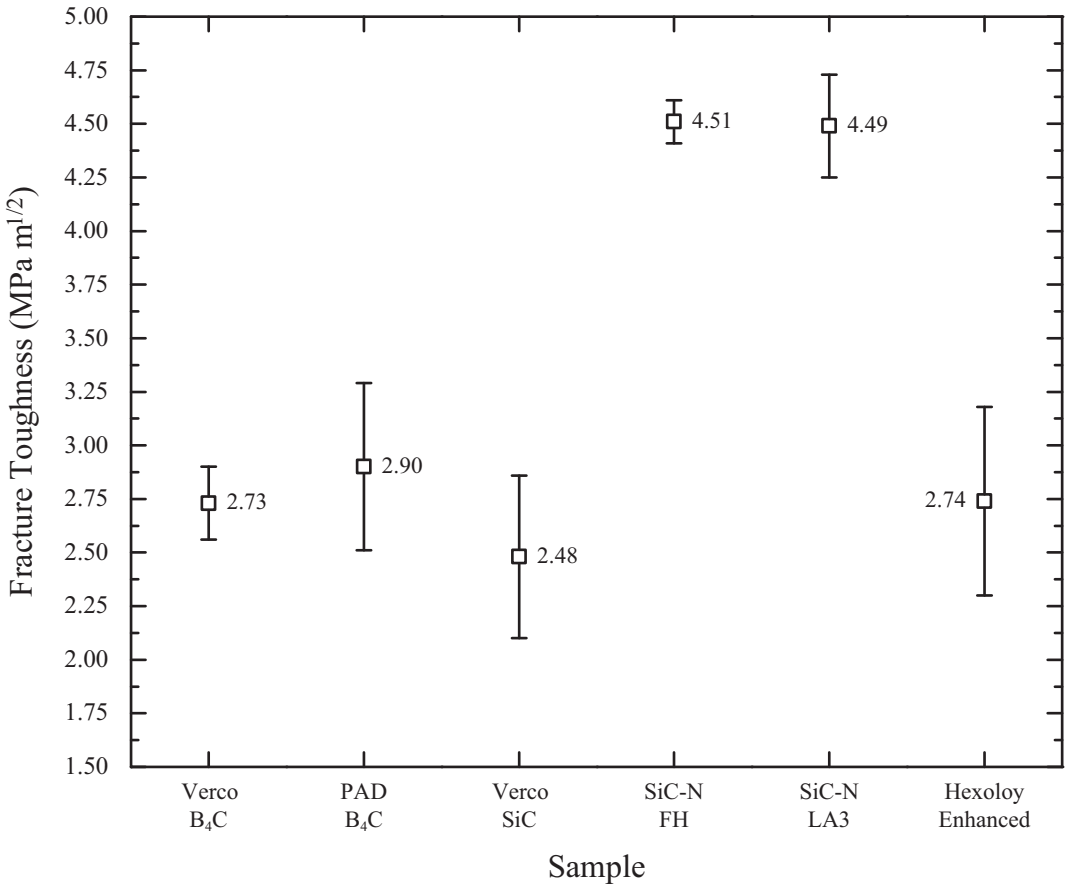

Figure 39: Chevron-notch fracture toughness values for all the ceramic samples using the ASTM C1421-01b standard. SiC-N samples exhibited higher fracture toughness values, due to the intergranular nature of the fracture mode.

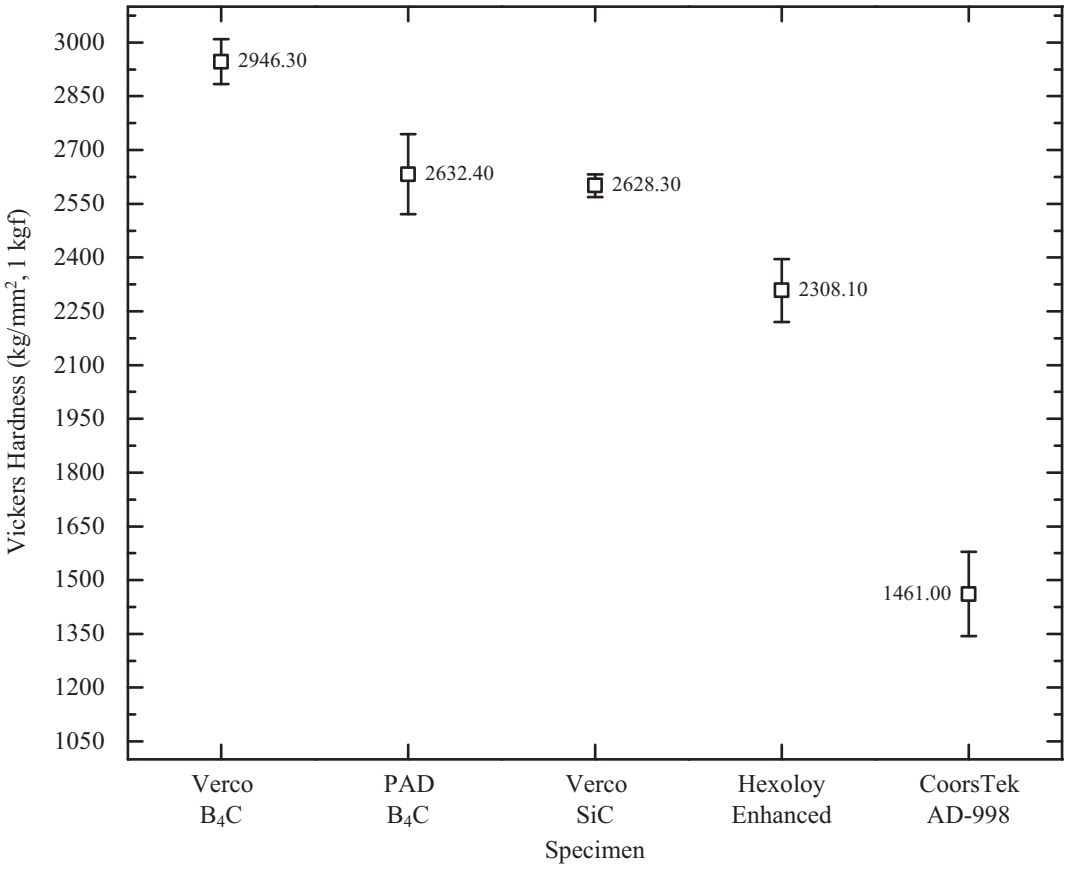

Figure 40: Vickers hardness indentation values for all samples according to the recommendations of the ASTM C1327–99 standard (1 kgf load). Verco B_4C and SiC are the hardest materials in both their respective materials. Verco SiC has a mean value approximately equal to that of PAD-B_4C.

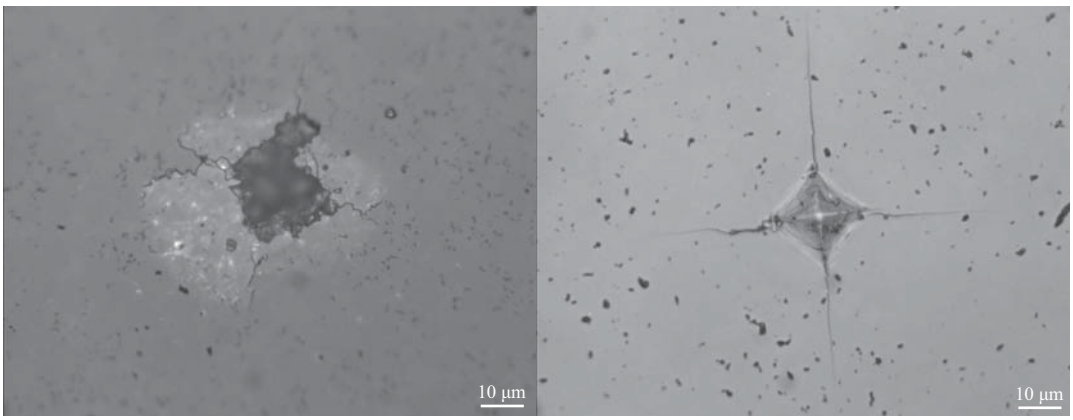

Figure 41: Optical micrography of Vickers indentations in a) SiC-N and b) Verco B_4C. Both SiC-N samples were unmeasurable at varying indentation loading levels as the intergranular nature of the cracking caused erratic indentation patterns.

The SiC-N sample indentations were not able to be measured due to erratic indentation patterns caused by the intergranular nature of the ceramic, as shown in Figure 41. Another source [62] has a reported value of 2233.09 ± 40.78 kg/mm^2 for SiC-N Vickers indentation using the standard method (HV1). However, varying indentation loads were applied with similar erratic results, therefore Vickers hardness testing of these materials was discontinued for this work.

Knoop hardness indentation testing is often preferred over the Vickers method since cracking becomes much less of an issue due to the more readily visible indentation in the sample [64]. Various studies have shown that a 19.6 N (2 kgf) Knoop test is the best means of determining hardness of an armor ceramic [53, 55]. It has been shown that the indentation size effect (ISE), the phenomenon in where the hardness of a ceramic decreases with increasing load, tends to disappear with loadings over 1 kgf [55]. Only one diagonal needs to be measured (the Knoop diagonal is 2.8 times longer than a Vickers diagonal of the same load [53]), which leads to less visual interpretation and a tighter standard deviation of measurement. SiC-N samples still exhibited large amounts of erratic cracking, however Knoop indentation values were measurable for both samples, since the diagonal tips were far enough away from

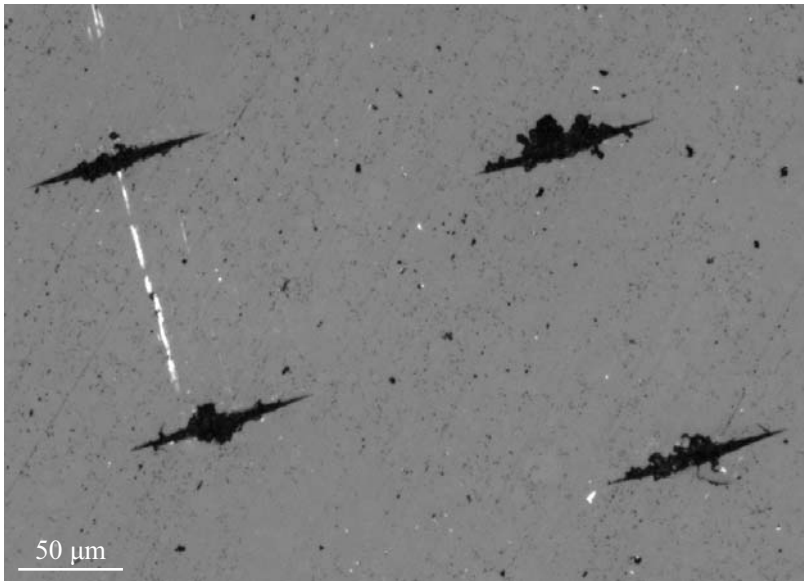

Figure 42: Knoop indentations taken in SiC-N FH exhibiting erratic central cracking but clear, defined diagonal edges.

the erratic indentation and were clearly visible, as shown in Figure 42. All Knoop indentation values using a 2 kgf load are shown in Figure 43.

While differing in value and scaling, the values for Knoop hardness have similar trend to the Vickers sample indentations. Of note are the SiC-N samples, which exhibit the lowest Knoop hardness values of all SiC samples. The data supports an inversely proportional relationship between hardness and fracture toughness (illustrated in Figure 44); the SiC-N samples exhibit superior fracture toughness values compared to the solid-state sintered SiC specimens. Similar experiments relating pressureless-sintered SiC versus hot-pressed or liquid phase sintering (LPS) SiC also concluded that LPS or hot-pressed SiC samples generally performed worse in hardness testing than solid-state SiC [15, 60]. What is clearly seen in the Knoop test, however, is the superior values of Knoop hardness for the Verco SiC sample over that of Cercom B_4C. Since the ISE of these materials should be saturated at a 2 kgf load, these values insinuate that Verco SiC should perform better than Cercom B_4C at a higher Vickers indentation loading.

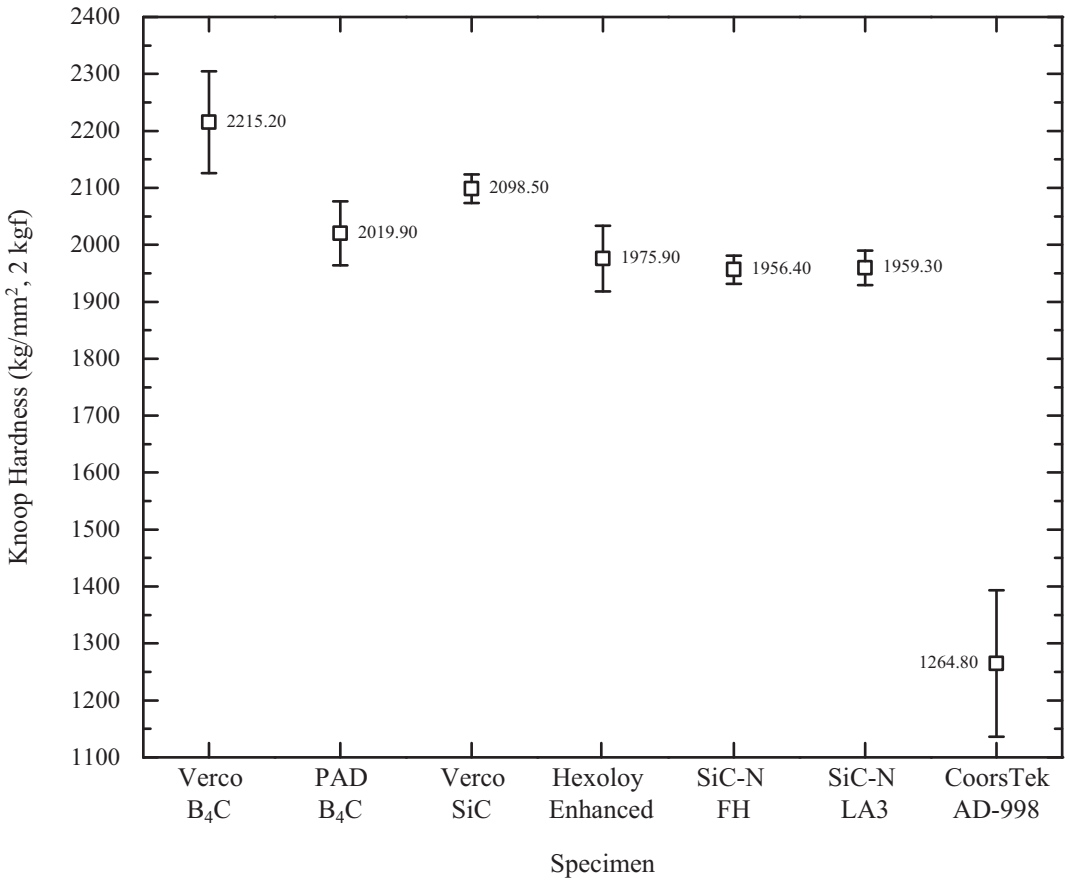

Figure 43: Knoop hardness indentation values for all samples taken in accordance with the ASTM C1326–03 standard (2 kgf). The general trend is similar as those shown in the Vickers hardness results, however, Verco SiC indentation values overtake those of PAD-B_4C.

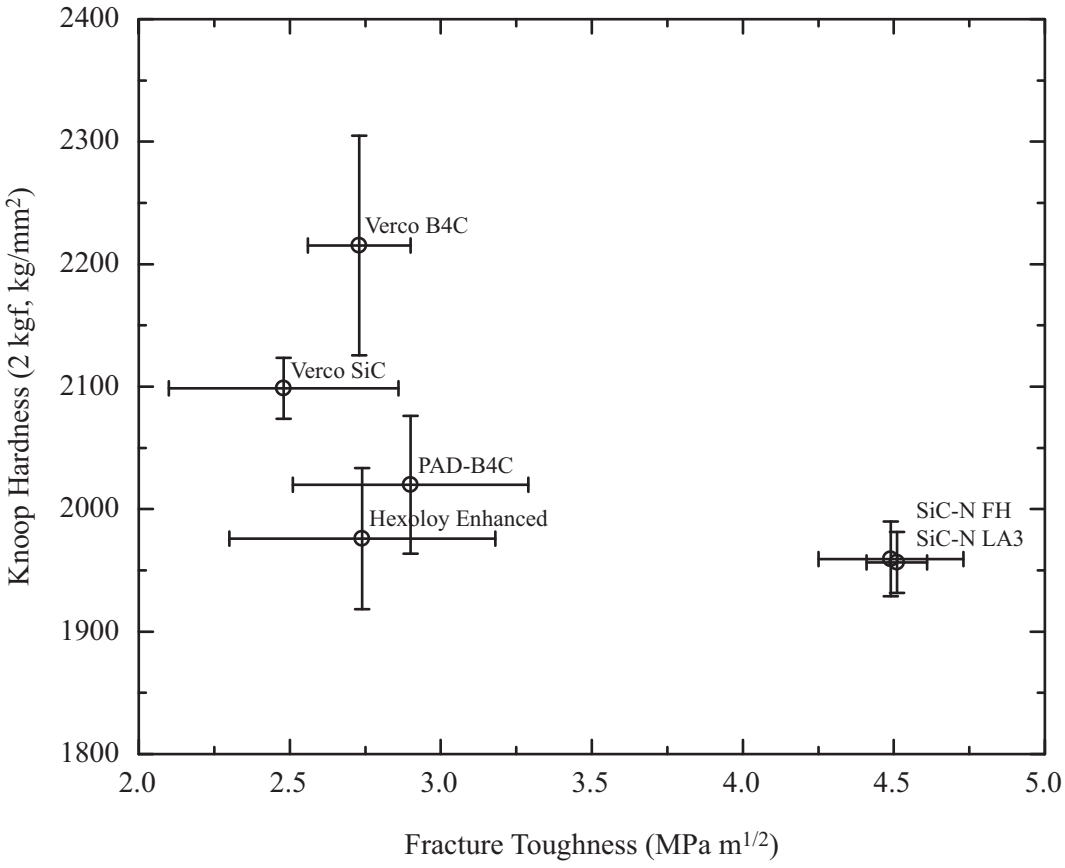

Figure 44: Knoop hardness (2 kgf) as a function of chevron-notched beam fracture toughness. The trend suggests an inverse relationship between the two mechanical properties.

Vickers and Knoop indentations were performed on each ceramic at 4.9 N (0.5 kgf), 9.8 N (1 kgf), and 19.6 N (2 kgf) loadings. 2 kgf is the highest loading the hardness test apparatus could achieve. 10 acceptable indentations were recorded for each loading. The results of the different loadings for both Vickers and Knoop are shown in Figures 45 and 46, respectively. The overlaid results showing the trend for both indenter types is shown in Figure 47. As shown in these figures, all samples exhibit a downward trend from lowest indentation load to highest, which was expected. Most of the sample hardness values seem to saturate at around 2 kgf. However, since testing was limited to a maximum of 2 kgf, it was impossible to confirm that the ISE had been eclipsed (as in Swab's work [55]). A similar pattern between Verco SiC and PAD-B_4C did occur in Vickers and Knoop loadings. Verco SiC matched and then eclipsed the hardness value for PAD-B_4C after 9.8 N (1 kgf).

The elastic modulus obtained for Verco B_4C is near the theoretical threshold value as reported by Thevenot [8], an indication of the high purity and homogeneity of the microstructure. Elastic moduli for SiC-N are comparable to reported values (as measured using strain gages) [62]. Verco SiC and Hexoloy Enhanced exhibit a lower value, which is likely a result of the slightly higher level of porosity in this sample compared to the SiC-N samples.

4.4 Ballistic Evaluation of SiC Armor

The System VII furnace interior was swapped out for a new graphite insulation package and elements to ensure the furnace interior was free of B_4C phase (It has been seen in previous tests that B_4C and SiC can form a eutectic liquid). Test pieces of SiC were run in the furnace at high temperatures until the density of subsequent tiles reached a plateau. An "aging" phenomenon has to occur, in where silicon phase has to reach an appreciable amount of infiltration into the insulation package before

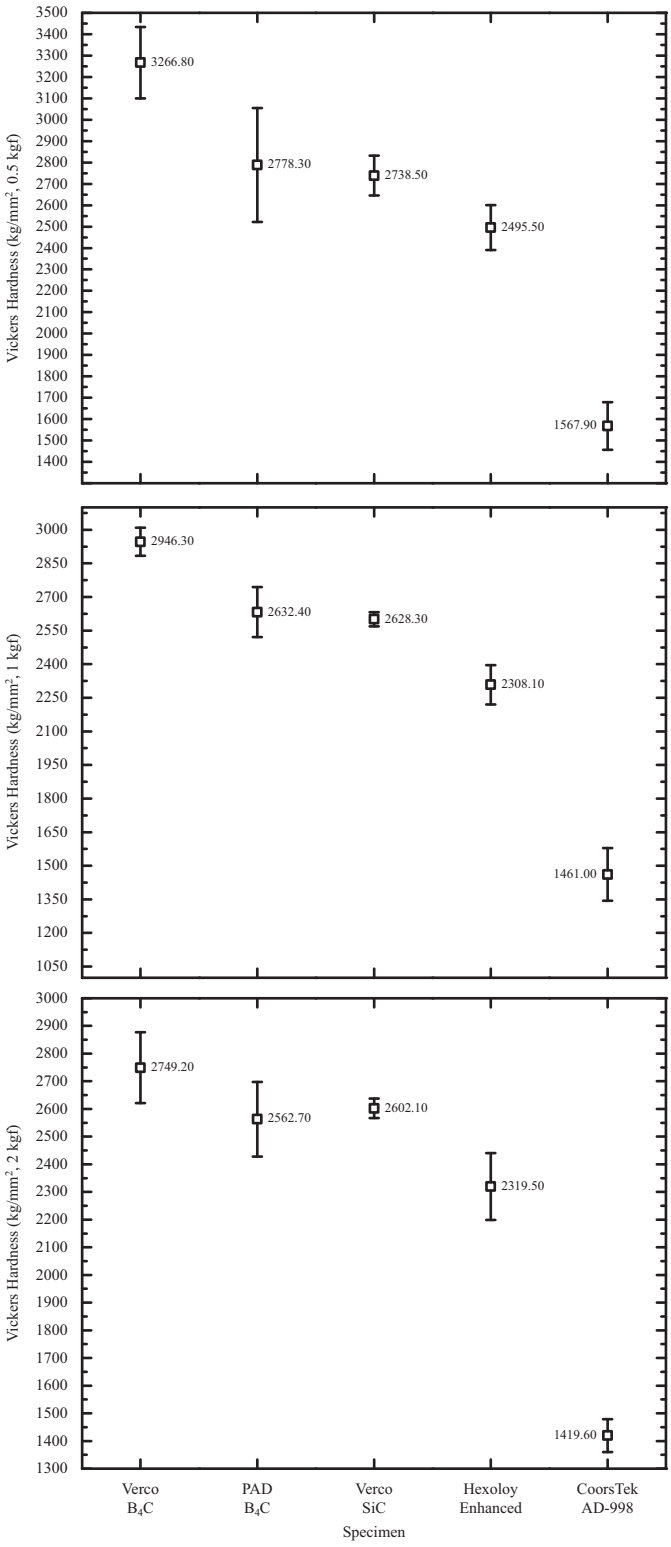

Figure 45: Vickers indentation results for all ceramic armor samples at 0.5, 1, and 2 kgf loadings.

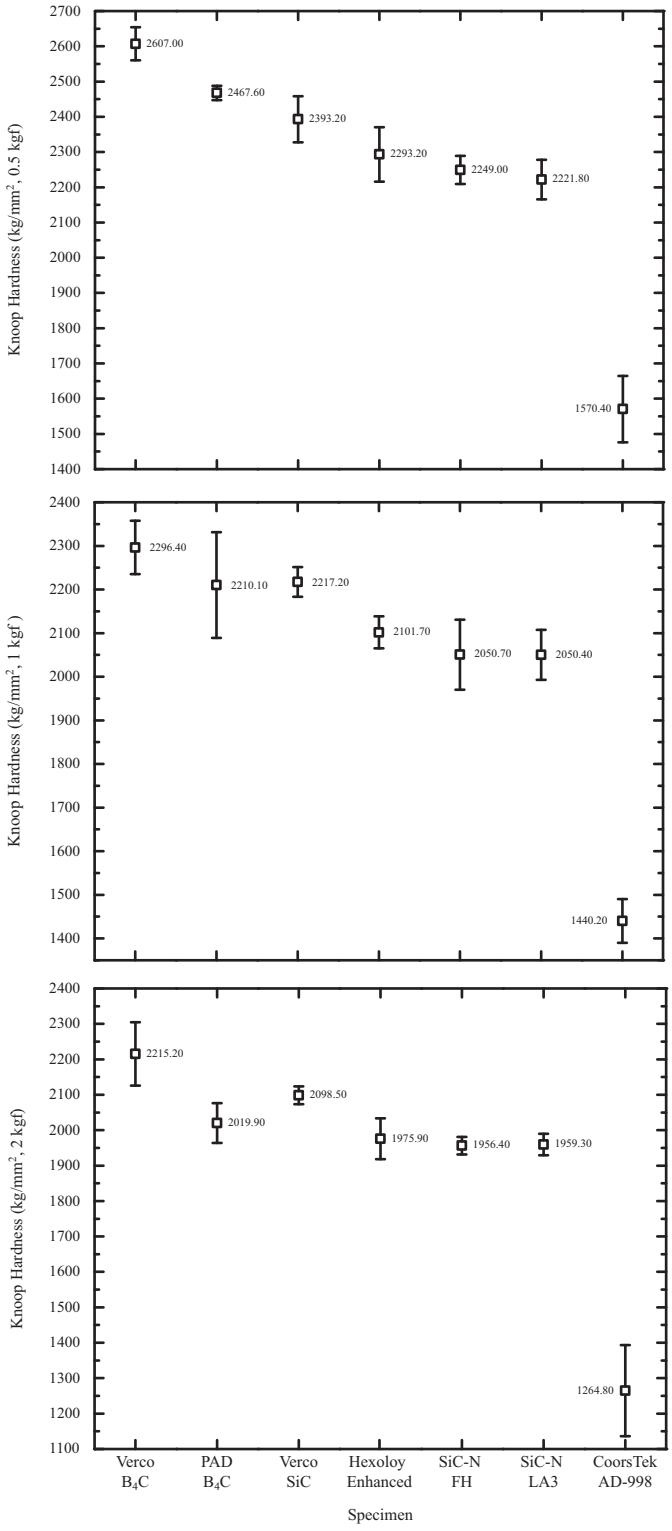

Figure 46: Knoop indentation results for all ceramic armor samples at 0.5, 1, and 2 kgf loadings.

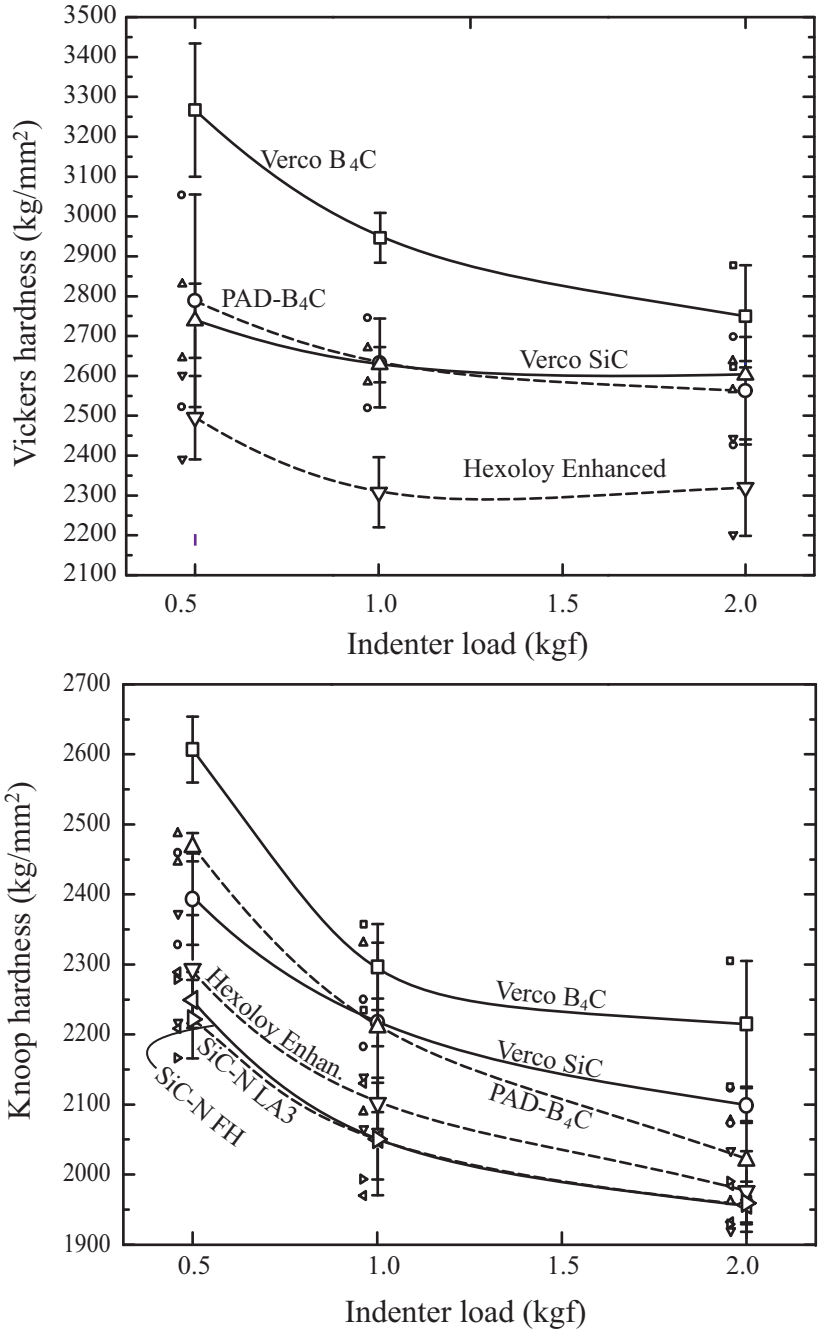

Figure 47: Vickers and Knoop indentations ranging from 0.5–2 kgf for each ceramic. A general downward trend is evident for all samples in accordance with the indentation size effect. Verco SiC exhibits a higher hardness compared to PAD-B_4C at increasing indentation load for both Vickers and Knoop.

sintered parts are consistently uniform. Due to differences between furnaces and optical temperature measuring equipment, the temperature for optimal sintering of the tiles needed to be discovered for the System VII. Tiles were sintered initially at a high temperature, which was consequently lowered with each sintering run until the density of the tiles reached around 95–96% relative density (based on geometric measurements). In the dilatometer, this optimal temperature was 2050°C. When firing large tiles in the System VII, however, the same results were obtained while firing between 2065–2100°C (depending on the part size, the thicker tiles needed a higher soaking temperature). All the remainging tiles were then subsequently sintered in this temperature range.

In the large sintering furnace, all the parameters of each run (temperature, pressure, power) are collected and logged for further evaluation. For the SiC runs, the parts were run under a pumping atmosphere for the first 800°C, in the range where water and any remaining organic species could vaporize off the parts. At higher temperatures, the furnace is set to a range mode, in where the pump is set to initialize whenever the pressure reaches a maximum of 10 Torr and to shut off when the pressure reaches a minimum of 1 Torr. The chamber pressure reading from a typical SiC run is shown in Figure 48. The amount of gas evolved from the parts past 1300°C is variable depending on the amount of tile loading in the furnace. However, in the range of 995–1160°C, there is always a large surge in outgassing from the parts, shown in Figure 49. This range for outgassing is highly repeatable for every run in the furnace. It is hypothesized to be the outgassing of CO or SiO due to the carbon-silica reaction, however, an analysis of the residual gases could not be performed at this time.

The 15 tiles selected from each size group had densities ranging from 3.1709–3.196 g/cm^3. These values, taken relative to the rule of mixtures theoretical density of 3.1757 g/cm^3, fall between 99.85–100.6%. The variation evident that causes measured values above 100% theoretical density could be due to a size effect (as also seen in

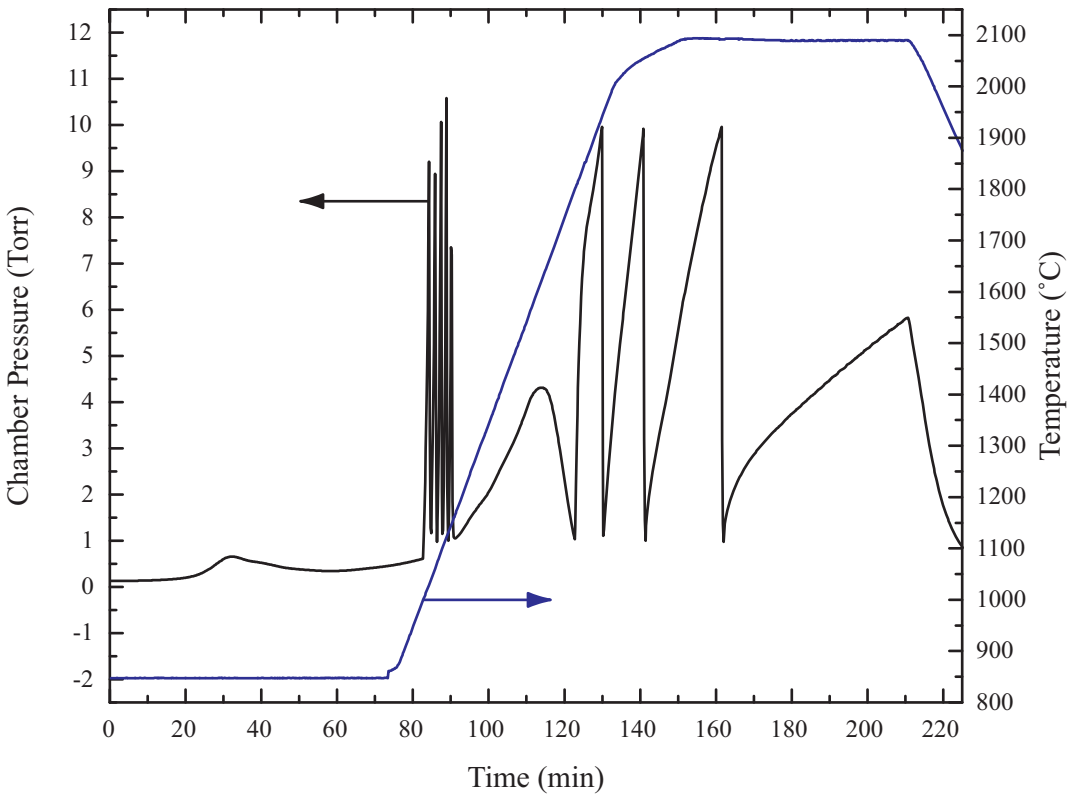

Figure 48: Typical sintering run for SiC in the Centorr System VII furnace.

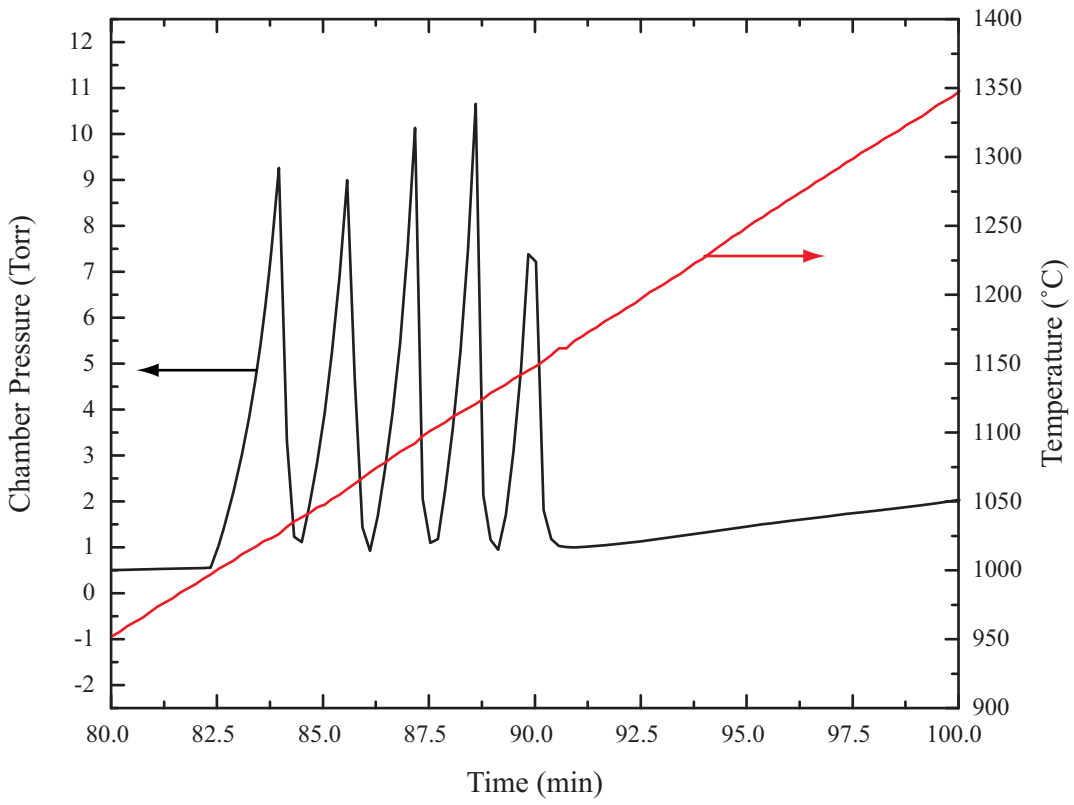

Figure 49: Zoomed in view of the area of severe outgassing between 995–1160°C.

Table 16: Merit Factor for SiC Armor Samples

Sample	Merit Factor
Historical Supplier 1	1.000
Historical Supplier 2	0.990
Supplier 3	0.942
Supplier 4	1.014
Verco SiC	1.031

previous work [2]), or more likely attributed to a small variation in carbon additive percentage from part to part.

Penetration velocities were established for each SiC sample tested by Foster-Miller. A "merit factor" was established for the performance of each supplier, which is a ratio of the V_{50} result for a given supplier's SiC tiles, as bonded to a composite backing, linearly pro-rated in proportion to variations in areal densities for each sample. The merit factor scores are listed in Table 16 and illustrated graphically in Figure 50. When the areal density of each supplier's tiles are taken into account, Verco SiC has the highest merit factor.

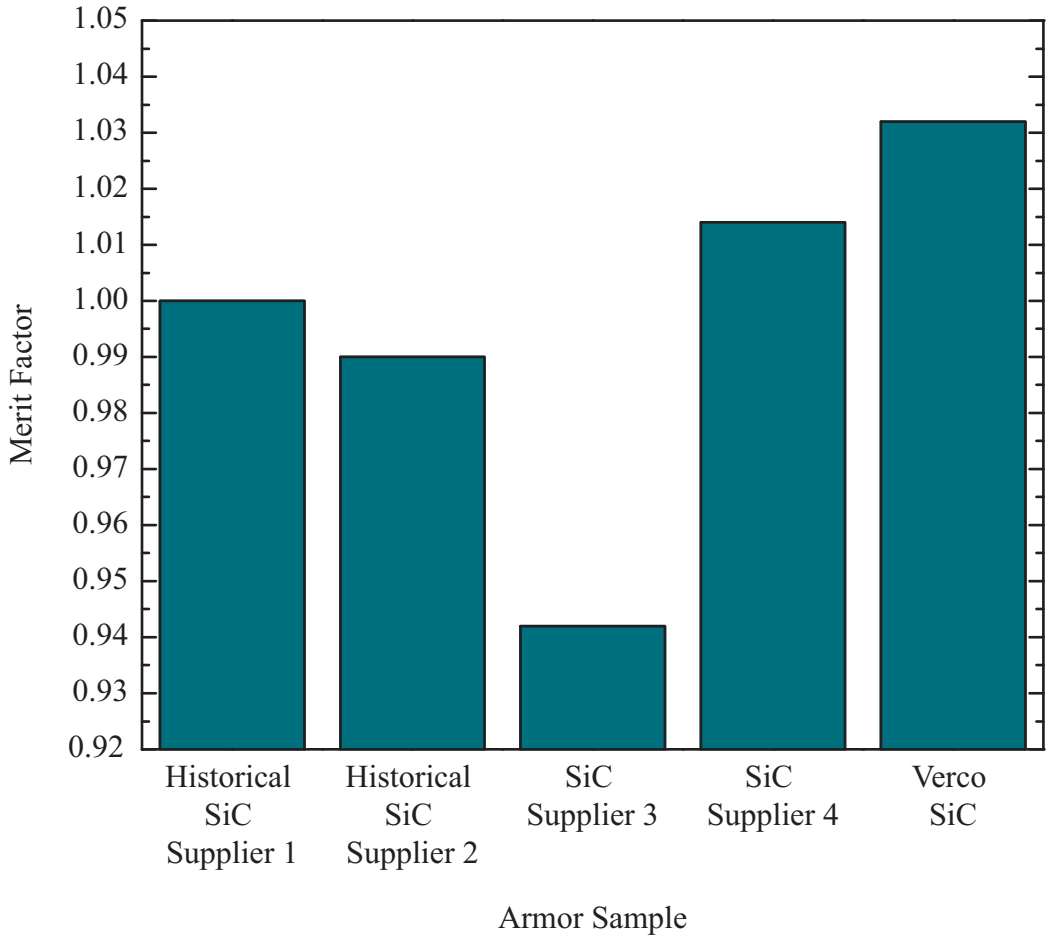

Figure 50: Merit factors calculated through ballistic testing of SiC tiles using a 7.62 × 54R mild steel ball round. Verco SiC exhibits the highest ballistic behavior.

CHAPTER V

DISCUSSION

Optimizing the microstructure of solid-state sintered SiC through optimizing the additive amount and through utilizing sintering and post-HIPing methods enabled the manufacturing of a SiC part that was theoretically-dense and exhibited a fine, equiaxed-grained microstructure. The density of 4" × 4" sent for ballistic testing were theoretically dense compared to the rule of mixture density calculated for a 2.5 wt.% carbon addition, however, neglecting the carbon content and calculating the density of all SiC samples (using the pure hexagonal SiC of 3.211 g/cm^3), the relative densities of Verco SiC, Hexoloy Enhanced, and SiC-N, were 99.3%, 98.0%, and 99.5%, respectively. Carbon derived from phenolic resin was more uniformly and finely dispersed throughout the Verco SiC part than in the Hexoloy Enhanced part (Figure 34), leading to better homogeneity throughout the microstructure. Sintering to a cutoff density of ∼96% relative density followed by post-HIPing eliminates the tendency for abnormal grain growth, resulting in a much finer microstructure (Figure 36) than that of Hexoloy Enhanced. Pore entrapment in grains is also reduced, leading to higher density in Verco SiC.

Exaggerated grain growth evident in the Verco SiC parts at high sintering temperatures, and the quick densification rate in the dilatometry traces suggest that there might be a liquid-phase sintering type mechanism involved in sintering SiC with boron. Grains also tend to show growth toward convex boundaries, which is not typical for solid-state sintering mechanisms (Figure 51). We have seen that B_4C and SiC combine to form a eutectic liquid at these sintering temperatures (from having run SiC parts in a furnace insulation inundated with boron vapor); however, the

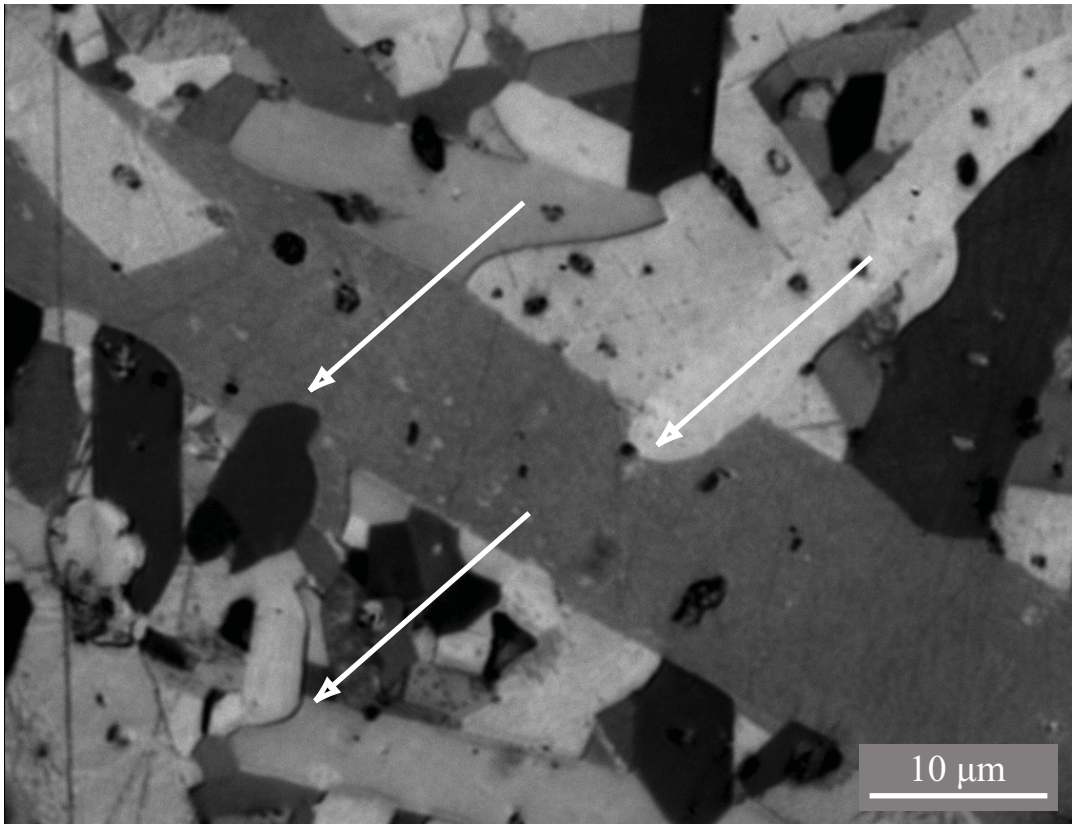

Figure 51: Microstructure of Verco SiC taken at 100×. Curved grain boundaries are evident, suggesting that there might be a liquid-phase sintering mechanism present.

amount of B_4C added (0.36 wt.%) in the Verco SiC parts is not substantial enough to form a fully-wetting liquid. EDS scans revealed no presence of a grain boundary phase, however the small grain boundary size (1–2 nm) and the difficuly in measuring boron using EDS can be contributing factors. Previous TEM work [61] of sintered SiC has shown no evidence of any secondary phases or elements in the grain boundaries and triple points (the boron content was similar (0.5 wt.%)). Therefore, the lack of evidence in quantitative analysis and the vastly superior hardness values combined with the transgranular fracture behavior of Verco SiC imply that the microstructure of Verco SiC does not exhibit any secondary intergranular phase.

The fracture toughness of the SiC-N materials was approximately three times those of all (SiC and B_4C) solid-state sintered ceramics. As reported in other work [15], the comparatively weak aluminosilicate interphase is the preferential path for crack

propagation, creating a tortuous path for cracks and facilitating crack deflection and bridging. The (4-point bending) fracture strength of a brittle ceramic is highly dependent on the size of the largest flaw on the surface under tension. The high strength and narrow strength distribution of SiC-N is an indicator of the decreasing importance of critical flaw size on strength, due to the crack branching and blunting mechanisms viable in these specimens. The Verco SiC specimen showed a broad distribution in flexural strengths. This implies that the strength of this material would be sensitive to surface finish.

Hardness results are not sensitive to surface flaws since these flaws are diminished through the polishing process. Hardness is a very localized test, and the specimen surface is under compression-induced shear rather than tension. Hardness generally shows a Hall-Petch relationship with grain size; the increase in hardness with decreasing grain size for boron carbide has been demonstrated in our previous work [63], therefore the materials with a finer grain size distribution would be expected to perform better. The Verco B_4C specimen was by far the hardest, as was expected. The presence of alumina embedded in graphite, a small amount of porosity, and the larger grain sizes of the PAD-B_4C are likely contributors to the comparatively lower hardness. It was expected that the hardness of B_4C materials would be superior to SiC materials. However, Verco SiC was remarkably high; as high as, and in some tests surpassing, PAD-B_4C. In comparing Verco SiC and Hexoloy Enhanced, the lower residual porosity and finer, equiaxed grains of the Verco material are consistent with higher measured hardnesses. The distribution in hardness of the Verco SiC is also very narrow. In comparing with the microstructure of Hexoloy Enhanced, because of the even distribution of graphite particles of finer dimension in Verco SiC, a hardness indenter would be more likely to measure the same behavior from one location to the next. The low hardness (and in the case of Vickers testing the immeasurability of the sample hardness) of the SiC-N specimens is attributable to the weak aluminosilicate

interphase at the SiC grain boundaries. Cracks meander and branch in all directions along the interphase under the load of the indenter and grains are broken out and pulled away with the diamond edge.

Reported hardness values for SiC materials vary considerably in the literature; more useful comparisons stem from measurements on the same instrument and by the same operator. Measured hardness decreasing with increasing indenter load is a result of a greater fraction of the energy imparted to the specimen going to crack formation and propagation, rather than plastic deformation. Lower loads give a truer picture of the specimen's resistance to localized plastic flow. Under these conditions; however, accurate measurement of indent dimensions becomes more difficult, due to the small size of the indentation and the difficulty of measurement.

Flinders [15] proposed that SiC-N materials performed better ballistically than their sintered SiC because of the high fracture toughness and high density of the parts compared to sintered SiC. Ray [60] did suggest, however, that a solid-state sintered SiC microstructure could perform as well as hot-pressed SiC (with high levels of fracture toughness) if the sintered parts could be processed to a finer grain size and higher density. Therefore, it was expected that the Verco SiC parts, exhibiting nearly the same density and grain size as SiC-N while having a much higher hardness, would perform well in ballistic testing. In the Foster-Miller testing group, Verco SiC outperformed four other manufactured SiC armor materials. However, it has been claimed that hot-pressed materials would perform better against a heavier penetrator, such as a tungsten carbide-cored armor piercing round. Future tests will be conducted to explore this hypothesis.

CHAPTER VI

CONCLUSION

The focus of this work was to create a theoretically-dense, clean-grain boundary, fine and equiaxed solid-state sintered silicon carbide microstructure that would exhibit superior hardness values and ballistic properties. The carbon content, sintering temperature, heating rates, and post-HIPing parameters were studied. Carbon additive amounts between 2.0–2.5 wt.% (depending on the resin source) yielded parts with high sintering densities, while keeping excess carbon in the final microstructure to a bare minimum. A slow heating rate to a 2050°C sintering soak yielded a dense sintered part with minimal open porosity and lack of pronounced grain growth (d_{50} = 2.525 μm). Post-HIPing at 1900°C removed the remaining closed porosity, and a theoretically-dense part was produced (3.175 g/cm^3), exhibiting none of the anisotropy and abnormal grain growth inherent to similar solid-state sintered SiC ceramics, such as Hexoloy Enhanced (d_{50} = 4.837 μm). Due to the optimized microstructure, Verco SiC parts exhibited the highest Vickers and Knoop hardness values of any SiC ceramic, and values equal to those of a commercial hot-pressed boron carbide (PAD-B_4C). While the fracture toughness of hot-pressed SiC materials are almost double that of Verco SiC, ballistic results imply that the high hardness and clean, homogenous microstructure of Verco SiC leads to a better performing ballistic product.

REFERENCES

[1] S. R. Skaggs, "A Brief History of Ceramic Armor Development," *Ceramic Engineering and Science Proceedings,* **24** [3] *Ceramic Engineering And Science Proceedings: 27th International Cocoa Beach Conference on Advanced Ceramics and Composites:A* 337–349 (2003).

[2] R. F. Speyer, N. Cho, and Z. Bao, "Density- and Hardness Optimized Pressureless Sintered and Post-HIPped B_4C," *J. Mat. Res.,* **20** [8] 2110–16 (2005).

[3] V. Skorokhod Jr., M. D. Vlajic, and V. D. Krstic, "Mechanical Properties of Pressureless Sintered Boron Carbide Containing TiB_2 Phase" *J. Mat. Sci. Lett.*, **15** [15] 1337–39 (1996).

[4] C. H. Lee, C. H. Kim, "Pressureless Sintering and Related Reaction Phenomena of Al_2O_3-doped B_4C," *J. Mater. Sci.*, **27** [23] 6335–340 (1992).

[5] K. Kawase, and K. Nakano, "Additive Effect on Sintering of Boron Carbide," *J. Ceram. Soc. Jpn.,* **95** [11] 1137–40 (1987).

[6] K. Zakhariev and D. Radev, "Properties of Polycrystalline Boron Carbide Sintered in the Presence of W_2B_5 without Pressing," *J. Mater. Sci. Lett,* **7** [7] 695–696 (1988).

[7] K. Schwetz and G. Vogt, "Process for the Production of Dense Sintered Articles of Boron Carbide," *U.S. Patent 4,195,066,* (1980).

[8] F. Theveonot, "Boron Carbide - A Comprehensive Review," *J. Euro. Ceram. Soc.,* **6** [4] 205–25 (1990).

[9] K. Niihara, A. Nakahira, and T. Hirai, "The Effect of Stoichiometry on Mechanical Properties of Boron Carbide," *J. Am. Ceram. Soc.,* **67** C13–C14 (1984).

[10] H. Lee and R. F. Speyer, "Pressureless Sintering of Boron Carbide," *J. Am. Ceram. Soc.,* **86** [9] 1468–73 (2003).

[11] H. Lee, W. S. Hackenberger, and R. F. Speyer, "Sintering of Boron Carbide Heat-treated with Hydrogen," *J. Am. Ceram. Soc.,* **85** [8] 2131–33 (2002).

[12] M. Chen, J. W. McCauley, K. J. Hemker, "Shock-Induced Localized Amorphization in Boron Carbide," *Science,* **299** 5612 1563–1566 (2003).

[13] G. Fanchini, J. W. McCauley, M. Chhowalla, "Behavior of Disorder Boron Carbide Under Stress," *Physical Review Letters,* **97** 035502 1–4 (2006).

[14] P. J. Hazell, C. J. Roberson, M. Moutinho, "The Design of Mosaic Armour: The Influence of Tile Size on Ballistic Performance," *Materials and Design,* **29** 1497–1503 (2008).

[15] M. Flinders, D. Ray, A. Anderson, R. A. Cutler, "High-Toughness Silicon Carbide as Armor," *J. Am. Ceram. Soc.,* **88** [8] 2217–2226 (2005).

[16] S. D. Nunn, J. G. R. Hansen, B. J. Frame, and R. A. Lowden, "Improved Ballistic Performance by Using a Polymer Matrix Composite Facing on Boron Carbide Armor Tiles," *Ceram. Eng. and Sci. Proc.,* **26** [7] *Advances in Ceramic Armor: A Collection of Papers Presented at the 29th International Conference on Advanced Ceramics and Composites* 287–292 (2005).

[17] H. O. Pierson, *Handbook of Refractory Carbides and Nitrides,* John Wiley & Sons, New York, 1996.

[18] R. S. Kern, "Solid Solutions of AlN and SiC Grown by Plasma-assisted Gas-Source Molecular Beam Epitaxy," *J. Mater. Res.,* **8** (7) 1477–80 (1993).

[19] G. R. Fisher and P. Barnes, "Toward a Unified View of Polytypism in Silicon Carbide," *Philosophical Magazine* B61:217–36 (1990).

[20] T. B. Shaffer, "Engineering Properties of Carbides," pp. 804–811 in *Engineering Materials Handbook, Volume 4, Ceramics and Glasses,* S. J. Schneider, Jr., Editor, ASM International, Materials Park, OH (1991).

[21] S.J. L. Kang, *Sintering,*, Elsevier Butterworth-Heinemann, Boston (2005).

[22] W. D. Kingery, H. K. Bowen, and D. R. Uhlmann, *Introduction to Ceramics*, 2nd Edition, John Wiley & Sons, New York (1976).

[23] R. M. German, *Sintering Theory and Practice*, John Wiley & Sons, New York (1996).

[24] J. E. Burke and J. H. Rosolowski, in *Treatise on Solid State Chemistry*, Vol. 4, N. B. Hannay, Ed., Plenum, New York, 1976, Chapter 10.

[25] W. J. Huppermann, S. Pejovnik, and S. M. Han, *Processing of Crystalline Ceramics,* Plenum, New York (1978).

[26] W. D. Kingery, "Sintering in the Presence of a Liquid Phase," in *Ceramic Fabrication Processes*, 2nd Edition, MIT Press and John Wiley & Sons, New York (1960).

[27] J. H. She and K. Ueno,"Densification Behavior and Mechanical Properties of Pressureless-Sintered Silicon Carbide Ceramics with Alumina and Yttria Additions," *Materials Chemistry and Physics,* **59** 139–42 (1999).

[28] J. W. Cahn and R. B. Heady, "Analysis of capillary forces in liquid-phase sintering of jagged particles," *J. Am. Ceram. Soc.,* **53** [7] 406–409 (1970).

[29] H. S. Cannon and F. V. Lenel, "Some Observations on the Mechanism of Liquid Phase Sintering," in *Plansee Proceedings*, 1952, F. Benesovsky (Ed.), Metalwerk Plansee, Reutte, p. 106 (1953).

[30] H.H. Park, O.J. Kwon and D. N. Yoon, "The critical grain size for liquid flow into pores during liquid phase sintering," *Metall. Trans. A,* **17 A**, 1915–19 (1986).

[31] J. K. Park, S.J. L. Kang, K. Y. Eun, and Y. D. Yoon, "The Microstructural change during liquid phase sintering," *Metall. Trans. A*, **20A**, 837–45 (1989).

[32] S.M. Lee and S.J. L. Kang, "Theoretical analysis of liquid phase sintering: pore filling theory," *Acta Mater.,* **46**, 3191–202, (1998).

[33] J.C. Baung, Y.G. Choi, E.S. Kang, Y.K. Baek, S.W. Jung,and S.J. Kang, "Effects of sintering atmosphere and Ni content on the liquid phase sintering of TiB_2-Ni," *J. Kor. Ceram. Soc.,* **38**, 207–11 (2001).

[34] S. Prochazka and R. M. Scanlan, "Effect of Boron and Carbon on Sintering of Silicon Carbide," *J. Am. Ceram. Soc.,* **58** [1–2] 72 (1975).

[35] L. Stobierski and A. Gubernat, "Sintering of Silicon Carbide: 1. Effect of Carbon," *Ceramics International,* **29** 287–292 (2003).

[36] M. S. Datta, A. K. Bandyopadhyay, B. Chaudhuri, "Sintering of nano crystalline α silicon carbide by doping with boron carbide," *Bull. Mater. Sci.,* **25** [3] 181–9 (2002).

[37] L. Stobierski and A. Gubernat, "Sintering of Silicon Carbide: 2. Effect of Boron," *Ceramics International,* **29** 355–361 (2003).

[38] F. F. Lange, "Hot Pressing Behavior of Silicon Carbide with Additions of Aluminum Oxide," *J. Mat. Sci.,* **10** [2] 314–20 (1975).

[39] C. G. Bergeron and S. H. Risbud, *Phase Equilibria in Ceramics,* American Ceramic Society, Westerville, OH (1984).

[40] M. A. Mulla and V. D. Krstic, "Pressureless Sintering of β-SiC with Al_2O_3 Additions," *J. Mat. Sci.,* **29** 934–8 (1994).

[41] T. A. Parthasarathy, T. Mah, L. E. Matson, "Processing, Structure, and Properties of Alumina-YAG Eutectic Composites," *J. Ceram. Proc. Res.,* **5** [4] 380–390 (2004).

[42] M. Omori and H. Takie, "Preparation of Pressureless-sintered SiC-Y_2O_3-Al_2O_3," *J. Mat. Sci.,* **23** [10] 3744–9 (1988).

[43] G. Rixecker, I. Wiedmann, A. Rosinus, and F. Aldinger, "High-Temperature Effects in the Fracture Mechanical Behavior of Silicon Carbide Liquid-phase Sintered with AlN-Y_2O_3 Additives," *J. European Ceram. Soc.,* **21** 1013–19 (2001)

[44] S. K. Lee, Y. C. Kim, C. H. Kim, "Microstructural Development and Mechanical Properties of Pressureless-Sintered SiC with Plate-like Grains using Al_2O_3-Y_2O_3 Additives," *J. Mater. Sci.,* **29** 5321–26 (1994).

[45] W. D. G. Bocker, R. Hamminger, J. Huber, A. Roosen, "Covalent High-performance Ceramics," *Advanced Materials,* **4** [3] 169–78 (1992).

[46] M. Nader and F. Aldinger, "Influence of the α/β-SiC phase transformation on microstructural development and mechanical properties of liquid phase sintered silicon carbide," *J. Mat. Sci.,* **34** 1197–1204 (1999).

[47] J. S. Reed, *Principles of Ceramic Processing,* John Wiley and Sons, New York, New York (1995).

[48] R. A. Cutler, "Liquid Phase Sintering of Silicon Carbide" U.§. Patent 4,829,027 (1989).

[49] A. Ezis, "Monolithic, Fully Dense Silicon Carbide Material, Method of Manufacturing, and End Uses," U.§. Patent 5,372,978 (1994).

[50] ASTM C1161–02c "Standard Test Method for Flexural Strength of Advanced Ceramics at Ambient Temperature," 2007 Annual Book of ASTM Standards

[51] ASTM C1421–01b "Standard Test Method for Determination of Fracture Toughness of Advanced Ceramics at Ambient Temperature," 2007 Annual Book of ASTM Standards

[52] ASTM C1327–99 "Standard Test Method for Vickers Indentation Hardness of Advanced Ceramics," 2007 Annual Book of ASTM Standards

[53] ASTM C1326–03 "Standard Test Method for Knoop Indentation Hardness of Advanced Ceramics," 2007 Annual Book of ASTM Standards

[54] ASTM C1198–01 "Standard Test Method for Dynamic Young's Modulus, Shear Modulus, and Poisson's Ratio for Advanced Ceramics by Sonic Resonance," 2007 Annual Book of ASTM Standards

[55] J. J. Swab, "Recommendations for Determining the Hardness of Armor Ceramics," *Int. J. Appl. Ceram. Technol.,* **1** [3] 219–25 (2004).

[56] S. Jihong, G. Jingkun, and J. Dongliang, "Hot Isostatic Pressing of α-Silicon Carbide Ceramics," *Ceramics International,* **19** 347–351 (1993).

[57] S. S. Shinozaki, J. Hangas, K. R. Carduner, and M. J. Rokosz, "Correlation between microstructure and mechanical properties in silicon carbide with alumina addition," *J. Mater. Res.,* 8 [7] 1635–43 (1993).

[58] B. Champagne and R. Angers, "Mechanical Properties of Hot-Pressed B-B_4C Materials," *J. Am. Ceram. Soc.,* **62** [3-4] 149–153 (1979).

[59] C. H. Lee, C. H. Kim, "Pressurless Sintering and Related Reaction Phenomena of Al_2O_3-doped B_4C," *J. Mater. Sci.,* **27** [23] 6335–340 (1992).

[60] D. A. Ray, S. Kaur, R. A. Cutler, "Effect of Additives on the Activation Energy for Sintering of Silicon Carbide," *J. Am. Ceram. Soc.,* **91** [4] 1135–40 (2008).

[61] E. Pabit, K. Sieben, D. P. Butt, H. Heinrich, D. Ray, S. Kaur, R. M. Flinders, R. A. Cutler, "Grain Boundary Chemistry of SiC-Based Armor," *Ceramic Engineering and Science Proceedings,* **27** [7] *Advances in Ceramic Armor II - A Collection of Papers Presented at the 30th International Conference on Advanced Ceramics and Composites* 69–84 (2006).

[62] D. Ray, R. M. Flinders, A. Anderson, R. A. Cutler, "Effect of Microstructure and Mechanical Properties on the Ballistic Performance of SiC-Based Ceramics," *Ceramic Engineering and Science Proceedings,* **27** [7] *Advances in Ceramic Armor II - A Collection of Papers Presented at the 30th International Conference on Advanced Ceramics and Composites* 85–96 (2006).

[63] H. Lee and R. F. Speyer, "Hardness and Fracture Toughness of Pressureless-Sintered Boron Carbide (B_4C)," *J. Am. Ceram. Soc.,* **85** [5] 1291–93 (2002).

[64] C. Ullner, A. Germak, H. L. Doussal, R. Morrell, T. Reich, W. Vandermuelen, "Hardness Testing on Advanced Technical Ceramics," *J. Eur. Ceram. Soc.,* **21** 439–51 (2001).